Spray-assisted alignment of layer-by-layer assembled silver nanowires for linear and chiral nanoplasmonics

Hebing Hu

ÉCOLE DOCTORALE de Physique et de Chimie-Physique

Institut Charles Sadron (UPR22-CNRS)

THÈSE présentée par:

Hebing Hu

Soutenue le: **5 Novembre 2015**

Pour obtenir le grade de: **Docteur de I'Université de Strasbourg**

Discipline: **Chimie-Physique**

Spray-assisted alignment of Layer-by-Layer assembled silver nanowires for linear and chiral nanoplasmonics

Directeur de Thèse:

DECHER Gero	Professeur, Université de Strasbourg, France

Rapporteurs:

FERY Andreas	Professeur, Universität Bayreuth, Allemagne
STELLACCI Francesco	Professeur, EPFL, Suisse

Examinateurs:

JEAN Bruno	Professeur, CERMAV-CNRS, Grenoble, France
HAACKE Stefan	Professeur, Université de Strasbourg, France

Acknowledgements

This work of this dissertation was carried out at the Institut Charles Sadron (ICS) in Strasbourg, France. Some experiments were done in collaboration with 4th Physics Institute at the University of Stuttgart, Germany.

First, I would like to express my sincere gratitude to Professor Gero Decher, my PhD supervisor, for his support and guidance during my doctoral studies and research as well as his help in science and life.

I would like to express my gratitude to Professor Andreas Fery, Professor Francesco Stellacci, Professor Bruno Jean and Professor Stefan Haccke for accepting as referees for my thesis work and for the interesting discussions and comments during the defence.

I would like to thank Professor Harald Giessen for his suggestions and I am grateful to Thomas Weiss, Martin Schaeferling for their simulation work. I am grateful to Xinghui Yin, Julian Karst for their discussions and suggestions for my work. I am grateful to Laura Na Liu for letting me measure the CD and ORD with the Jasco spectrometer in her lab. I would like to thanks Christophe Contal for the AFM measurements, Cedric Leuvrey for the SEM images, Marc Schmutz for the TEM measurements, Thomas Hermans, Vincent Marichez and Martine Heinrich for the CD measurements, Fabinine Huber for the UV measurements and Oriol Arteaga for the Mueller Matrix Polarimetry measurements.

I would like to thank everyone that helped me with the administrative task during the PhD. Odile Lemble, Lea Koch, Katia Bruzzone, Leyla Ermis.

I would aslo like to thank Matthias Pauly for his guidence and help during my PhD, I

learned a lot from him. I would like to thank Olivier Felix for his suggestions and help for my work. Many thanks to all my collegues and friendliness. Seydina, Marek, Teru, Maria, Paul, Xiaofeng, Christophe, Vincent, Rebbeca, David, Michel, Jonas, Florian, Yulia, Souvik, Sri, Heveline, Marvin, Pauline.

Thanks to all my Chinese friends, we usually have lunch together and share our interesting things with each other. We will never forget the fantanstic experience in Strasbourg.

Huge thanks to my wife, Ying, for her continurous support and help in my life. She makes me forget the work when I back home. Usually the dinner is ready when I arrived at home. I am grateful to her for giving and taking care of my son, Yifan.

Double thanks to the people I forgot, you definitely belong here.

I dedicate this work to my family.

List of abbreviations

AFM	Atomic Force Microscopy
TEM	Transmission Electron Microscopy
SEM	Scanning Electron Microscopy
AgNW	Silver nanowire
LB	Langmuir-Blodgett
LbL	Layer-by-Layer
GIS	Grazing-incidence spraying
Milli-Q	Ultrapure Millipore water
PEI	Poly(ethyleneImine)
PAH	Poly(Allylamine Hydrochloride)
PSS	Poly(StyreneSulfonate)
SWNT	Single-Wall Carbon Nanotubes
UV	Ultraviolet

Dépôt couche-par-couche de films minces de nanofils d'argent orientés par pulvérisation pour des applications en nanoplasmonique linéaire et chirale

Résumé de Thèse en Francais

(Summary of the Thesis in French)

Un grand intérêt a été porté ces dernières années aux nanomatériaux unidimensionnels tels que les nanotubes, les nanobâtonnets et les nanofils à cause de leurs propriétés physiques intéressantes et des applications dans le domaine de l'opto-électronique qui en découlent. Cependant, il est nécessaire d'auto-assembler ces nano-objets anisotropes d'une manière orientée afin de conserver l'anisotropie des propriétés dans le dispositif. A ce jour, plusieurs techniques d'auto-assemblage orienté ont été proposées pour construire des architectures fonctionnelles complexes bien définies et de structure contrôlée.[1] On peut par exemple citer la technique de Langmuir-Blodgett,[2] le transfert de bulles de liquide,[3] ou l'utilisation de champs électriques ou magnétiques.[4] Cependant, ces techniques ne sont pas adaptées pour fabriquer des films homogènes sur une grande surface, ou ne permettent pas de former des films multicouches de structure contrôlée.

La technique couche-par-couche (*LbL, Layer-by-Layer)* est une méthode simple, flexible et efficace pour produire des structures fonctionnelles possédant des propriétés biomédicales, optiques, mécaniques ou magnétiques intéressantes.[5] Elle permet de combiner une grande variété de constituants comme par exemple des nanoparticules sphériques, des nanobâtonnets ou des nanofils dans des structures stratifiées avec un contrôle précis sur la séquence de dépôt des matériaux. Dans cette thèse, nous introduisons une nouvelle méthode d'assemblage que nous nommons « pulvérisation à angle rasant » (*GIS, Grazing Incidence Spraying)* pour la fabrication

de films mono- et multicouches de nanofils d'argent orientés. Cette méthode est basée sur la pulvérisation de la suspension de nanofils avec un angle faible sur le substrat, ce qui crée un film liquide constamment en mouvement à l'interface, induisant une force de cisaillement sur les nanofils dans la direction de l'écoulement.

Nous avons utilisé la technique de pulvérisation à angle rasant pour la fabrication de films minces de nanofils d'argent fortement orientés qui présentent des propriétés optiques fortement anisotropes. Dans la mesure où la direction d'orientation peut être choisie indépendamment pour chaque nouvelle couche, nous avons également caractérisé des nanostrucures chirales qui présentent une forte activité optique.

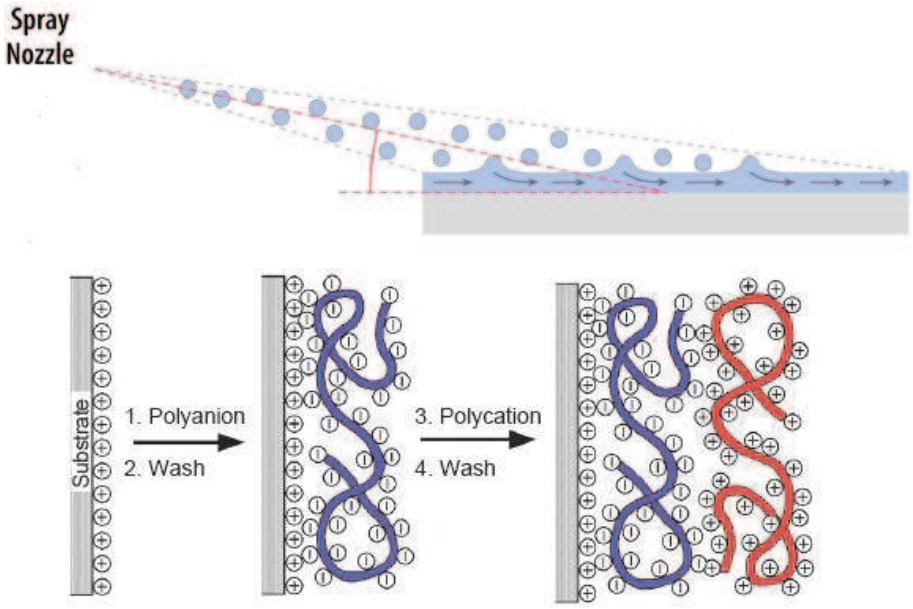

Schéma I. En haut: représentation schématique de la technique de dépôt à angle rasant (en haut) et de la technique couche-par-couche (*LbL*, en bas).

1. Film monocouche de nanofils d'argent orientés

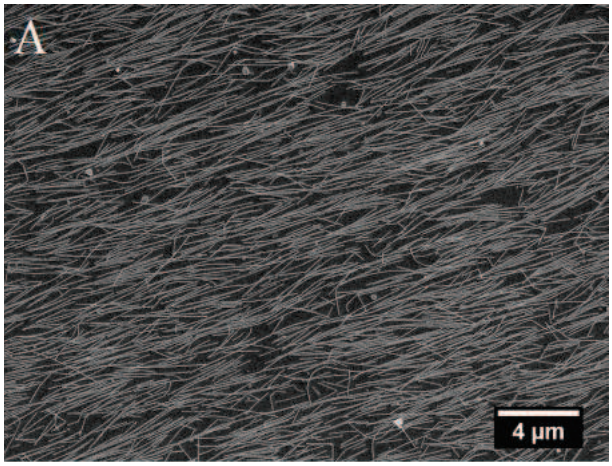
A
4 µm

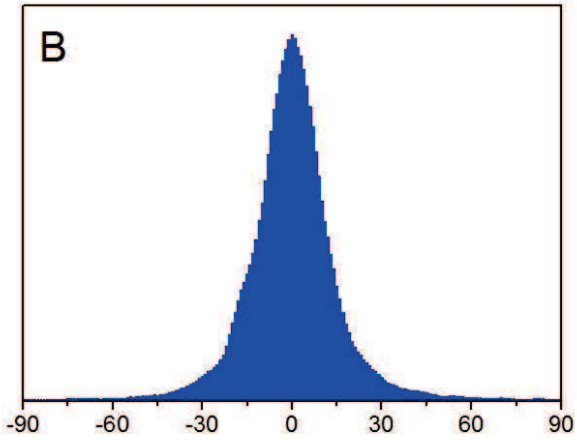
B
-90
-60
-30
0
30
60
90

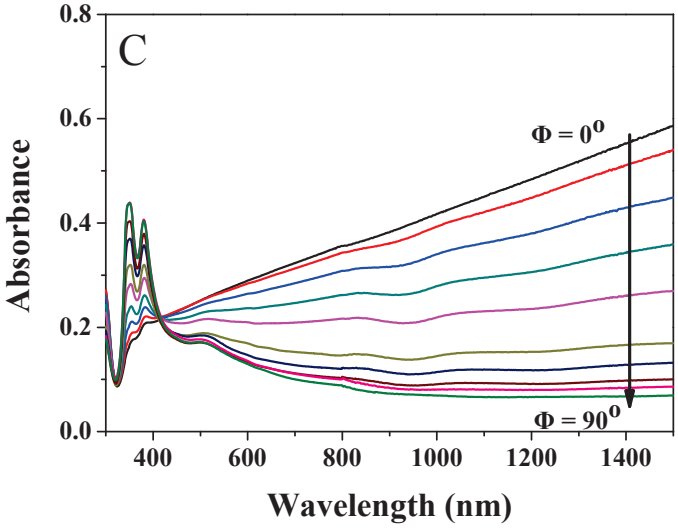
C
Absorbance
0.0
0.2
0.4
0.6
0.8
400
600
800
1000
1200
1400
Wavelength (nm)
Φ = 0°
Φ = 90°

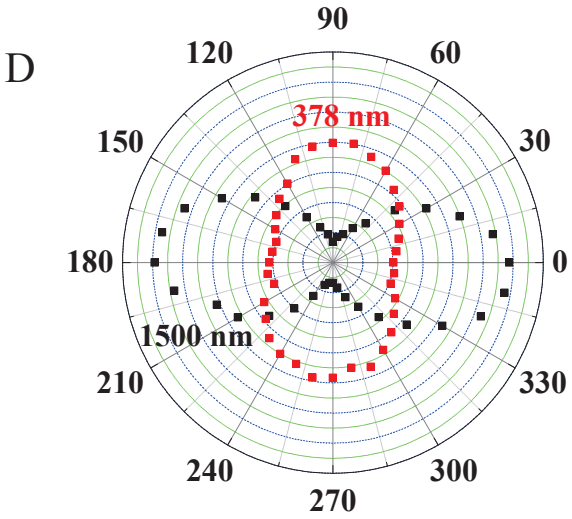

Figure I. (A) image MEB d'un film monocouche de nanofils d'argent. (B) distribution des angles entre l'axe principal des nanofils et la direction de pulvérisation. (C) absorbance UV-Visible d'un film monocouche sous lumière polarisée linéairement pour différents angles entre le plan de polarisation de la lumière et la direction d'orientation. (D) représentation polaire de l'absorbance d'une monocouche en fonction de l'angle du polariseur dans le proche UV et dans le proche infrarouge.

Les films minces orientés de nanofils d'argent ont été caractérisés par Microscopie Electronique à Balayage (MEB) (Figure IA) afin de déterminer leur morphologie. Il apparaît que les nanofils d'argent peuvent être déposés en monocouche de manière orientée, c'est à dire que les axes des nanofils pointent tous dans la direction de pulvérisation dans le plan du substrat..

Les nanofils d'argent, comme toutes les nanoparticules métalliques, expriment le phénomène de résonnance des plasmons de surface (SPR). La SPR consiste en l'oscillation résonnante des électrons de conduction à l'interface entre le métal et son environnement sous l'effet de l'excitation de la lumière incidente On peut s'attendre à ce que les propriétés optiques d'un film orienté de nanoparticules anisotropes soient elles-mêmes anisotropes. En effet, il s'avère que les propriétés optiques dépendent

fortement de la direction de polarisation de la lumière incidente. L'absorbance a été mesurée en fonction de l'angle ϕ entre le plan de polarisation de la lumière et la direction d'orientation (Figure IB). Lorsque le plan de polarisation augmente de 0° à 90°, l'absorbance dans le domaine du proche-infrarouge décroit, et celle dans le domaine du proche UV croit. En effet, à ϕ = 0°, c'est la bande SPR longitudinale dans le proche IR qui est excitée ; à l'inverse, à ϕ = 90°, le mode transverse est excité, ce qui se traduit par une absorbance dans le proche UV. Pour des angles de polarisation intermédiaires, les deux modes sont excités. L'absorbance à 1500 nm et 378 nm (qui correspond à la résonnance transverse) est représentée en fonction de l'angle du polariseur ϕ dans la Figure IC. Cette représentation souligne la sensibilité des propriétés optiques du film à la polarisation de la lumière incidente, et suggère un comportement de polariseur optique pour les films minces de nanofils d'argent orientés : dans le domaine du proche-IR, l'absorbance est maximale pour ϕ = 0° et 180° (excitation du mode longitudinal de la SPR) et un minimum à ϕ = 90° et 270°.

1. Film multicouche de nanofils d'argent orientés

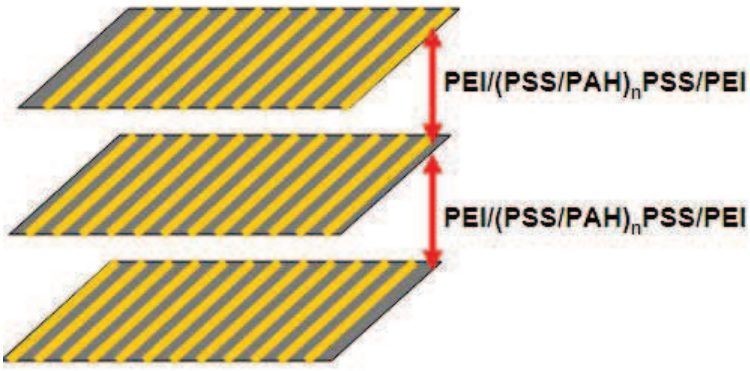

Schéma II. Structure schématique d'in film multicouche de nanofils d'argent orientés, comprenant des couches de polyelectrolytes de charges opposées entre les couches de nanofils d'argent.

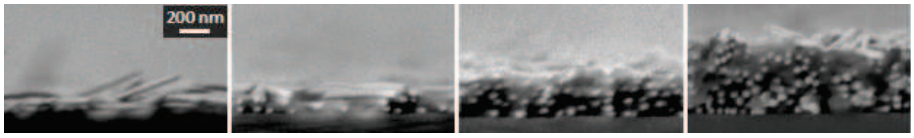

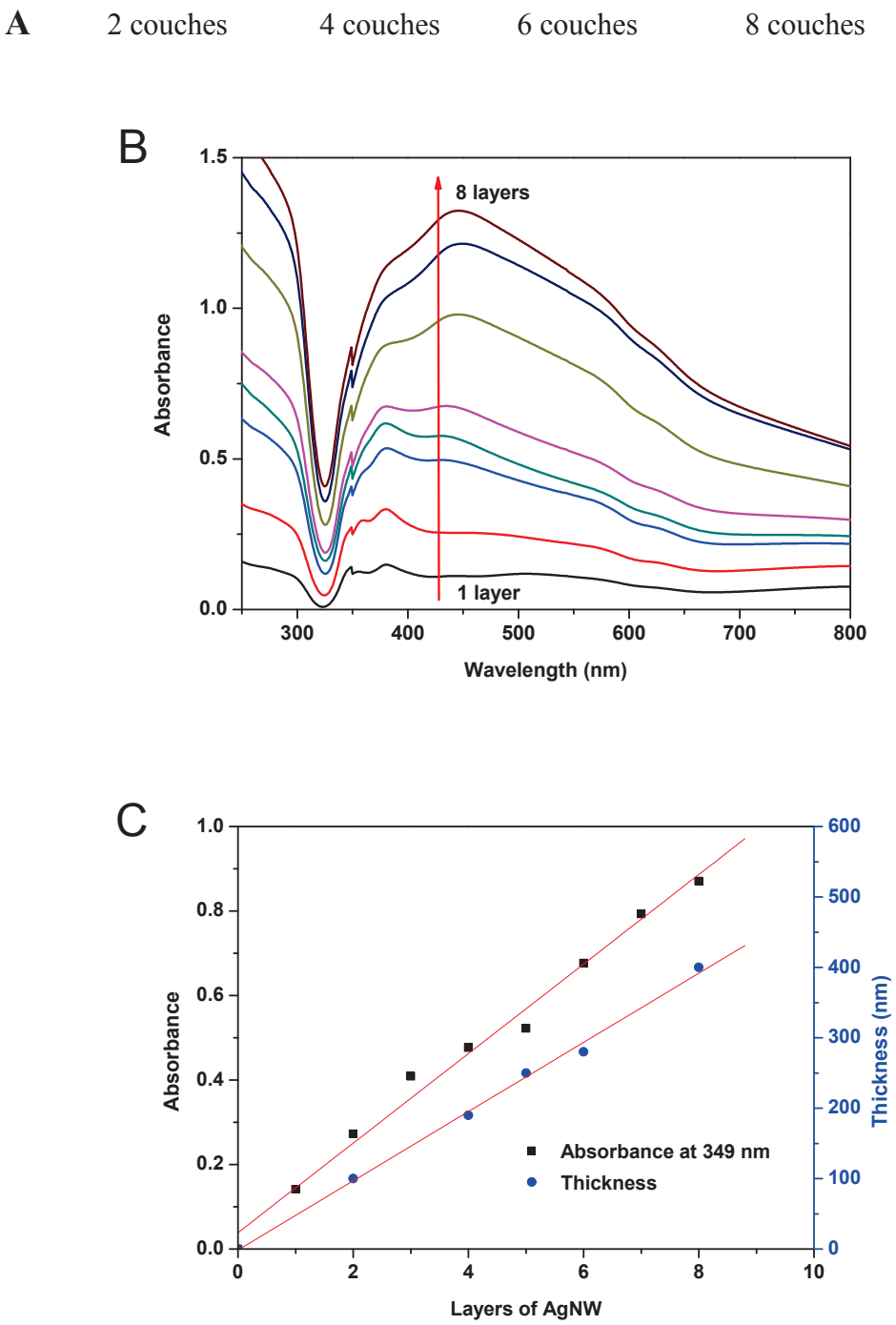

Figure II. (A) Vue en coucpe par MEB d'un films multicouches de nanofils d'argent de différentes épaisseurs. (B) spectre d'absorbance UV-Visibles pour différents nombres de couches (C) Variation de l'absorbance à 380 nm et de l'épaisseur mesurée par MEB des films en fonction du nombre de couches déposées.

La construction des films multicouches a été suivie en imageant des films de différentes épaisseurs par MEB (Figure IIA) en mesurant leur absorbance (Figure IIB). Les images MEB (Figure IIA) révèlent que l'épaisseur du film augmente linéairement avec le nombre de couches déposées, avec un incrément de 50 nm par couche de nanofils d'argent, ce qui correspond à l'épaisseur attendue pour un film multicouche de nanofils de 40 nm de diamètre recouverts de polyélectrolytes. Cette croissance linéaire du film est confirmée par l'augmentation linéaire de l'absorbance avec le nombre de couches (Figure IIC). L'absorbance augment de 0,15 unités de densité optique par couche de nanofils d'argent. La densité des nanofils dans chaque couche et l'espacement entre les couches peut être modulé facilement en jouant sur la concentration des suspensions et la durée de pulvérisation, et la quantité de polyélectrolytes insérée entre les couches d'argent respectivement.

3. Films minces chiraux de nanofils d'argent.

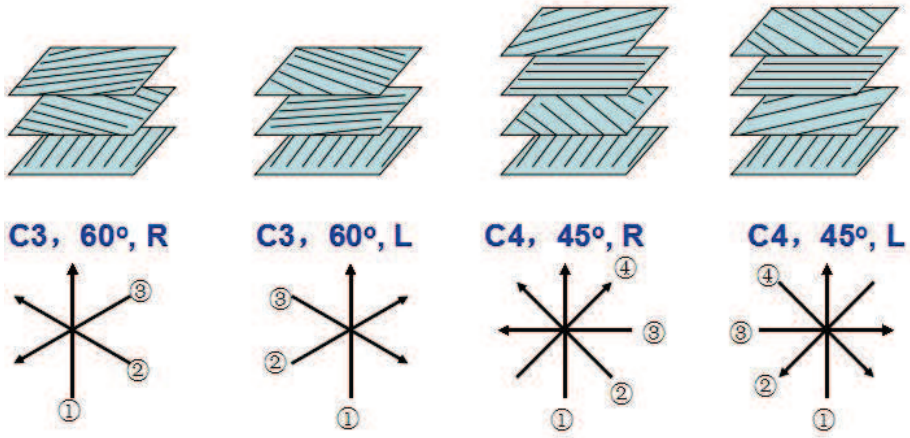

Schèma III. Illustration de la structure des films minces chiraux.

Des systèmes plasmoniques chiraux peuvent être facilement préparés avec la technique de pulvérisation à angle rasant car la direction d'orientation peut être choisie indépendamment dans chaque couche. Le Schéma III illustre la structure des films minces chiraux. Les nanofils d'argent sont orientés sur un substrat recouvert de PEI, puis des multicouches de polyélectrolytes (PSS/PAH) ont été déposées, avec une épaisseur par bicouche d'environ 3 nm. La multicouche complète peut donc

s'écrire : Substrat/PEI/AgNW/PEI/$(PSS/PAH)_n$/PSS/PEI, sur laquelle on peut déposer une nouvelle couche de nanofils d'argent avec un angle spécifique par rapport à la direction d'orientation de la première couche de fils d'argent. Afin d'obtenir une structure chirale, mais possédant une symétrie du point de vue d'une onde polarisée linéairement, des angles de 60° et 45° ont été choisis pour des films à 3 et 4 couches respectivement. De plus, il est possible de former ces structures hélicoïdales avec les deux sens de rotation possible de l'hélice. Par exemple, le dépôt de 3 couches de nanofils avec un angle de -60° entre les directions d'orientation de chaque couche conduira à une hélice gauche de symétrie C3, alors qu'un dépôt de 3 couches à +60° conduit à une hélice droite.

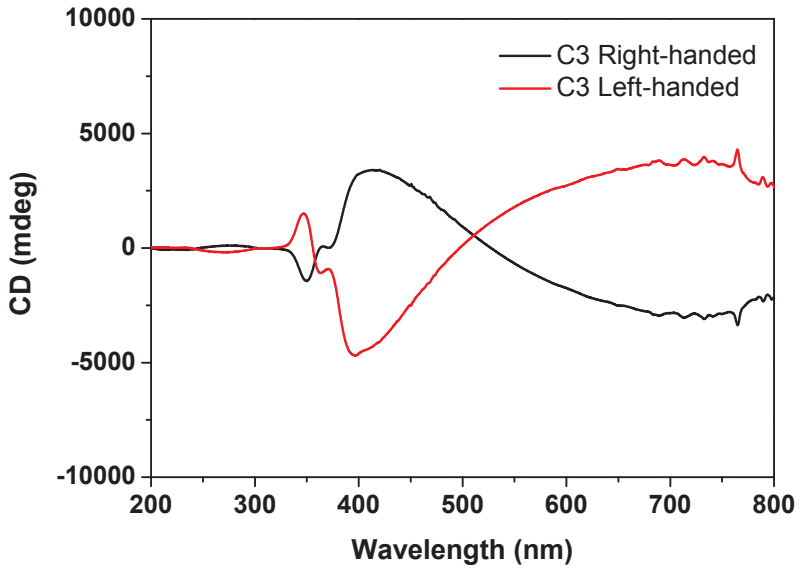

Figure III. (A) spectre CD de l'échantillon C3.

Les spectres de dichroïsme circulaire (CD) du film de symétrie C3 gauche et droite sont très symétriques (Figure III). De plus, le signal CD obtenu est très important : plusieurs milliers de mdeg, ce qui est très élevé par rapport aux valeurs obtenues ans la littérature pour des systèmes similaires.[6]

En résumé, l'objet de cette thèse est d'étudier la formation de films minces multicouches de nanofils d'argent de structure contrôlée. Les propriétés optiques de ces films ont été étudiées en détail, en particulier pour les structures chirales qui montrent une activité optique très importante

References.

1. Sajanlal, P. R.; Sreeprasad, T. S.; Samal, A. K.; Pradeep, T. *Nano Rev.* **2011**, *2*, 5883.
2. Chen, M.; Phang, I. Y.; Lee, M. R.; Yang, J. K. W.; Ling, X. Y. *Langmuir* **2013**, *29*, 7061.
3. Yu, G.; Cao, A.; Lieber, C. M. *Nature Nanotech.* **2007**, *2*, 372-377.
4. Hangarter, C. M.; Myung, N. V. *Chem. Mater.* **2005**, *17*, 1320-1324.
5. Srivastava, S.; Kotov, N. A. Composite. *Acc. Chem. Res.* **2008**, *41*, 1831-1841.
6 Kuzyk, A.; Schreiber, R.; Fan, Z.Y.; Pardatscher, G. E.; Roller, M.; Hogele, A.; Simmel, F. C.; Govorov, A. O.; Liedl, T. *Nature*, 2012, 483, 311.

1 State of art

1.1 Self-assembly of one-dimensional nanostructures

1.1.1 Introduction

One-dimensional (1D) nanoparticles such as carbon nanotubes, nanorods, nanowires, nanobelts and nanofibers have been paid wide attention in recent years because of their importance in the field of mesoscopic physics and technological applications in opto-electronic nanodevices.[1-3] With a large surface-to-volume ratio and two-dimensional confinement, nanowires show unique magnetic, optical, and electronic properties.[4-7] Moreover, the large aspect ratio of the nanowires, as a good energy transport material, can direct the conduction of particles such as photons, electrons and photons. Most deposition techniques result in randomly oriented nanowire thin films. The consequence of this is that the anisotropic properties found in individual nanoparticles is lost in the resuting assembly, which is one of the main barriers preventing their application in high-performance and low-cost devices. However, well aligned nanowires might exhibit superior properties that are not found in disordered nanowire based structures.[8] For instance, electrons can directly transport from one end to another along the aligned directions, while they might transport circularly then be wasted through the crosslinked networks contributed by the randomly oriented nanowires.[9] Thin films composed of large-area assembled one-dimensional nanostructures with well-controlled orientation, location, and spacing could lead to the next generation high-performance electronic and optoelctronic nanosystems.[10-11] Assembly of nanowire structures requires not only manipulation of individual wires but also the controlled connection from one wire to another. For low-cost applications of 1D nanomaterials, it is very important to develop suitable assembling methods for forming nanostructures thin films with good packing order. One big challenge is assembling the nanowires in desired locations to build high-order functional architechtures.

To date, a wide range of assembly strategies have been developed for assembly of

aligned nanowires on various substrates.[12] Generally, there are two main methods for the assembly of nanowire: (1) direct growth of aligned nanowires or nanofibers on to a desired substrate even at desired locations, which involves the synthesis of the nanostructures. (2) alignment of pre-grown nanowires onto a desired substrates. Here, we manly introduce the methods of alignment nanowires onto a desired substrates.

1.1.2 Various methods for assembly of nanowires

1.1.2.1 Assembly of nanowires by Langmuir-Blodgett technique

Langmuir-Blodgett (LB) technique was traditionally used to transfer monolayers of amphiphilic materials from a liquid onto a solid substrate to form a extremely thin film with high degree of order. In recent years, this technique has been shown to be a low-cost, easily integrated method to assemble nanomaterials, including nanoparticles,[13] nanorods, nanowires, nanotubes, and even two-dimensional nanosheets.[14] The process of the LB techinique for alignment of nanowires is illustrated in Figure 1A.[15] Nanomaterials were first dissolved in an volatile solvent and spread onto a water surface using a microsyringe. After solvent evaporation, the sample was compressed slowly with a barrier while the surface pressure was monitored. The nanowires are close-packed with their longitudinal axis aligned perpendicular to the compression direction and a Langmuir thin film consisting of a nanostructure monolayer can be obtained.[16] For instance, Yu et al. aligned the hydrophilic flexible Te nanowires with aspect ratios of about 10^4 with the LB technique. They first dissolved the Te nanowires in N,N-dimethylformamide (DMF) and then added to a mixture of DMF and chloroform. Packing the arrayed nanowire monolayers makes it possible to construct nanomesh-like nanostructures or more complex multilayerd structures composed of ultrathin nanowires on a planar substrate by simply controlling the rotation angle (Figure 1B-D).[17] Whang et al. have successfully aligned silica nanowire monolayers via the LB technique, as shown in Figure 1E-G. The spacing of the transferred nanowires is controlled from micrometer scale to well-ordered and close-packed structures by the compression process. Furthermore, hierarchical structures can also be produced by repeating the assembly

process after changing the orientation of the structure.[18] Lieber and his co-workers used this technique to align silicon nanowires and integrate them into nanowire-based field-effect transistors.[19] A uniform parallel layer of aligned nanowires with a average spacing was transferred from nanowires monolayers at the air-water interface to a substrate surface. Centimeter-scale arrays contains lots of silicon nanowire field-effect transistors were prepared by pressing complementary electrode arrays onto the nanowire patterns.

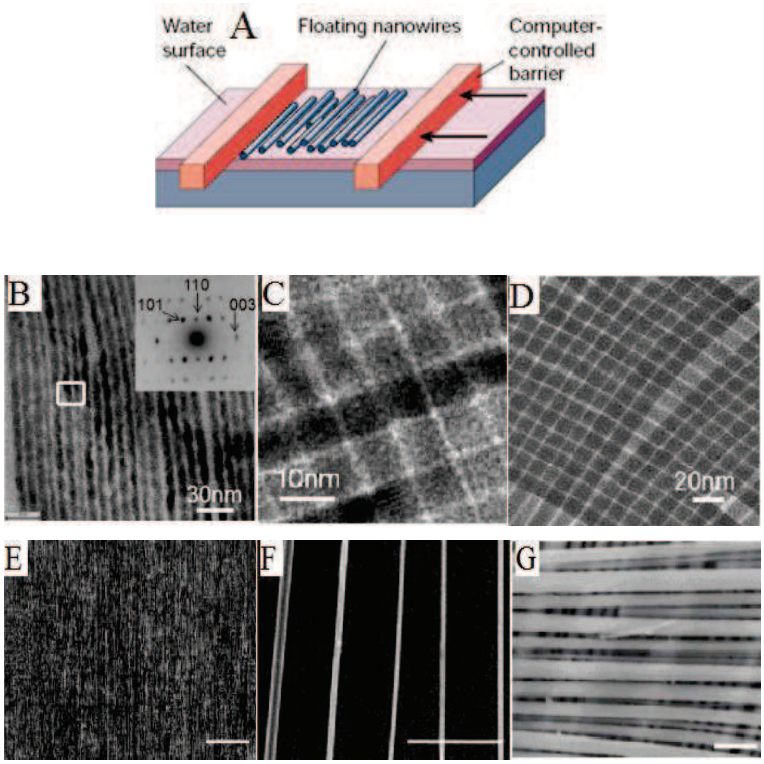

Figure 1. (A) Schematic processes of the LB assembly.[15] (B) TEM image of the monolayer assembly of Te nanowires. (C) TEM image of crossed Te nanowires. (D) TEM image of crossed layers of Ag_2Te nanowires.[17] (E and F) SEM images of an LB assembly of aligned Si nanowires (scale bar in E: 100 μm; scale bar in F: 100 μm). (G) SEM image of an high-density crossed nanowire array (scale bar: 200 nm).[18]

1.1.2.2 Evaporation-mediated assembly of nanowire

The dynamics of evaporation are rather complicated and involve many challenging problems in physic, however, the assembly induced by evaporation are very common. Usually, the solvent evaporation rate is believed to be critical factor for the formation of these well-ordered structures. In the recent years, this simple assembly method, which was conveniently named as drying-assisted or evaporation-mediated assembly, has been widely used in the self-assembly of spherical and the anisotropic nanoparticles on solid substrate.[20-21] A schematic representation of evaporation mediated assembly of nanorods on a substrate is shown in Figure 2.[22] In general, when a liquid droplet is placed in contact with a substrate, the interfacial forces are inclined to drive the droplet spreading until an equilibrium, then the solvent is subsequently evaporated in a controlled manner, and the relatively weak interactions such as the van der Waals forces, dipole-dipole interactions between the dispersed nanoparticles become more obvious as the volume of the droplet is reduced, driving the nanoparticles to self-assembly.

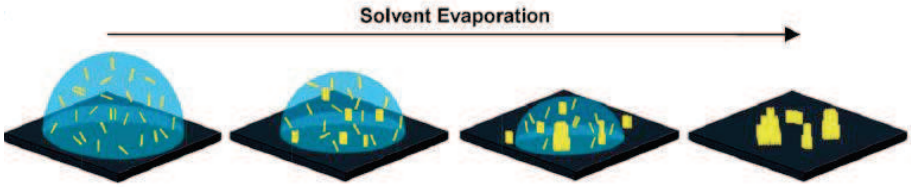

Figure 2. Schematic illustration of evaporation-mediated assembly.[22]

Here we take some recently reported evaporation driving nanowire organization as examples. Yan and co-workers[23] reported the preparation of thin nanowires with a diameter of about 1.8 nm and length up to several micrometers. The ultrathin nanowires could spontaneously organized into three-dimensional superstructures via a parallel arrangement after evaporation of a mixture composed of ethanol and cyclohexane. Welland et al.[24] reported a self-asembly approach induced by evaporation to make protein fibrils films. The films were highly rigid and well-aligned, the Young's modulus is up to 5-7 GPa, which is almost the highest values for protein materials. In brief, the films were prepared by transferring certain

amount of nanowires containg hydrogel onto a flat substrae; the solvent and the volatile acid were evaporated for 24 hours and the resulting protein films could be removed by tweezers. Choi et al.[25] reported a nanowire self-assembly procedure during the evaporation of a colloid droplet of nanowires on the superhydrophobic surfaces, the orientation of nanowires is achieved by the interactions between the hydrophobic surface and the nanowires.

Recently, Yu and co-workers developed a novel three-phase-interface assembly method to produce free-standing ordered silver nanowire thin films.[26] Figure 3A and B shows the SEM images of random oriented silver nanowires and the aligned Ag nanowires after assembly. With this facile approach, silver nanowires were close-packed and oriented parallel to each other. The self-assembly process was conducted by dropping an appropriate amount of silver nanowire aqueous solution onto the surface of chloroform. The formation of silver nanowire by this three-phase-interface method is illustrated from Figure 3C-E, the corresponding experimental photographs of the steps are shown from Figure 3F-I. Initially, the Ag nanowires transferred step-by-step from the water-oil interface to the water-air interface through the oil-water-air line. Second, the silver nanowires at the water-air interface self-organized, first at the contact line at the contact line of the wall of the container and the water phase, which can be denoted as water-air-substrate interface. Third, the film of the silver nanowires at the water-air-interface grew into a film. Finally, the silver nanowire covered the whole water-air interface to form a well-aligned silver nanowire film. So the three-phase interface plays a key role in the orientation process, and could drive the movement and self-assembly behavior of the silver nanowires. Also, the same lab reported a water-oil interface assembly strategy to prepare large-area nanofilms composed of various nanobuilding blocks at room temperature, including nanoparticles, nanocubes, nanosheets and nanowires.[27] A family of water/oil interface could provide effective platforms for rapid fabrication of nanofilms to deepen the impression of assembly at nanoscales. Several kinds of substrates could be selected to transfer the nanofilms, and the thickness of the films could be adjusted by Layer-by-Layer dipping.

Lee and the co-workers reported[28] a simple one-step process for aligning organic nanowires at the organic solvent/water interface. Solvent evaporation plays a very important role in the assembly procedure. As the dichloromethane evaporated, the organic nanowires was trapped at the DCM/water interface because of the compression force. The density of the nanowires increased as more DCM evaporated and then the DCM/water interface continuously shrink. When the solvent was evaporated completely, a compact monolayer of well-aligned nanowires was formed on the water surface. As a result, the disorderd nanowired were compressed into an ordered way. These films can be transferred onto a desired substrate or Layer-by-Layer stacked to form a multilayered film.

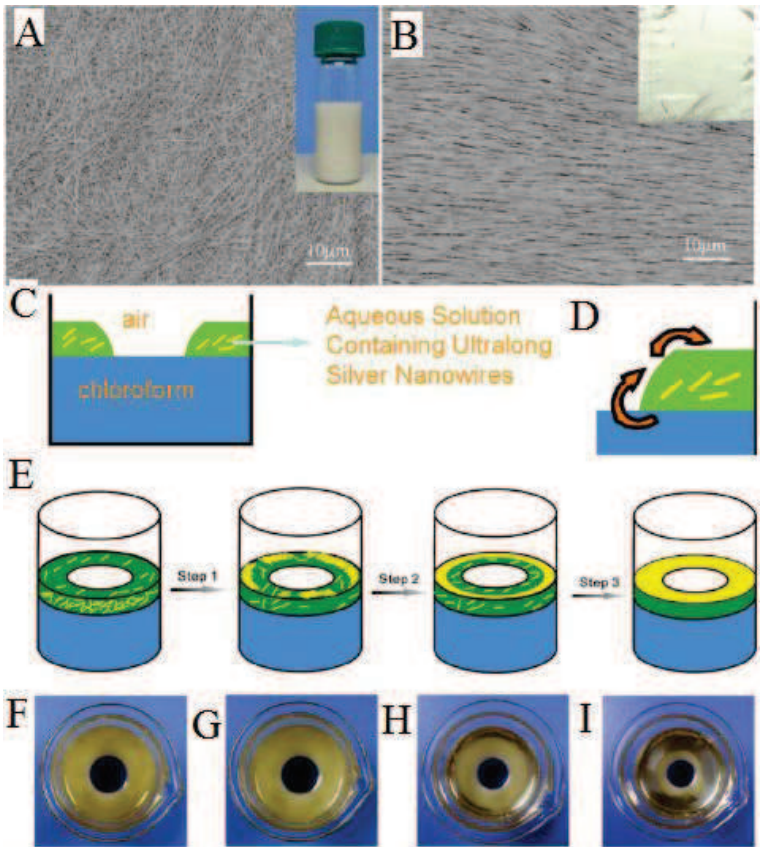

Figure 3. (A) SEM image of the random oriented Ag nanowires. (B) SEM image of the aligned nanowires. (C) Cross section of the three-phase interface. (D) Schematic illustration of the movement of the Ag nanowires with the evaporation of the oil phase. (E) Schematic representation of the stages of formation of the Ag nanowire film at the three-phase interface. (F-I) Corresponding experimental photographs of the steps shown in E.[26]

1.1.2.3 External-field-directed assembly of one-dimensional structures

The use of an applied external field (e.g. Magnetic, electric) in facilitating the assembly of colloidal nanoparticles has been paid wide attention recently. The ability of an external field to direct the assembly of nanostructures is especially good for the alignment of anisotropic nanostructures. Under the influence of an external field, 1D nanostructures align with the longitudinal axis parallel to the direction of the field line.

1.1.2.3.1 *Magnetic-field*

A magnetic field is the magnetic effect of electric currents and magnetic materials. It can be produced by moving electric charges and the intrinsic magnetic moments of elementary particles associated with a fundamental quantum. An interesting phenomenon of the magnetic fields is that it can be used for by migratory navigation and homing animals. The nanostructures can be polarized like a bar magnet under the external magnetic induction, which implies that the external magnetic field can direct the assembly behaviors of the nanostructures. Fragouli[29] et al. reported a simple technique for magnetic-field-induced formation, assembling, and positioning of magnetic nanowires in a polymer film. The control of the dimension of the nanowires and of their localization across the polymer matrix can be achieved by varying the duration of the applied magnetic field, in combination with the evaporation dynamics. Figure 4A shows the scheme of the fabrication approach. The well-aligned film is fabricated by exposing nanosized building blocks with a certain concentration to an

external magnetic field. Figure 4B-E shows the optical microscope pictures of various NP/polymer composite assemblies. The polymer matrix also plays a very important role in the assembly process since it induces the aggregation process in the initial stage of formation and defines a viscosity gradient in the film volume, contributing to the irreversible formation of well-determined NWs at specific depths in the film. The obtained films can show anisotropic magnetic property, with higher magnetization in the direction of the NWs growth.

Chen and co-workers[30] showed a approach combing arc-discharge growth with magnetic-field-induced orientation to prepare well-aligned and closely packed single-walled carbon nanotube (SWNT) films on various substrates. This approach involves electrical arc-discharge growth of SWNTs, diffusion and alignment of the SWNTs in a parallel magnetic field, then deposition of these oriented SWNTs on substrates at the desired orientation and location. Figure 5 A illustrates the fabrication process of closely packed SWNT films on a substrate. The film structure, area, location, thickness, orientation can all be well controlled. Also, the evaporation coating character can also enable a adjustable deposition of aligned SWNT films with desired shapes by controlling the parameter of deposition. So, various patterned structures with oriented SWNTs on a designated area can be fabricated directly by employing the commonly used mask technique in vacuum evaporation coating. Since the alignment of the SWNT film is only determined by the relative direction between applied magnetic field and substrate, the alignment orientation of SWNTs can be easily tuned by changing the direction of the substrate. Thus, multilayers and three-dimensional architectures with each layer has the different orientation direction and location can be prepared simply by adjusting the orientation and location of the receiving substrate.

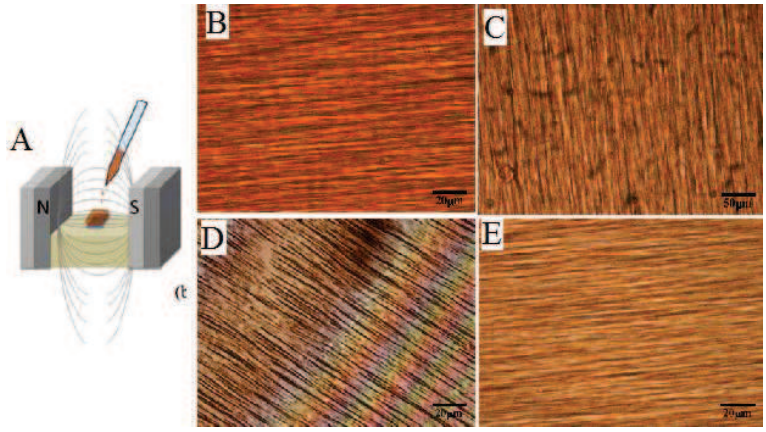

Figure 4. (A) Scheme of the magnetic-induced assembly method. (B-E) Optical microscope images of various colloidal NPs/polymer assemblies. (scale bar: 20 μm) (B) 1% wt. γ-Fe_2O_3 in 99% wt. of poly(methylmethacrylate) (PMMA). (scale bar: 50 μm) (C) 1% wt. γ-Fe_2O_3 in 99% wt. of polystyrene (PS). (scale bar: 20 μm) (D) 2% wt. γ-Fe_2O_3 in 98% wt. of poly[3-3'(vinylcarbazole)] (PVK). (E) 1% wt. Fe_2O_3-TiO_2 heterostructures in 99% wt. of PEMMA.[29] (scale bar: 20 μm)

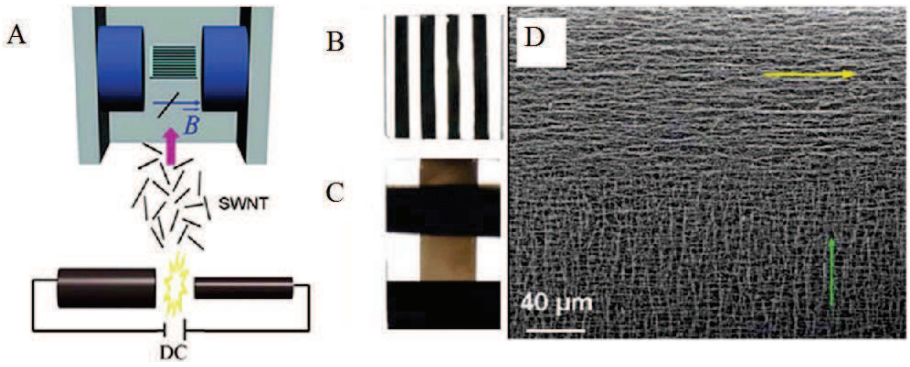

Figure 5. (A) Scheme of fabrication of well-aligned and closely packed SWNT film on an arbitrary substrate with a magnetic field. (B) Photograph of patterned, aligned SWNT films On glass slide. (C) Photograph of the 3D structure of aligned SWNTs with different orientations. (D) SEM image of a two-layered deposited aligned SWNT film with a different orientation.[30]

1.1.2.3.2 *Electric-field*

The alignment of one-dimensional nanostructures induced by the electric field is very

interesting since the possibility of prepare oriented 1D nanostructures in a desired region between the electrodes. When nanowires exhibit conductive behavior or a charged condition, an applied electric field will induce dipoles and force them towards the region with highest field gradient. So, the nanowires are aligned along the electrical field direction.

Figure 6 shows a example of experimental setup that has been used in orientation of colloidal nanorods under direct current.[31] In general, a conducting substrate is placed between parallel electrodes that are arranged in a top-down manner. The nanorod suspension is dropped onto the substrate and the solvent is slowly evaporated for several hours with a direct voltage of sufficient magnitude is applied. When placed under the influence of an external electric field, the nanorods rotate to align the long axis with the field direction. The rods can align over large areas by following the field streamlines throughout the electrode gap.[32] The position of the electrodes determines the direction of the electric field and thus influence the final alignment of the nanorods in relate to the substrate. Furthermore, controlled the solvent evaporation assists the close-packing of the aligned nanorods and the degree of positional order is dependent on the evaporation rate. With a slower rate of solvent evaporation, a higher degree of positional order is observed.[31]

Alternating current (AC) electric fields can also be used to assemble the 1D nanostructures. An advantage of the AC electric field is that it can avoids the eletrochemical effects. Mayer and co-workers[33] have demonstrated the assembly of gold nanowires dispersed in a dielectric medium using an alternating current. The gold nanowires are easily polarized in the electric field due to charge separation at the nanowire surface. The nanowire orientation can be influenced by the frequency of the alternating voltage. As the frequency of the alternating voltage increased, the time of alignment decreased.

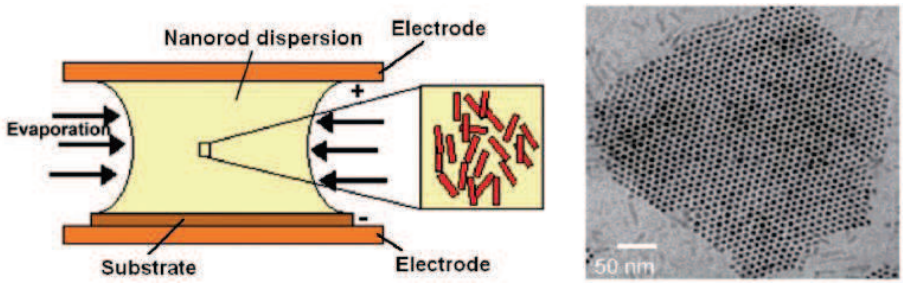

Figure 6. Top-down arrangement of electrodes yields nanorods that are oriented perpendicular to the substrate. TEM image shows vertically oriented nanorods.[31]

1.1.2.4 Assembly by microfluidic and microchannels

Microchannels are able to provide directional shear force along the flowing direction, which might serve as the driving force to affect the interactions of the 1D nanostructures and orients them parallel to the flowing direction. First, a homogeneous nanowire suspension is prepared, when the suspensions pass through a microfluidic channels, nanowires are integrated.[34] The nanowire are aligned along the flow direction because the shear force, and the density of assembled nanowires is controlled by the concentration of nanowires and flow time. The degree of alignment can be controlled by the flow rate, since higher flow rate produce larger shear forces and lead to better alignment. The average nanowire coverage can be controlled by the flow duration. Complex architectures such as mesh-like arrays can be fabricated through a layer-by-layer process. Lieber and co-workers[34] reported this method for hierarchical assembly of one-dimensional nanostructures into well-defined functional networks with this method. A poly(dimethylsiloxane) mold with a microchannel whose width ranging from 50 to 500 μm and length from 6 to 20 mm is contact with a flat substrate (Figure 7A). Nanowires can be aligned by passing a suspension of nanowires through the microfluidic channel structures (Figure 7B). Crossed NW arrays were also fabricated by layer-by-layer assembly of silver nanowire from different direction (Figure 7C).

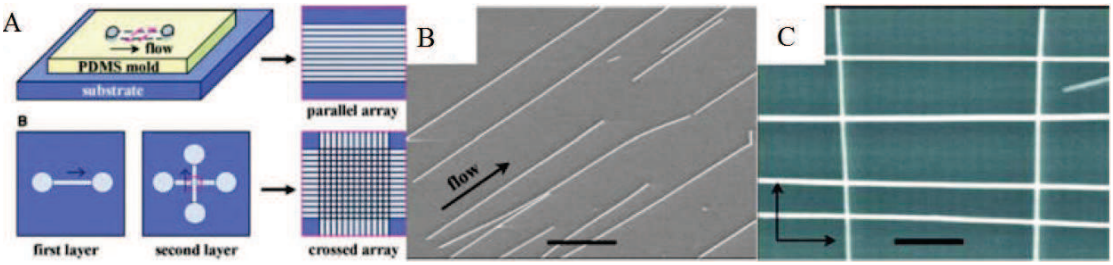

Figure 7. (A) Schematic of fluidic channel structures for the assembly. (B) Parallel arrays of NWs assembly was obtained by flowing NW suspension inside the channel (scale bar: 2 μm). (C) Multiple crossed NW arrays can obtained by changing the flowing direction (scale bar: 500 nm).[34]

Templates with designed geometrically channels, can create different assembly patterns. Design of the template needs to be in accordance with the structure of the one-dimensional structures. The size and morphology of the template depends strictly on the way of the one-dimensional nanostructures deposited on the it. For instance, Russell and co-workers[35] used a block copolymer thin film with nanochannels lying parallel to an underlying substrate to align the CdSe nanorods along the channel walls (Figure 8). A film flotation method was used where the template channels were exposed to the surface of the aqueous nanorod suspension for 10-12 hours. After this, the CdSe nanorods accumulated in the channels and on the surface of the template. The nanorods on the surface of template can be removed by rinsing with water, leaving the nanorods that are confined in the channels. The length of the nanorods relative to the channel width is very important for the orientation and the position of the rods. A channel width that is too small would have the problem to confine of the rods within the channels while and excessively large width would lead to a random orientation of the rods.

Also, the substrates with chemically functionalized surfaces can be used to assemble the one-dimensional structures. For example, a chemically functionalized template whose surface has been designed with special regions having different affinities was used to align functionalized colloidal gold nanorods with controlled position and

orientation.[36] Bao and co-workers[37] also used this method to assemble water-dispersible Pd nanorods (Figure 9). First, a drop of the aqueous nanorod suspension is deposited on a template, which has been functionalized into alternating hydrophilic and hydrophobic stripes through microcontact printing. The nanorods are then allowed to deposited near the template surface and the excess suspension was removed by a pipette, leaving the droplets that are selectively deposited on the hydrophilic position of the template. Once the water has completely evaporated, nanorods are confined within the hydrophilic region of the template. The width of the hydrophilic stripes relative to the nanorod length is adjusted in order to align the nanorods. Nanorod can be aligned when the width of the hydrophilic stripes is less than the length of the nanorods.

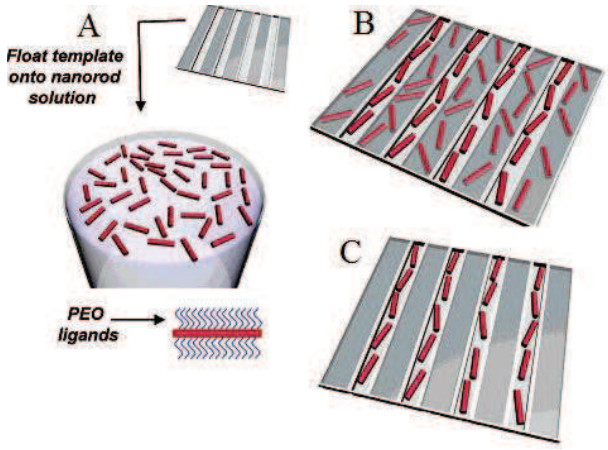

Figure 8. Schematic representation of template-assisted assembly of nanorods based on geometric confinement.[35]

Recently, Yu and co-workers[38] ordered silver nanowires with a glass capillary (Figure 10). The Ag nanowires with high aspect ratio were aligned by flowing through a glass capillary. By controlling the flow parameters such as flow rate, flow distance and the concentration of Ag nanowire suspension, initially random Ag nanowires can be aligned to form nanowire arrays with tunable density, forming cambered nanowire films adhered onto the inner wall of the capillary. The glass capillary with well-aligned silver nanowire films inside can serve as a portable and reusable

substrate for surface-enhanced Raman spectroscopy (SERS), which may provide a promising platform for detecting mixture pollutions.

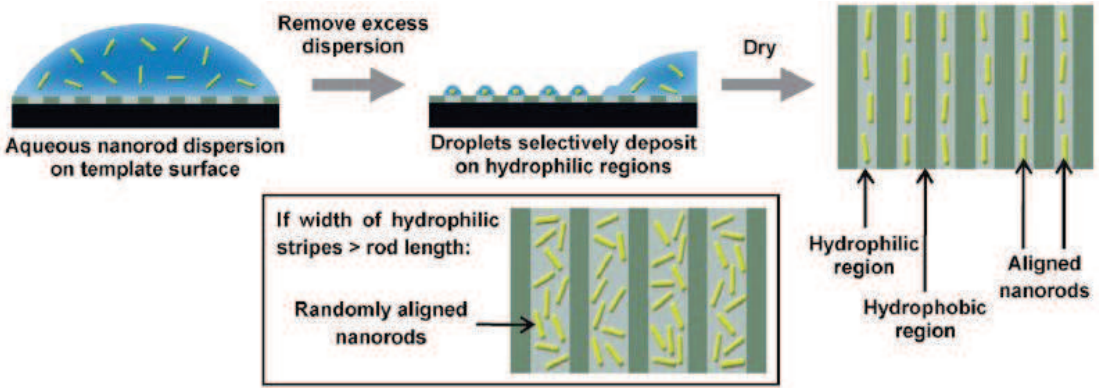

Figure 9. A template with surface patterned into hydrophilic and hydrophobic regions is used to confine and align nanorods within the hydrophilic regions.[37]

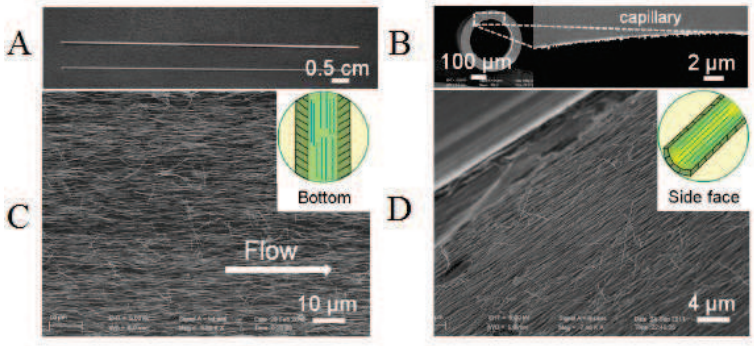

Figure 10. Well-aligned Ag nanowire films with curvature were obtained by an capillary. (A) Photograph of two capillarys, upper one with the aligned Ag nanowires and down one is the naked capillary. (B) SEM images of the cross section of capillary with Ag nanowire aligned inside. (C, D) SEM images of as obtained silver nanowire assemblies at the bottom and side face of side face of the capillary in wall.[38]

Wang and co-researchers[39] also used the glass capillary to align various nanoparticles (Figure 11), including tobacco mosaic virus, gold nanorods, and bacteriophage M13,

were aligned inside a glass tubes functionalized with several kinds of polymers. The properties of 1D nanoparticles, such as stiffness and aspect ratio, play a critical role in the alignment. In general, a better aligned structure can be produced when longer and stiffer nanoparticles are used at higher flow rate and higher concentration. Furthermore, these hierarchically organized structures can be used to support cell growth and control the cell orientation and morphology.

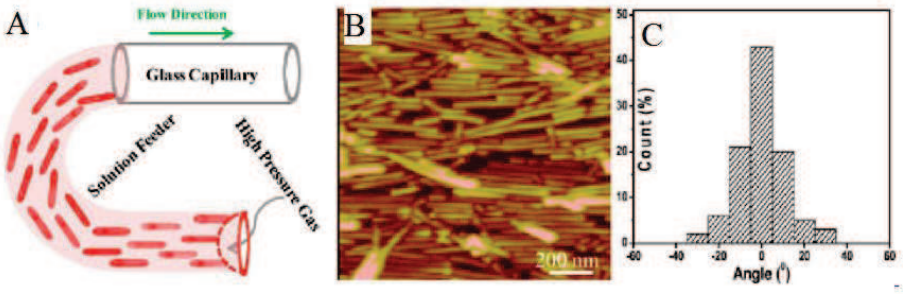

Figure 11. (A) Schematic illustration of experimental setup. One end of feeder is connected to the capillary, while the other end is kept open for filling of 1D NP solutions and subsequent high pressure gas. (B) AFM image of aligned TMV on the inner surface of a capillary tube after the flow assembly. (C) A histogram of TMV angular spread distribution with respect to flow direction.[39]

1.1.2.5 Assembly within bubble blowing films

Blown film extrusion is the normal method to make polymer films, especially for the preparation of plastic films in large quantities, which involves extruding a molten polymer and blowing it to form a balloon, which can be collapsed and form continuous flat films. Recently, Yu et al.[40] have used a general method for preparing well-aligned and density controlled nanowire and nanotube films over large areas. Figure 12A shows the basic three steps for the alignment: first, preparation of a stable, homogenous and controlled concentration polymer suspension dispersed with nanowires and nanotubes. Then expansion of the polymer suspension happens, using a circular die to form a bubble with a controlled pressure, P, and expansion rate, where

stable vertical expansion is achieved using an external vertical force. The nanowires or nanotubes within the film align along the shear force created by expansion of the film. Lastly, the bubble films were transferred to the substrates. Figure 12B shows the bubble expansion process, the ring visible at the top of the bubble moves upwards at a constant speed during expansion. The shear stress associated the suspension passing through the die could oriented the high-aspect-ratio nanowires in a polymer suspension along the principal direction of strain. Besides oriented silica nanowires, CdS nanowires as well as modified carbon nanotubes have also been transferred to a broad range of rigid or flexible substrates with excellent orientational alignment such as curved surfaces (Figure 12C). The transferred nanowire or nanotube density on the film can be controlled by the concentration of the nanoparticle in the polymer suspension. Large nanowire field-effect transistor arrays can also show excellent performance when they are prepared by transferring Si nanowire blown-bubble films on plastic substrates.

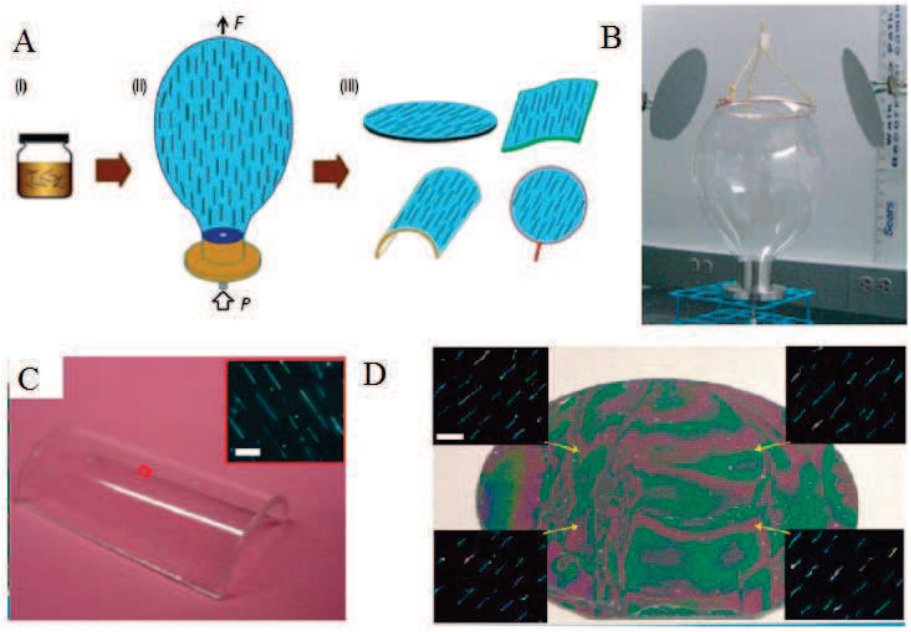

Figure 12. (A) Illustration of blown-bubble film (BBF) process. (B) Photographs of the directed bubble expansion. (C) A curved surface. Inset, dark-field optical image showing Si NWs in the film. (scale bar: 10 μm) (D) Image of 0.10 wt% silicon-nanowire blown bubble film transferred to Si wafer. (scale bar: 10 μm)[40]

1.1.2.6 Assembly by Electrospinning

Electrospinning uses an electrical charge to prepare very fine fibers from a liquid. Electrospinning shares characteristics of both electrospraying and conventional solution dry spinning of fibers. The standard setup for electrospinning consists of spinneret connected to a high-voltage (5 to 50 kV) direct current power supply, a syringe pump, and a grounded collector[41] (Figure 13). A sol-gel, polymer solution, particulate suspension or melt is loaded into the syringe and this liquid is extruded from the needle at a constant speed by a syringe pump. Alternatively, the droplet at the tip of the spinneret can be replenished from a header tank providing a constant feed pressure. However, the random orientation of fibers prepared by the conventional electrospinning may limit the potential application of the fibers, especially in the fields of electronics and photonics which need direct, fast charge transfer and uniform structures. In order to solve this, lots of strategies have been developed, such as pair electrodes collection, magnetic field collection and rotation of collection.

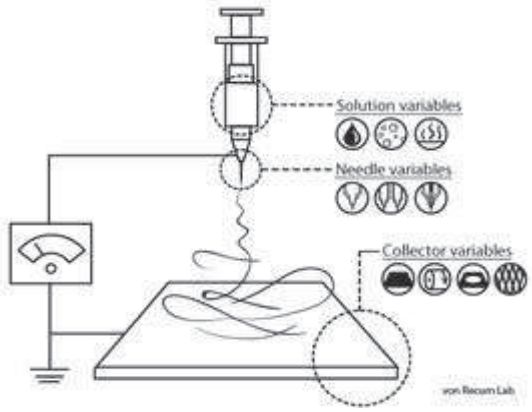

Figure 13. Illustration of electrospinning process.[41]

The Xia group[42] reported a developed electrospinning process for fabricating uniaxially aligned nanofibers with various compositions. In order to aligned the nanowire in parallel to each other, the conventional receiver electrode was cut into two pieces, which were separated with a gap. When the receiver was modified by pairing gold electrodes patterned on the insulating substrate and alternatively grounding (Figure 14A), a double-layered mesh-like network of nanowires can be obtained (Figure 14B).

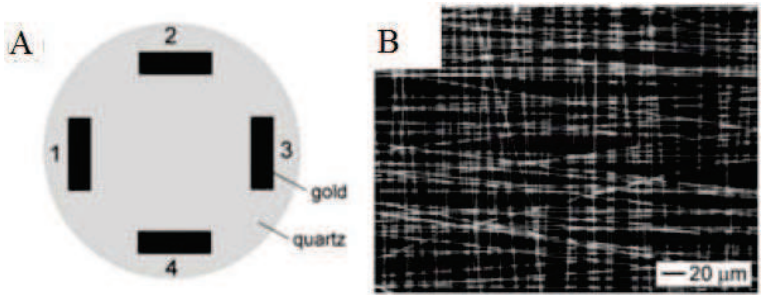

Figure 14. (A) Illustration of electrospinning with a test pattern consisting of four gold electrodes. (B) Optical image of a mesh-like network made of PVP nanofibers.[42]

Recently, Yang and co-researchers used the electrode collectors modified with the magnetic or electric field to align nanowires.[43] The schematic setup of electrospinning with the collectors modified by magnetic field was shown in Figure 15A. The SEM image of Figure 15B showed the uniaxially aligned PLGA fibers collected for 2 hours. The magnetic field could produce an additional force and increase the speed of the jet reaching a substrate. The advantage of the external magnetic field to fabricated aligned nanofibers is that the alignment can be maintained for thick membranes.

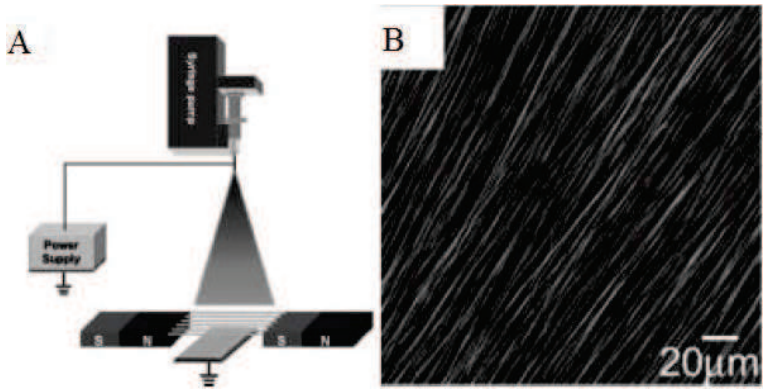

Figure 15. (A) Illustration of electrospinning modified by magnetic field. (B) SEM image of the PVP fibers obtained by this method.[43]

Besides the electrodes, the high-speed rollers have also been used as collector for anisotropic eletrospinning. Aligned nanofibers could be fabricated by electrospinning with a rotating disk collector.[44] Figure 16A illustrate the setup for preparation of aligned nanofibers by the electrospinning with a rotating collector. The linear rate of the rotation at the edge was 11 m/s. Figure 16B showed the optical micrographs of the aligned fibers. Most fibers were aligned along the longitudinal axis, which form a a unique oriented topography.

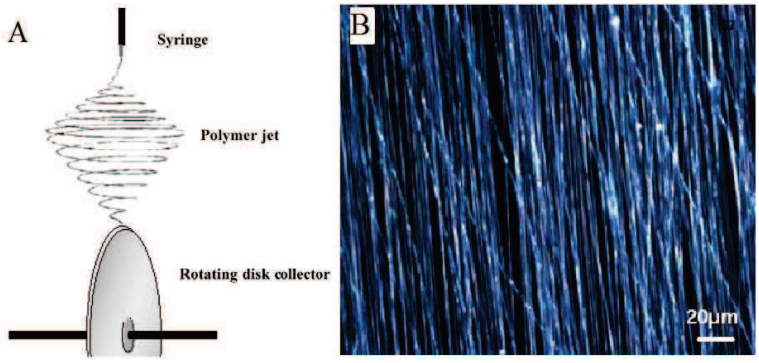

Figure 16. (A) Illustration of setup for fabrication of aligned nanofibers by electrospinning with a rotating disk collector. (B) Optical micrograph of aligned organic nanofibers.[44]

1.1.2.7 Assembly Induced by another nanostructures

Some nanowires can be aligned with some appropriate materials at the interface, the interaction between the nanowires and the assistant materials can direct the orientation of the nanowires. Figure 17[45] shows a novel approach for the assembly of one-dimensional hybrid nanostructures that consist of gold nanowires with ultrahigh aspect ratio (L/d > 500) aligned along the axes of multiwalled carbon nanotubes. This self-assembly behavior of oleylamine-coated Au nanowires along sidewalls of carbon nanotubes.

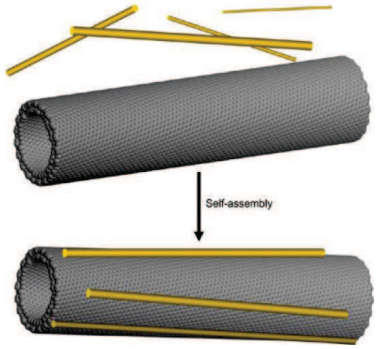

Figure 17. General scheme of Au nanowire self-assembly onto CNTs.[45]

Hwang et al.[46] Followed the assembly of collagen on muscovite mica at a concentration lower than the critical fibrillogenesis concentration (Figure 18). Initially, individual collagen molecules adsorb to mica and subsequently nucleate into fibrils lead to the alignment of fibrils in parallel to each other. Comparing collagen assembly on the two kinds of mica at different potassium concentrations revealed that potassium binds to the negatively charged mica surface and neutralizes it, and reducing the binding affinity of collagen and enhancing surface diffusion. These results indicated that collagen alignment on mica follows the surface adsorption, diffusion, nucleation, and growth route.

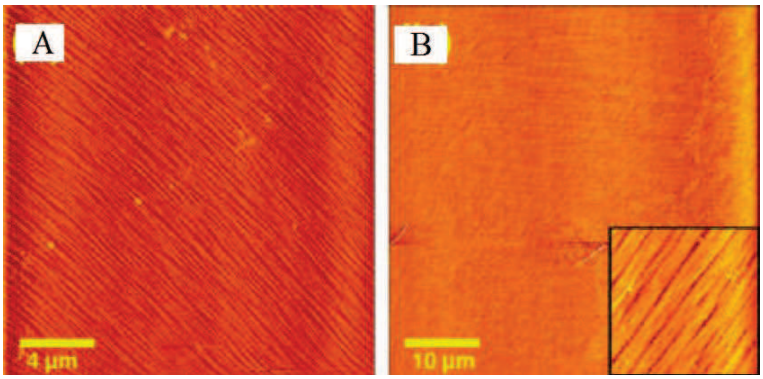

Figure 18. Highly aligned collagen fibrils on muscovite mica. [KCl] = 200 mM. (A) 10 µg/mL collagen and 1 min of incubation. (B) 50 µg/mL collagen and 108 min of incubation.[46]

Wu and co-workers[47] studied the co-assembly behavior of graphene oxide (GO) nanosheets and $Na_{0.44}MnO_2$ nanowires (Figure 19). As the addition of GO nanosheets to the nanowire aqueous suspension, the nanowires oriented gradually at the air-water interface. The aligned nanowires can be transferred to hydrophilic substrates with the orientation parallel to the liquid-substrate contact line upon evaporation of the solvent. In this case, the GO nanosheets can be considered at two- dimensional macromolecules, it can adsorb onto the nanowire surface through hydrogen-bonding and ion-dipole interactions. As a result, the GO-adsorbed nanowires become surface active and enriched at the air-water surface. The adsorption of GO also increases the negative surface charge density of the nanowires and further stabilized the solution. When a critical concentration is reached, the nanowires aligned.

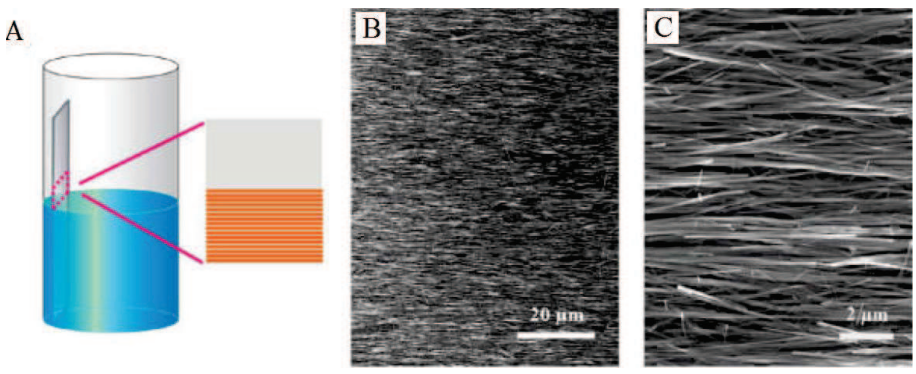

Figure 19. Nanowire alignment with GO on a Si substrate. (A) The scheme describing setup: a piece of cleaned Si wafer is immersed into the nanowire/GO solution. With solution evaporation, aligned nanowire is deposited on the substrate with the orientation parallel to the horizontal liquid-substrate contact line. (B-C) SEM images of nanowire alignment.[47]

1.1.3 Applications of the oriented nanowire films

1.1.3.1 SERS sensing

Yu et al.[38] aligned the silver nanowires in a glass capillary. Since the existence of the large electromagnetic field, the oriented silver nanowire films can be used as an active platform for SERS detection. The enhanced electric field around the noble metal nanostructures is considered to be the main factor for the SERS enhancement. Figure 20A shows the illustration of the cyclic utilization of SERS substrate. Comparing with Ag nanowires films in planar Raman substrates by the LB technique, the Raman enhancement of the capillary aligned films is bigger, however, SERS spectrum of Ag colloid nanoparticle films exhibit the worst performance (Figure 20B). The detection limit of the SERS spectra for adsorbed Rhodamine 6G on Ag nanowire substrates is as low as 5×10^{-9} M. The Ag nanowire films aligned inside of the capillary can be used as portable and reusable SERS substrates. After the substrates using R6G as the probe molecule immersed in the concentrated HCl acid liquid, no Raman signal was detected. Moreover, this aligned thin film can be used as a SERS sensor for detecting mixture pollutions. Figure 20D shows the SERS spectra of Ag nanowire thin film for probing 4-MBA, R6G and the mixture of 4-MBA and R6G. The capillary based SERS substrate can be served a versatile platform to detect mixture pollutions.

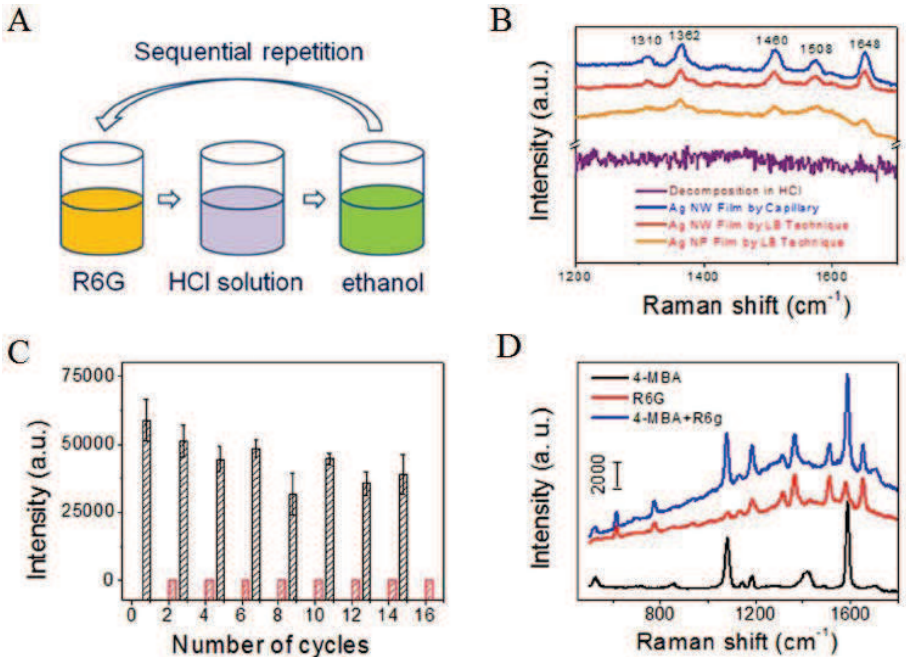

Figure 20. Unique SERS application of Ag nanowirs films inside of a capillary. (A) Scheme of the cylic utilization of SERS substrate. (B) SERS spectra of adsorbed R6G before and after the dispersion into the concentrated HCl, SERS spectra of Ag nanowire films by LB technique and SERS spectra of Ag nanoparticle films by LB technique. (C) Repeatability of the capillary SERS substrate about 8 cycles. (D) SERS spectra of adsorbed R6G, 4-MBA, and a mixture of R6G and 4-MBA.[38]

1.1.3.2 Fabrication of nanodevice

The high degree of orientation and tunable density of the nanowires is an important factor in lots of electronic devices and their potential applications. Haick et al.[48] aligned the SiNWs on a 300 nm thermal oxide coated heavily doped p-type silicon wafer. The aligned SiNWs were configured as back-gated field-effect transistors (FETs) by defining Ti/Au (40/110 nm) source (S) and drain (D) contacts with a channel length of 2 μm and a channel width ranging from 1 μm to 350 μm. The density of the connected Si NWs between the source and drain electrodes was similar for all channel widths. Figure 21A shows the drain current (I_{ds}) versus drain-source voltage (V_{ds}) curves of spray-coated Si NW arrays by using a sweeping voltage range from 0 to +2 V at various gate voltages (V_{gs}). We can see from the figure, the I_{ds} - V_{ds}

curves showed a typical accumulation mode of p-channel transistor behavior. Figure 21B showed the plot of I_{ds} *versus* V_{gs} at a constant V_{ds} = +2 V showed a small current when the V_{ds} was more positive than the threshold voltage. The I_{ds} increased linearly with increasing V_{gs} in the negative direction. The electrical features of the FETs reproducible from sample to sample. Randomly selected Si NW FETs showed well-constrained V_{th} and I_{on} behavior, with values of 4.26 ± 1.10 V and 0.66 ± 0.22 μA (Figure 21C, D).

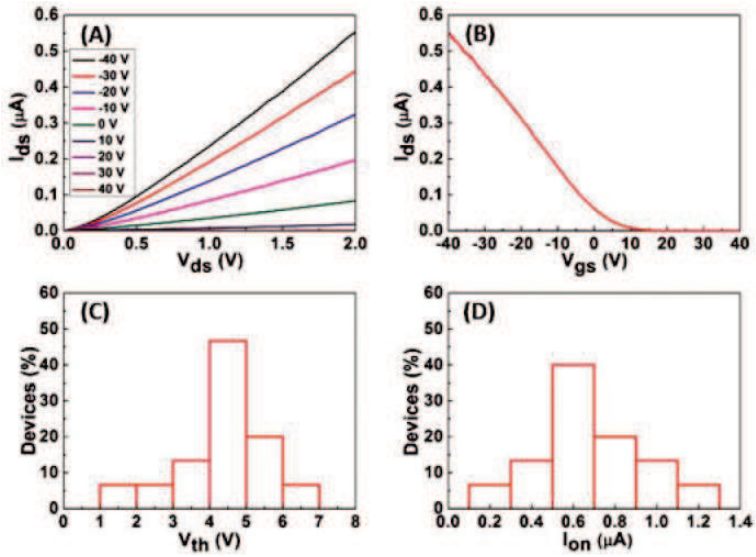

Figure 21. Devices based on Si NW arrays. (A) Family of source-drain current (I_{ds}) *versus* source-drain voltage (V_{ds}) plots at different gate voltages (V_{gs}). (B) Ids versus gate Vg recorded for a typical device plotted on linear scales at Vds = 2 V. (C) Histogram of the threshold voltage (V_{th}) determined from analysis of 15 random chosen devices. (C) Histogram of on-current (I_{on}) determined from analysis of 15 random chosen devices.[48]

Photoconductivity is an optical and electrical phenomenon which a material becomes more electrically conductive since the adsorption f radiation such as the visible light, ultraviolet light and infrared light. Yu and co-workers[17] prepared a type of photoconductive nanodevice composed of 20-layer parallel Te nanowire monolayer assemblies on Si/SiO_2 substrate by Langmuir-Blodgett technique. They investigated

the photoelectric properties of the Te nanowire nanodevice by measuring the current-voltage (I-V) curves in dark and under white light illumination of different light intensities (Figure 22A and B). The I-V curves exhibited linear behavior, and the electrical resistance of the Te nanowire films decreased when the light was turned on from the dark condition, the current of the divices increased significantly with the light intensity increasing (Figure 22B). It is high insulating in the dark (Figure 22A). Figure 22C showed a reversible switching of a Te nanowire device between high and low conductivity states when the lamp was turn on and off, after test cycles, the switch ratio remained 1.6, almost the same as the beginning. The device fabricated using aligned Te nanowires as building blocks shows a weak but detectable response to light, which suggested that they are candidates for optoelectronic switches, with the dark insulating state as "OFF" and the light exposed conducting state as "ON".

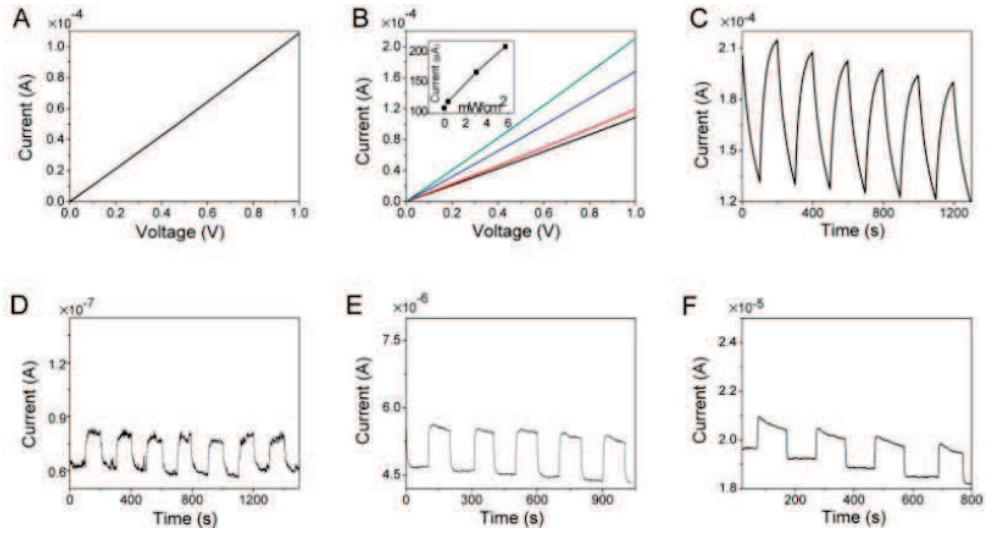

Figure 22. Photoelectric properties of the Te nanodevices. (A) I-V curves measured in the dark. (B) I-V curves measured under different light intensities. (C) Reversible switching of a 20-layer Te nanowires device between high and low conductivity. (D-F) Reversible switching photoconductivity properties of Te nanodevices which have monolayer, three layers and five layers, respectively.[17]

The well-aligned silver nanowires films can generated some novel optical properties since the electromagnetic fields that localized between the adjacent nanowires. This has great application in the field of ultrasensitive and molecular specific sensing. Yu et al.[26] investigated the dependence of the UV-vis spectra on the polarization angle of the incident light and found the existence of large EM fields in the films (Figure 23). The polarization angle of the incident light is the angle between the polarized electric field and the long axes of the nanowires, was recorded by rotating a half-wave plate in the laser path. When the polarization angle increased from 0° to 90°, the transmission intensity increased, which means the dependence of the extinction spectra is the dependence of the extinction of longitudinal plasmons within the monolayer. However, the film composed of the random oriented Ag nanowires, the transmission intensity showed no change as the polarized angle rotated from 0° to 90°. Thus, the great order of the film of the silver nanowires has the large electromagnetic fields.

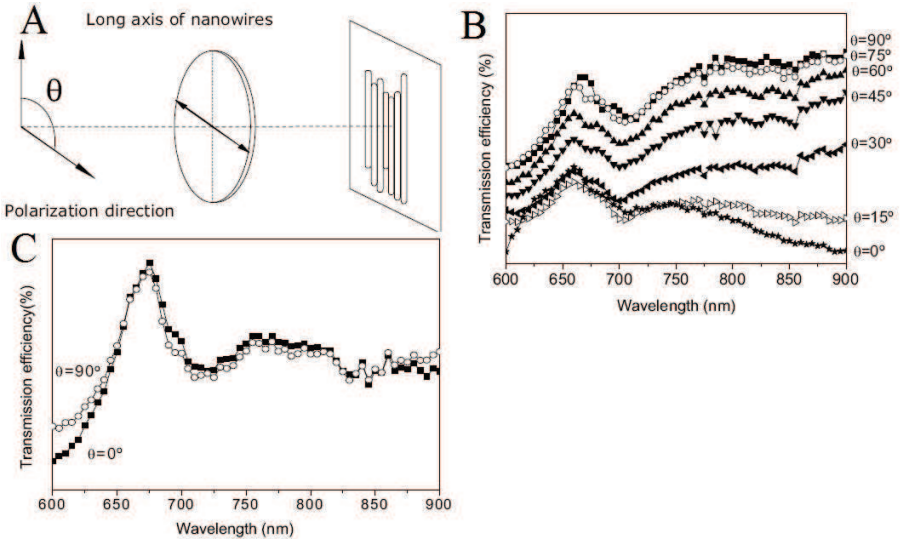

Figure 23. (A) Schematic illustration of the polarized angle θ, which is the angle between the polarization direction and the long axis of the nanowire. (B) UV-vis transmission spectra of the silver nanowire film measured with polarization angles in the range of 0-90°. (C) UV-vis transmission spectra of the film made from the randomly oriented Ag nanowire film. The spectra are obtained at polarization angle of 0° and 90°, respectively.[26]

1.1.3.3 Membranes for separation

Membranes composed of one-dimensional structures have been used to filtrate the nanometer-scale particles or viruses from solution. However, it is difficult to control the diameter of the 1D structure. The pore size of these fibrous membranes is not controllable and not suitable for the efficient separation and filtration of different sized nanoparticles. Recently, Yu and co-workers[52] report the preparation of new type of free-standing membrane made of carbonaceous nanofibers (CNF), which has very narrow pore size distribution and can filter out the nanoparticles effectively from a solution. The cut-off size of the membranes is tunable from a few tens to hundreds of nanometers by changing the diameters of the CNFs. The filtration behavior of these CNF was tested by filtering different size nanoparticles from solution. Three kinds of membranes consisting of different size CNFs (CNF-50, CNF-71 and CNF-98) were used to evaluate the performance. And five kinds of nanoparticles with different sizes, 5, 25, and 50 nm Au, 25 nm Ag, and 150 nm SiO_2 were chosen for the test. Almost all the 5 nm Au nanoparticles can pass through the membrane (Figure 24A), in contrast to the permeation of 5 nm Au particles, all the 25 nm Au particles can be filtered out from the solution (Figure 24B). For CNF-71 membrane, two different size Au nanoparticles were used to test the size selectivity. Au particles (25 nm) filtered out by CNF-50 membrane, but could freely pass through the CNF-71 membrane (Figure 24C). In contrast, the size of 60 nm Au nanoparticles were totally filtered out from solution by the CNF-71 membrane (Figure 24D). These results mean the CNF based membranes have excellent size-selective filtration properties.

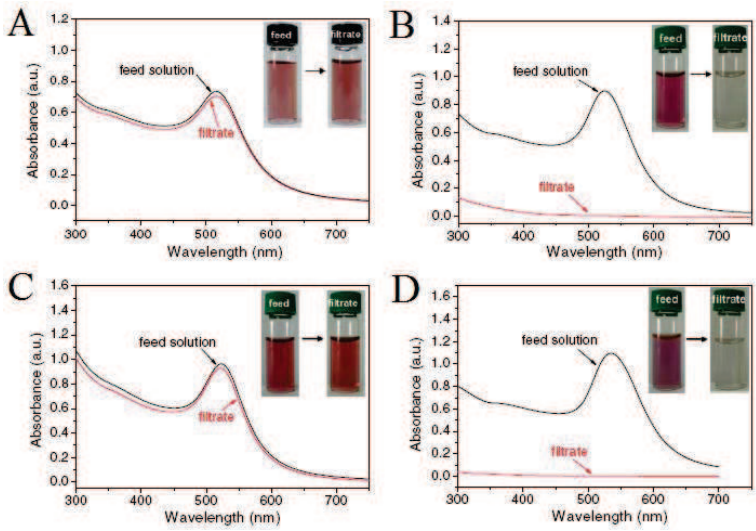

Figure 24. (A, B) Filtration of 5 nm and 25 nm Au nanoparticles using the CNF-50 membrane, respectively. (C, D) Filtration of 25 nm and 60 nm Au nanoparticles using the CNF-71 membrane, respectively.[52]

1.2 Layer-by-Layer (LbL) assembly

1.2.1 Principle of the LbL technique

Layer-by-Layer (LbL) deposition is an easy and versatile tool to fabricate the thin film. The first reports of this technique was done by Iler, who carried it out with microparticles on glass slides.[53] The technique was later revitalized by the discovery of its application to a wide range of polyelectrolytes by Prof Decher.[54] A simple description of the building of polyelectrolyte multilayers requires two opposite charge polyelectrolytes solution (a polycation ad a polyanion) and a substrate with charge on the surface. When a negetively charged substrate is dipped into a polycation solution, the polycation chains stick to the substrate due to the ionic interaction, which lead to a reverse surface charge. The substrate is then rinsed with pure water to remove the excess weakly attached chains and died. Followed by dipping into a polyanion solution causes a new adsorption of the negative layer, the surface charge of the substrate is reversed and negative charged. Then the film was washed with pure water again to remove the weakly adsorbed polyelectrolyte. One layer pair of polyeletrolyte complex thin film is obtained. The multilayer thin film can be constructed by alternate deposition of positively and negatively charged layers (Figure 25).

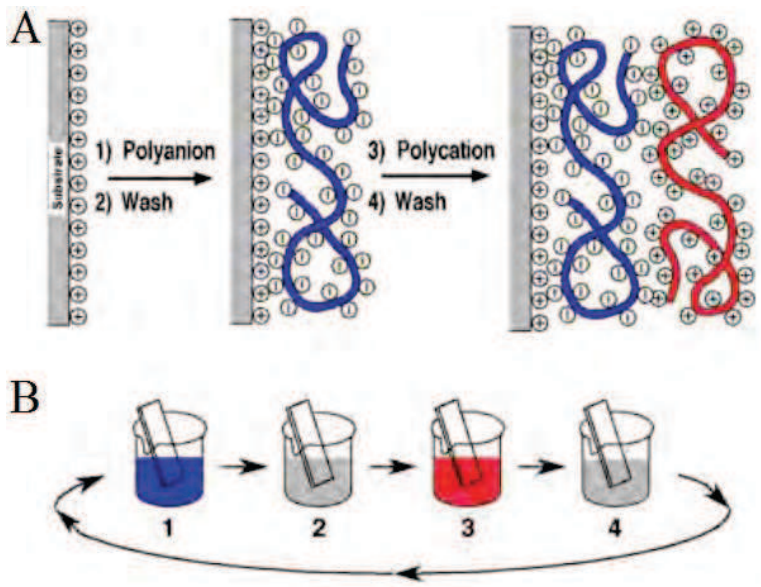

Figure 25. Principle of the Layer-by-Layer deposition technique. (A) Schematic illustration of the alternative adsorption of oppositely charged polyelectrolytes. (B) Illustration of the deposition process.[55]

Layer-by-Layer assembly technique allows the building of thin films with controlled structure and composition on almost any substrate. However, there is an issue with the time required for the film construction, it takes a few minutes to build a single layer by dipping, and this has to be multiplied by the deposited layer numbers. In order to shorten the depositing time, a much faster method for the Layer-by-Layer assembly was introduced by Schlenoff.[56] The same sequence is respected but the time for the deposition of a single layer reduces from around 10 minutes to around 5 seconds. This is because by dipping, the polyelectrolytes are absorbed on the charged surface due to the diffusion of the molecules from the solution to the surface, however, by spraying, the polymers are forced to go faster to adsorb on the surface. The thickness of the films prepared by spraying is thinner than the films prepared by dipping because there is a force to press the film during the film fabrication.

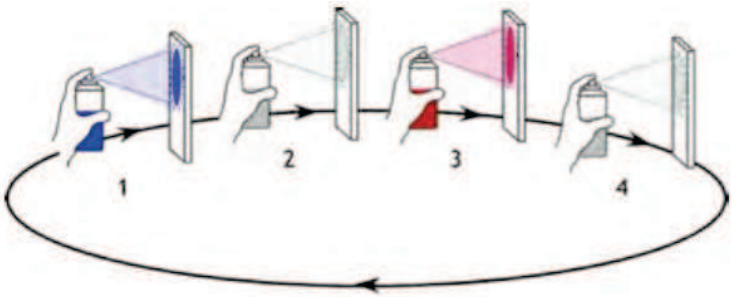

Figure 26. Fabrication of LbL film by spraying.[57]

Another fast approach for the deposition of a Layer-by-Layer assembled film is the Spin-assisted LbL deposition. Usually a small amount of material is placed on the center of the substrate, which is either spinning at low speed or not spinning. Then, the substrate is rotated at high speed in order to spread the coating material with the centrifugal force. Rotation is continued while the fluid spins off the edges of the substrate, till the desired thickness of the film is obtained. Usually, the applied solvent is volatile, the higher the angular speed of spinning, the thinner the film. Also, the material on the substrate experience a shear force due to the centrifugal force. When high aspect ratio nanostructrues is placed on the substrate, the nanostructures may be aligned due to the shear force in the radial direction.

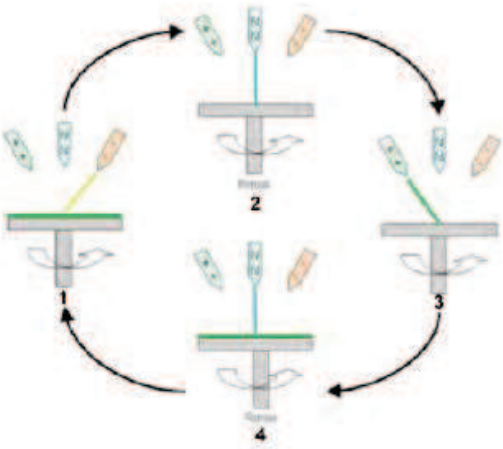

Figure 27. LbL assembly of polyelectrolytes films by spin-assisted coating.[58]

1.2.2 Polymers as building block

LbL assembly was initially used for polyelectrolyte/polyelectrolyte complex systems, now the LbL technique is almost applicable for any charged species. The positively charged polyelectrolytes are commonly used range from the conventional polyelectrolytes (poly(allylamine hydrochloride)) (PAH), poly(ethyleneimine) (PEI), polydiallyldimethylammonium chloride (PDADMAC)), and the common negative charged polyelectrolytes including poly(styrene sulfonate) (PSS), poly(acrylic acid) (PAA), poly(vinyl sulfate). Standard polymers functionalized with ionic groups can also be utilized. The use of electrostatic LbL assembly is not limited to charged polymers. Colloidal particles such as proteins and inorganic nanoparticles (silica, Au, TiO_2, magnetic nanoparticles) with charged surfaces are also commonly used as building blocks. The forces that promote fabrication of LbL films are also not restricted to ionic interactions. Assemblies based on hydrogen bonding [59], covalent attachment[60], biological recognition[61], host-guest interactions[62] and hydrophobic interactions[63] have also been investigated.

1.2.3 Control of the Layer-by-Layer buildup.

In any Layer-by-Layer assembly, the architecture of the thin film is determined by the deposition condition and the component. It is very necessary to characterize and monitor the buildup process. Ellipsometry is a very common way for this purpose since it is very easy to measure the thickness of the film with this technique. Usually, the growth of layer-by-layer assembled film is proportional to the number of deposition cycle, as the deposition cycle increased, the thickness of the film increased proportionally. This kind of build-up is called linear growth and the thickness of the multilayers film is determined by the number of deposition cycles. Figure 28 shows some example results measured with ellipsometry.

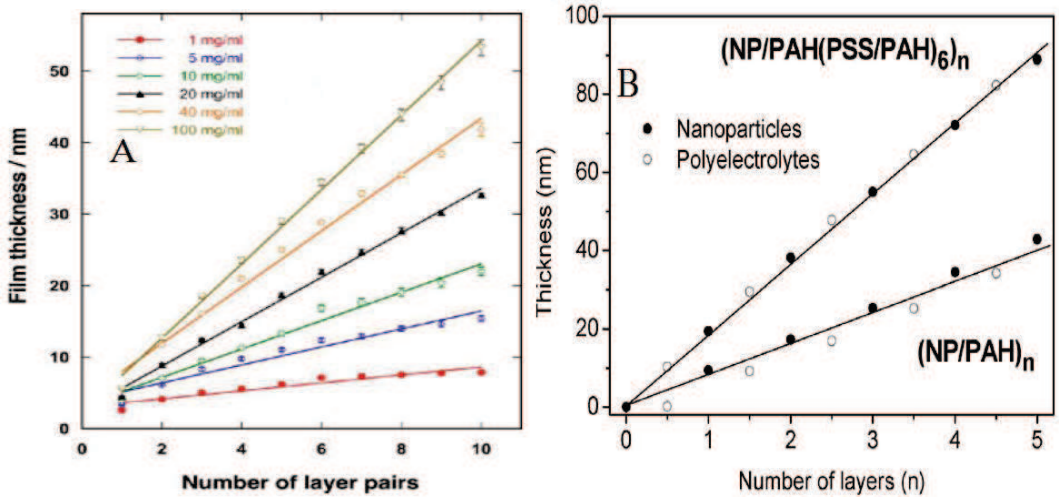

Figure 28. Ellipsometry monitoring the thickness of (PEI/CNER)n film (A)[64] and $(NP/PAH)_n$ film (B).[65]

Another very useful method is the UV-vis spectroscopy, it is suitable for a broad range of materials (Figure 29). Increment in absorbance per layer can be easily measured, which provides the information on the film growth in terms of the amount of material adsorbed on each layer as well as on the structure in term of the peak position. Usually, LbL film are built on glass and quartz slide for this kind of analysis. For LbL on particles, the solution with particles having LbL coating can be measured directly with the UV spectroscopy.

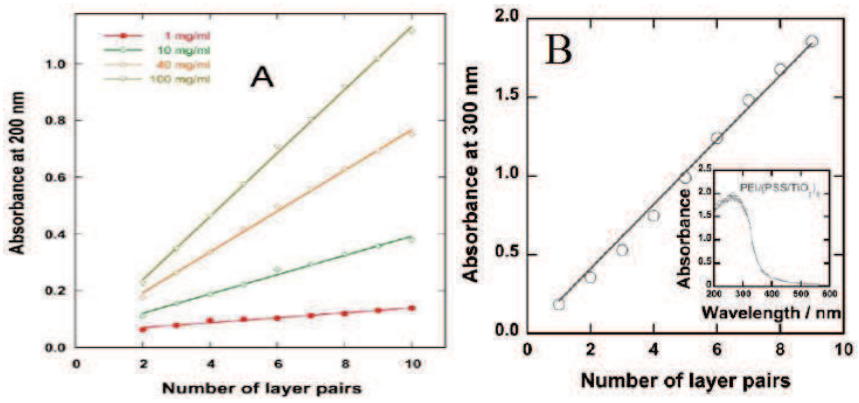

Figure 29. UV monitoring the film growth of (PEI/CNER)n film (A)[64] and $(PSS/TiO_2)_n$ film (B).[66]

For Layer-by-Layer assembly on the colloidal particles, the thickness of the shell on the core particle can be monitored by measuring the total size of the original particle and the shell by dynamic light scattering and by electron microscopy. For example, Decher et al.[67] monitored the LbL $(PSS/PAH)_n$ film built on the gold nanoparticles with Transmission Electron Microscope (TEM) (Figure 30).

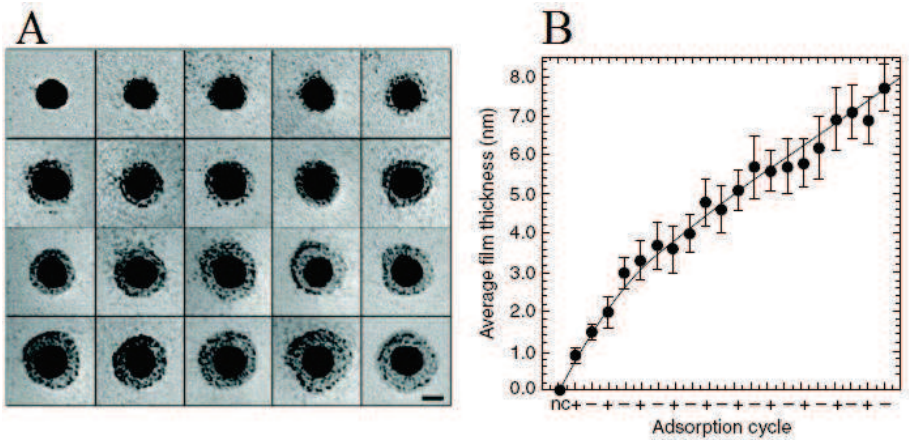

Figure 30. (A) TEM monitoring the film growth of (PSS/PAH)n on gold nanoparticles. (B) Average thickness of the shell calculated from the TEM.[67]

1.2.4 LbL assembly of various nanostructures

1.2.4.1 LbL assembly of nanoparticles

Nanoparticles with desired property can be assembled into the LbL films. In the process, first the polymers are coated on the substrate, and then the adsorption of the oppositely charged particles is used to build the multilayers. Virtually transparent films of TiO_2 were fabricated with PSS via layer-by-layer assembly.[66] These nanoscale films are fairly homogeneous and smooth over large areas and show different optical interference colors depending on film thickness. The photocatalytic performance of such films toward on-flow degradation of hydrogen sulfide under UV-A irradiation was investigated, which showed the catalytic efficiency of the films increased with increasing film thickness, also the nanoporous structure of the film allows for the permeation of gas (Figure 31).

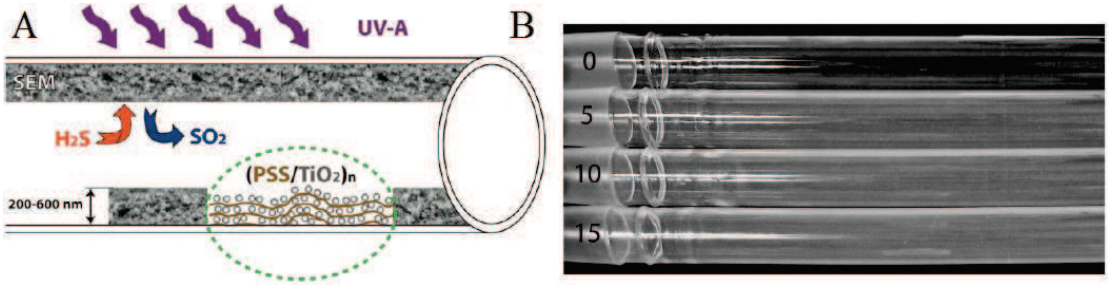

Figure 31. (A) Schematic showing the reactor with catalytically active coating. (B) Photographic image of tube reactors coated with PEI/$(PSS/TiO_2)_n$ films.[66]

Pichon and co-workers reported the ability to tune the magnetic properties of the iron oxide NP assemblies by controlling the formation of the LbL nanostructure (Figure 32). The magnetic properties of the film can be controlled by assembling of NP monolayers with very low roughness combined with the precise control of the interlayer distance. The iron oxide NPs interact preferentially in the plane of the NP layers through dipolar interactions, the resulting strong magnetic anisotropy along the NP layer induces their antiparallel coupling, which is highly dependent on the dipolar interactions occur between NPs of adjacent layers. The magnetic properties can be modulated by controlling of the distance between NP layers.

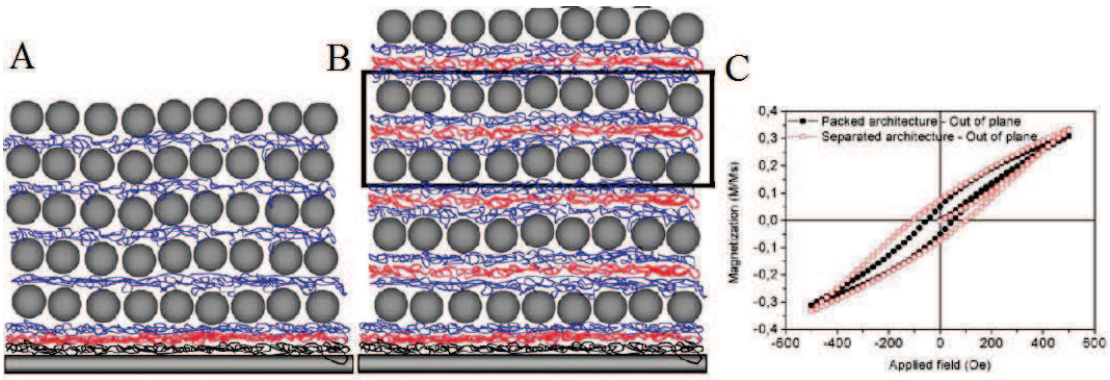

Figure 32. (A-B) Schematic representation of Packed architecture $(NP/PAH)_5$ and well-separated architecture $(NP/PAH(PSS/PAH)_6)_5$. (C) Out-of-plane magnetization curves of packed and separated architectures.[65]

Qureshi et al.[64] prepared the nanoprotective films of an oligomeric novolac epoxy resin with poly(ethyleneimne) using covalent LbL-assembly. The abrasion resistance of the cross-linked films was measured using a conventional rubbing machine and found to be greatly enhanced compared to the classic LbL-films that are mostly assembled by electrostatic interactions. This classic epoxy binder (CNER) was co-assembled with PEI to form thin protective layers on top of LbL-film composed of gold nanoparticles and PAH. The critical thickness of the protective LbL-films on top of the gold nanoparticle layer was determined to about 10 nm. At this thickness ,the entire film withstands at least 25 rubbing cycles with a reduction of the total thickness of about 2% or less (Figure 33).

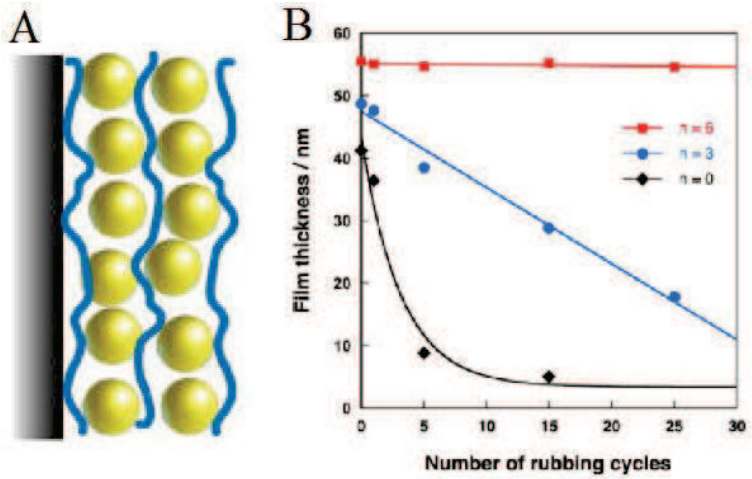

Figure 33. (A) Schematic representation of coating protective films on the AuNP-films. (B) Change of the film thickness for unprotected and nanoprotected AuNP-films as a function of different numbers of rubbing cycles.[64]

In another study, Au-NPs and the polyelectrolytes multilayer structures were fabricated using spin-assisted LbL method.[68] These films with a general formula $[Au/(PAH/PSS)_nPAH]_m$ possessed a well microstructure with uniform surface morphology. All films showed the strong extinction peak in the region of 510-550 nm, which is due to the plasmon resonance of the individual gold nanoparticles red-shifted

because of a local dielectric environment. For films with high density of gold nanoparticles within the layers, the second strong peak was consistently observed around 640 nm, which is the collective plasmon resonance from intralayer interparticle coupling. The observation of independent and concurrent individual, intralayer, and interlayer plasmon resonances can be critical for sensing applications, which involve monitoring of optomechanical properties of ultrathin optically active compliant membranes (Figure 34).

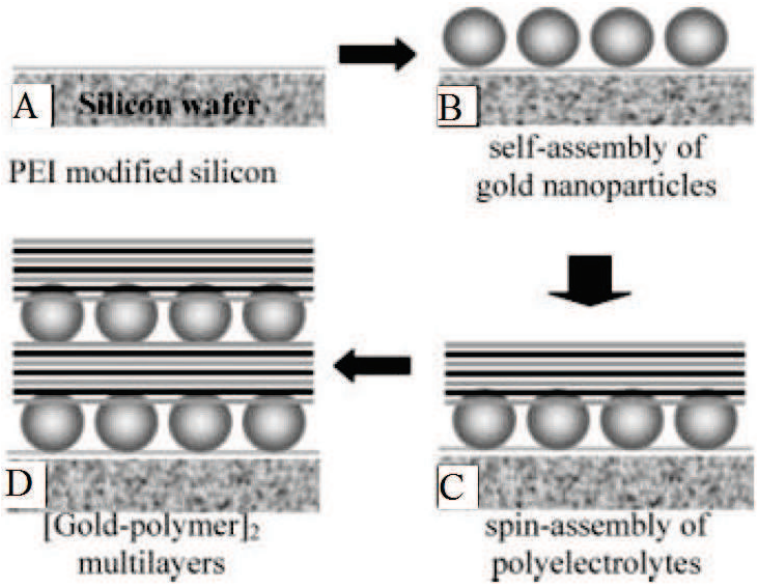

Figure 34. (A) PEI monolayer. (B) Au-NP monolayer deposited on PEI. (C) Au/(PAH/PSS)$_n$PAH fabricated by LbL. (D) [Au/(PAH/PSS)$_n$PAH]$_2$ multilayers.[68]

Rogach et al.[69] also LbL assembled the semiconductor NPs with the oppositely charged species. HgTe NPs and PDDA were assembled into thin films with controlled thickness. LbL films were prepared according to the standard procedure: (1) the substrate was dipped into the PDDA solution for 10 min, rinsed with water for 1 min. (2) the substrate was dipped into the dispersion of HgTe nanoscrystals for 20 min, then rinsed with water. Such a procedure resulted in a layer pair consisting of a polymer/nanocrystal composite. The cycle can be repeated for several times to obtain

a multilayer film of desirable thickness. The LbL assembled films displayed strong emission in the near-infrared range, peaking around 1600 nm and covering the entire telecommunications spectral region of interest. LbL films of nanoparticles can be considered as very inexpensive technology, enabling implementation of cost-effective high capacity optical networks.

Detsri and co-workers prepared composite thin films of silver nanoparticles and polyaniline for ammonia sensing[70]. The multilayer composite thin films were fabricated by alternate deposition of anionic and cationic polymers. Anionic polyelectrolytes was prepared by chemical reduction of silver ion using water soluble polyaniline as the stabilizing agent to form negatively charged silver nanoparticles/polyaniline composite. Silver nanoparticles with anionic water soluble polyaniline were then deposited into the thin film with cationic PDDA and characterized for their optical properties. These films were used as sensor for the ammonia detection, the changes in optical properties of the films were evaluated for various ammonia concentration. The color shifted strongly from orange-red to yellow when exposed to ammonia. These silver NP/polyaniline thin films displayed fast color change and could be used for ammonia sensing in industrial section (Figure 35).

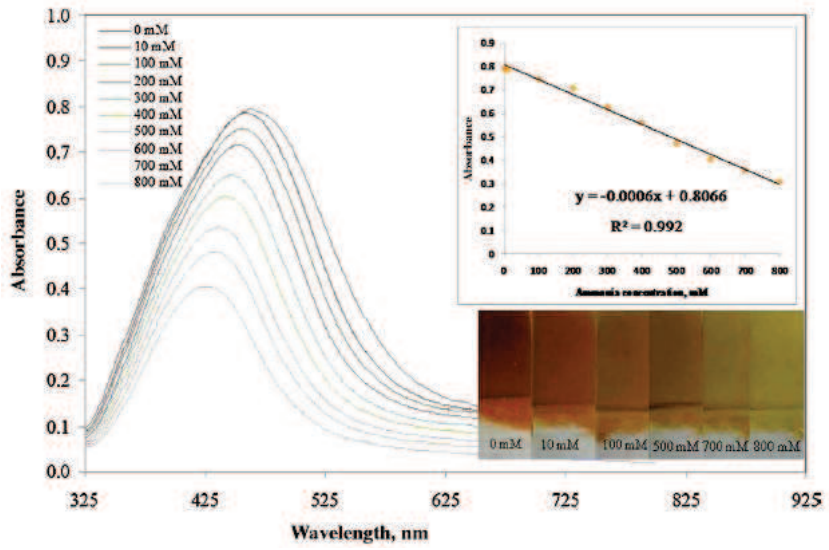

Figure 35. UV-vis spectrum of AgNP/polyaniline-CoPSS/PDDA multilayer films exposed to various concentration of ammonia.[70]

1.2.4.2 LbL assembly of nanoplates and nanosheets

LbL of NPs can also be extended to nanosheets, which are of great interest for their unique material properties. Notley et al.[71] Reported LbL assembly of positively charged PEI and anionic graphene sheets modified with layers of polyethylene oxide-polypropylene oxide-polyethylene oxide (PEO-PPO-PEI) surfactants. The buildup of the multilayer assembly through ionic interactions was strongly influenced by the solution conditions, such as pH, ionic strength, and ionic species. Thus, the thickness of the film could be tailored by numbers of layer pair and changing the solution conditions. Basic and acidic conditions were shown to favor the formation of multilayers based on the resulting packing of the PEI because the charge on the graphene sheets hardly caries over the pH range. The growth rate of the multilayers was also dependent on the graphene concentration. By considering the effect of each of these parameters, the deposition and formation of multilayers containing graphene can be easily optimized for a given application (Figure 36).

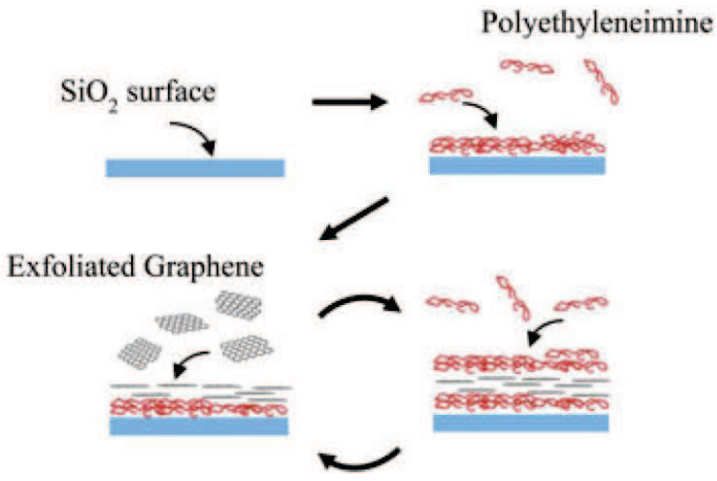

Figure 36. LbL assembly of graphene sheet with PEI.[71]

Liu and co-researchers Layer-by-Layer assembled the CdS quantum dots and graphene nanosheets into the multilayer hybrid films.[72] The stable aqueous dispersion of polymer-modified graphene nanosheets was prepared via in situ

reduction of exfoliated graphite oxide in the presence of PAH. The resulting water-soluble PAH-modified GNs and the tailor-made negatively charged CdS quantum dots were LbL assembled (Figure 37). This alternative GNs-CdS QDs multilayered films showed obviously enhanced photoelectrochemical and photocatalytic activities under visible light irradiation compared to pure CdS QDs and GNs films. This enhancement was mainly because of the judicious integration of CdS QDs with GNs in an alternating manner, which maximizes the 2D structural advantage of GNs in the composite films.

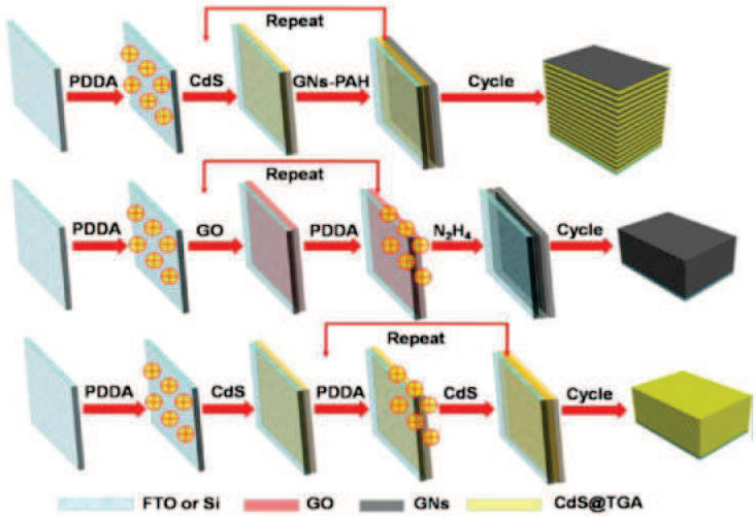

Figure 37. Schematic illustration for LbL assembly of GNs-CdS QDs, Pure GNs and pure CdS QDs multilayered films.[72]

Furthermore, multilayer thin films composed of gold nanoparticles (Au NPs) and titania nanosheets were constructed on glass or ITO substrate in an arbitrary layering order using the LbL technique.[73] Coverage of Au NPs with 1 to 3 layers of titania nanosheets can enhance the plasmonic resonance-based adsorption and photocurrents. Adsorption can be improved further by alternative stacking of Au NPs and titania nanosheets. Plasmon resonance of the multilayer can be red-shifted and enhanced by interlayer plasmon coupling via a single intervening nanosheet, however, the coupling can be suppressed by two or more layers of nanosheets. The polarity of

photoresponses can be controlled by changing the order of LbL assembly of Au NPs and titania nanosheets.

Lee et al. tried to improve membrane durability by Layer-by-Layer assembling of graphene oxide nanosheets on polyamide membrane.[74] The attractive features of graphene oxide nanosheets such as high hydrophilicity, chemical robustness and ultrafast water permeation was harnessed for a dual-action barrier coating layer that enhances resistance to both fouling and chlorine-induced degradation of polyamide thin-film composite membranes while keeping their separation performance. GO multilayers were coated on the PA-TFC membrane surfaces via LbL technique. It was found that the GO coating layer can increase the surface hydrophilicity and reduce the surface roughness, leading to obviously improved antifouling performance against a protein. The chemically inert nature of GO nanosheets enables the GO multilayer to act as a chlorine barrier for the underlying PA membrane, leading to a profound suppression of the membrane degradation in salt rejection upon chlorine exposure (Figure 38).

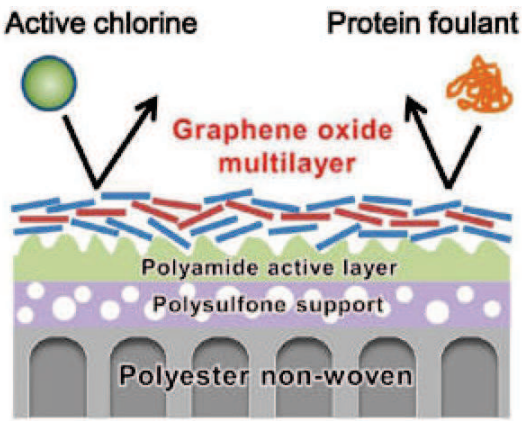

Figure 38. Schematic illustration of multilayered graphene oxide on a polyamide thin-film composite membrane surface for enhancing resistance to both fouling and chlorine-induced degradation.[74]

Hammond and co-workers developed a polymer-clay structure from a unique combination of LbL materials: PEI, Laponite clay and poly(ethylene oxide)[75]. This trilayer LbL structure is assembled using a combination of hydrogen bonding and

electrostatic interactions. The films were characterized using ellipsometry, profilometry, X-ray photon spectroscopy, AFM, SEM and electrochemical impedance spectroscopy (EIS). The results demonstrated a layered, anisotropic structure, which resulted in in-plane ion transport 100 times faster than cross-plane at 0% relative humidity. Podsiadlo et al[76] prepared layered ultrastrong polymer nanocomposites using poly(vinyl alcohol) (PVA) and montmorillonite (MTM) clay. SEM showed the dense coverage of the nanoplatelets and strictly planar orientation (Figure 39). Evaluation of mechanical properties yielded remarkable results even without glutaraldehyde (GA) cross-linking. The nanocomposited displayed four times higher strength and nearly one order of magnitude higher Young's modulus when compared with pure PVA polymer. GA cross-linking increased the strength, stiffness, and brittleness of both pure PVA and the PVA/MTM composite. A high level of ordering of the nanoscale building blocks, combined with dense covalent and hydrogen bonding and stiffening of the polymer chains, leads to highly effective load transfer between nanosheets and the polymer.

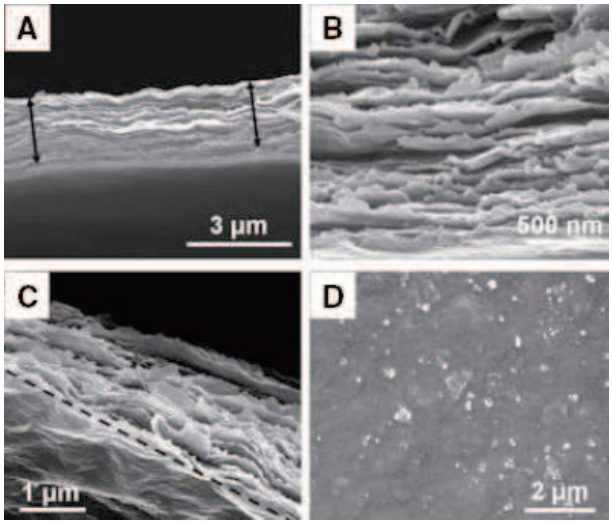

Figure 39. SEM of PVA/MTM nanocomposite: (A) Cross-section of the film. (B) Close-up of the cross-section. (C) Top-down view of a fracture edge of the composite after tensile testing. (D) Top-down view of the composites surface.[76]

Bi_2WO_6 nanoplates were also incoporated into the LbL films by Shi and co-workers (Figure 40).[77] These multilayer films show higher visible-light photoactivity ($\lambda > 420$ nm) than that of Bi_2WO_6 nanoplate powders and P25 TiO_2 films. Photocatalytic activities of the films were evaluated by decomposing rhodamine B (RhB) under UV and visible-light irradiation. Thickness and photoactivity of the film can be modified easily by changing the deposition cycles. Bi_2WO_6 nanoplate films showed the spectral selectivity of the photocatalytic degradation of RhB. Under the wavelength greater than 300 nm, the RhB molecules tend to be transformed to rhodamine over Bi_2WO_6 films selectively. However, under shorter wavelength ($\lambda = 254$ nm) light irradiation, the RhB molecules can be photodegraded completely. Generally, the Bi_2WO_6 films have both the potential application in selective oxidation and photosynthesis, and in photodegradation of dyes by the different wavelength light irradiation.

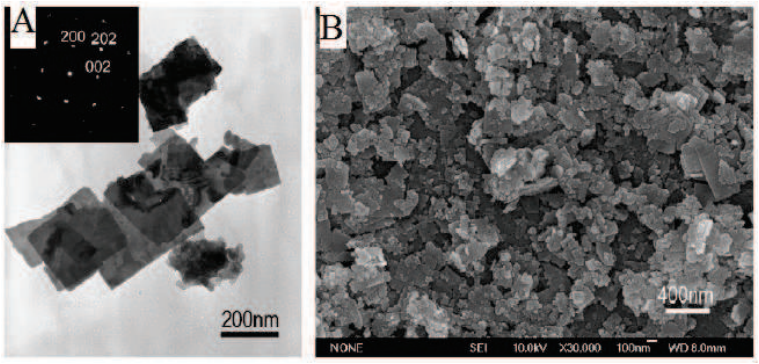

Figure 40. (A) TEM image of Bi_2WO_6 nanoplates and the electron diffraction pattern (inset). (B) FE-SEM image of Bi_2WO_6 film with eight deposition layers.[77]

1.2.4.3 LbL assembly of one-dimensional nanowires

LbL assembly of one-dimensional NWs is a new area of research. One-dimensional materials play a very important role in fabricating devices of the next generation. The LbL assembly method was extended to NWs by alternative adsorption of polymers and NWs. Kotov and co-workers[78] reported the LbL assembled films of natural

cellulose nanowires, which obtained from a marine animal tunicate display surprisingly high uniformity and aspect ratio comparable with synthetic NWs. Their LbL assembled films show strong antireflection (AR) properties have an origin in a novel highly porous architecture reminiscent of a "flattened matchsticks pile", with film-thickness-dependent porosity and optical properties created by randomly oriented and overlapping NWs. At an optimum number of LbL deposition cycles, light transmittance reaches nearly 100% ($\lambda \approx 400$ nm) when deposited on a microscope glass slide. This first example of LbL layers of cellulose NWs can be seen as an exemplary structure for any rigid axial nanocolloids, for which, given the refractive index match, AR properties are expected to be a common property. Gunawidjaja et al [79] fabricated the freestanding layer-by-layer (LbL) films encapsulating controlled volume fractions of silver nanowires. The AgNWs are sandwiched between poly(allylamine hydrochloride)/poly(styrene sulfonate) (PAH/PSS) films resulting nanocomposite films with a formula of $(PAH/PSS)_{10}PAH/AgNW/(PAH/PSS)_{10}PAH$ (Figure 41). The Young's modulus, roughness, ultimate strain are evaluated for supported and freestanding structures. Since the diameter of the nanowires (73 nm) is larger than the thickness of the LbL films, a peculiar morphology is observed with the silver nanowires protruding from the planar LbL films. Nanowire-containing LbL films possess the ability to sustain significant elastic deformations with the ultimate strain reaching 1.8%. The Young's modulus increases with increasing nanowire content, reaching about 6 GPa for the highest volume fraction, due to the filler reinforcement effect commonly observed in composite materials. The ultimate strengths of these composites range from 60-80 MPa, which is comparable to LbL films reinforced with carbon nanotubes. These robust freestanding arrays of silver nanowires with peculiar mechanical, optical, and conducting properties combined with excellent micromechanical stability could serve as active elements in microscopic pressure and photothermal sensors.

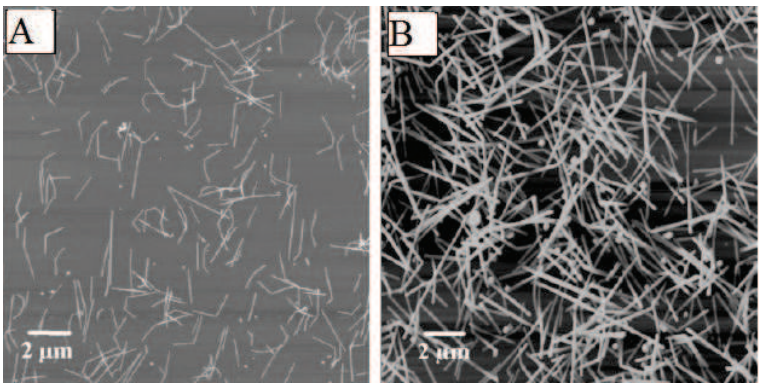

Figure 41. AFM images of silver nanowires assembled on ten PAH/PSS layer pairs.[79]

Liz-Marzan and co-workers reported the LbL films using the standard polyelectrolytes and Au wires.[80] The influence of average interparticle distance on the optical response of gold nanorods was studied through the systematic construction and characterization of monolayer and multilayers on glass substrates. The control of nanorod density in monolayers was achieved by varying deposition time, and spacing in multilayer films was varied by increasing number of polyelctrolyte layer pairs (Figure 42). Finally, well-defined interparticle distance were imparted through homogeneous coating of the nanorods with silica shells. In all cases, plasmon coupling (leading to extensive red-shift and broading of the longitudinal surface plasmon band) could be efficiently screened by keeping the particles separated at distances longer than the nanorod short axis.

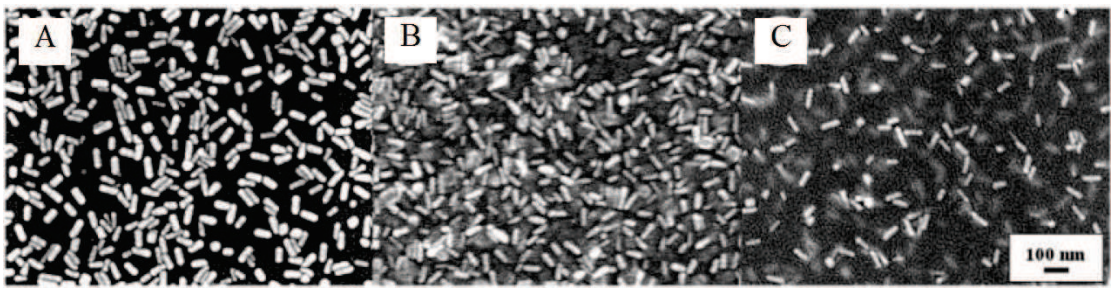

Figure 42. TEM images of LbL multilayer Au nanorod films with four nanorod layers separated by: a single PDDA layer (A); PDDA/PSS layer pair (B); and $(PDDA/PSS)_2$ multilayers (C).[80]

Layer-by-Layer assembly of NW was also performed by transition of CdTe NPs to Te NWs in the presence of EDTA (Figure 43).[81] Te NWs with a surface charge potential of ~ - 50 mV, exhibited a uniform diameter with lengths ranging from 100 to 800 nm. The solid, thin films of Te NWs on glass slide were prepared by using a standard LbL approach by dipping the glass slide alternatively into a positively charged polyelectrolytes (PDDA) and negatively charged Te NW solution. To characterize the conductive and photoconducting properties of the LbL assemblies made from Te NWs, PDDA/NW was prepared and electrical contacts were made by attaching silver wires to the surface of the Te films with colloidal silver paste as the conductive glue. The electrical resistance of the Te NW films was measured in the dark and under illumination with low-power sources. The "light-on-light-off" cycle was demonstrated to be very stable under ambient conditions for more than 100 repetitions, revealing no sign of photodegradation. The photocurrent rise-and-fall kinetics were found to be relatively long. The photocurrent measurement of the thin films demonstrated that Te thin films can be reversibly switched between the lower- and higher- conductivity states after exposure to the external light sources. The photoconducting NWs could serve as light detectors and switching devices for optoelectric applications, in which the binary states can be addressed optically.

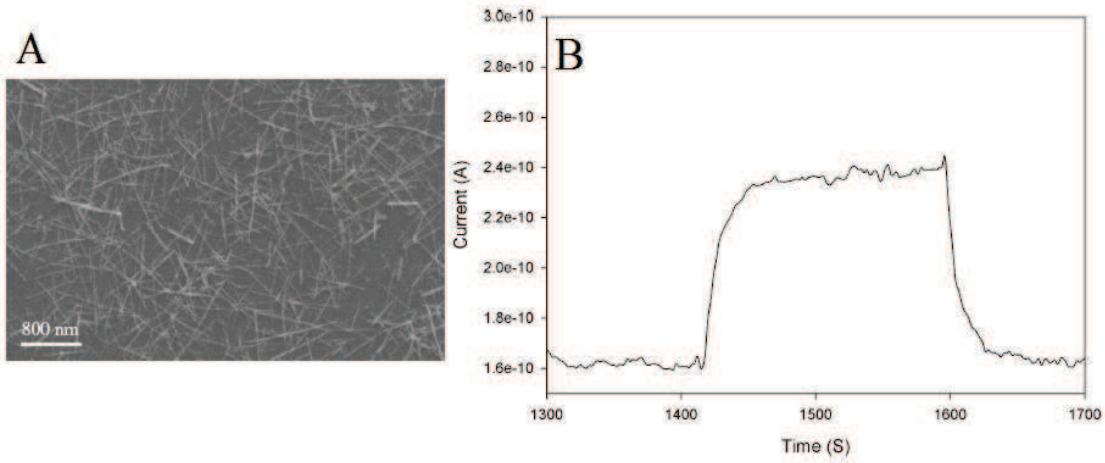

Figure 43. (A) SEM image of $(PDDA/NW)_2$. (B) Photoresponse of the Te films for repetitive switching between "on" and "off" states.[81]

1.3 Chiral plasmonic nanostructures

An object or a system is chiral if it is distinguishable from its mirror image, which can not be superposed onto it. Oppositely, a mirror image of an achiral object, such as a sphere, can not distinguished from the object. A chiral object and its mirror image are called enantiomers. Human hands are the best example of chirality. The left hand is a non-superimposable mirror image of the right hand, no mater how the two hands are placed, it is impossible for all the major features of both hands to coincide across all axes.

Molecular chirality is of interest in chemistry and biology. It was Louis Pasteur, who investigated the recemization of tartaric acid, found the connection between chirality and optical activity.[82] Chirality is not limited to molecular systems, but may appear in any object. In recent decades, wide attention have been paid to the chirality in inorganic nanostructures for the following reasons: 1. In some cases, nanostructures might have much stronger optical activity than the molecular systems, such optical activity could result in interesting optical effects and devices. 2. After precisely controlling in the synthesis of nanostructures, such as, nanoparticles, cubes, rods, wires, fabricating of chiral nanostructures is of course one of the next challenges.

In the field of chiral plasmon nanomaterials, both fundamental studies and applied

research depend on their various and reliable preparation methods. Normally, chiral plasmonic systems may appear in the following cases: (1) Nanostructure with a chiral shape, and there is enantiomeric excess in the ensemble of nanostructures, then optical activity is expected. (2) The achiral nanoparticle are arranged in a chiral configuration and electronic coupling between the nanoparticle occurs, CD should occur because of the electronic excitation of the NPs. (3) Macroscopic mixtures of achiral nanoparticles with chiral inorganic crystals. (4) When an achiral NP is interacting with chiral molecules, the induced CD at the electronic states of the particle may occur (Figure 44).

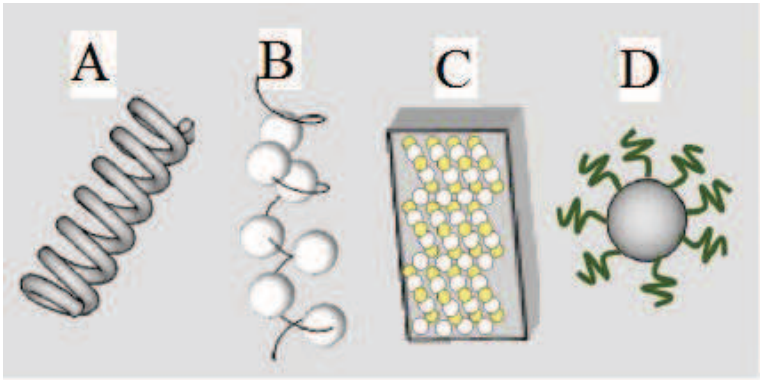

Figure 44. Various possibilities of obtaining CD at the electronic excitation of nanostructure. (A) Chiral shape. (B) Chiral arrangement of interacting achiral NPs. (C) Intrinsically chiral crystal. (D) Achiral nanoparticle interacting with chiral molecules.[82]

1.3.1 Nanostructures with chiral shapes

So far, some progress has been made in strategies to synthesize helical and chiral nanostructures, but most helical inorganic nanostructures were obtained with random handedness.[83] Only, very recently, some groups have tried the enantioselective synthesis of helical structure. For example, Che et al.[84] reported the surfactant-templated synthesis of ordeered chiral mesoporous silica, together with a general approach for the structural analysis of chiral mesoporous crystals by electron

microscopy. The meterial has a twisted hexagonal rod lide morphology, with diameter 130-180 nm and length 1-6 μm. TEM confirm the presence of hexagonally ordered chiral channeles with a diameter of 2.2 nm winding around the central axis of the rods. This result could lead to new uses for mesoporous silica and other pore chiral pore materials in catalysis and separation media, where both shape selectivity and enantioselectivity can be applied to the manufacturing of enantiomerically pure chemicals and pharmaceuticals (Figure 45). Recently, the same group synthesized chiral TiO_2 fibres via transcription of the helical structure of amino acid-derived amphiphile fibres through coordination bonding interactions between the organics and the TiO_2 source. After calcinatin, the as-prepared amorphous TiO_2 double-helical fibres with a pitch length of ~ 100 nm were transferred to double-helical crystalline fibres with anatase nanocrystals in an epitaxial helical relation ship. Both the amorphous and anatase crystalline helical TiO_2 fibres exhibited optical response to circularly polarized light at the absorption edge around ~ 350 nm.[85]

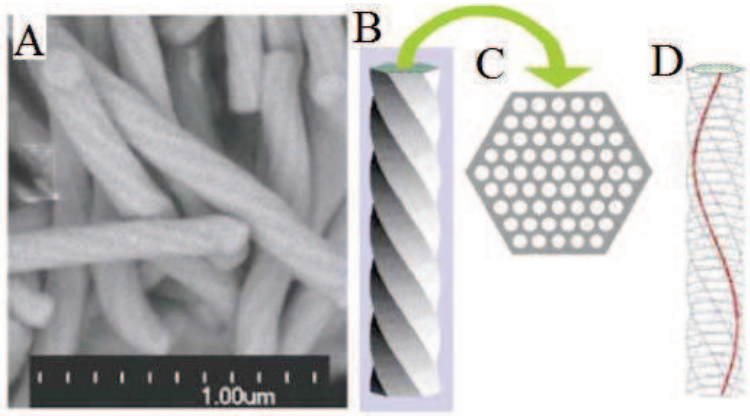

Figure 45. SEM image and schematic drawing of a structural model of chiral mesoporous silica. (A) SEM image, showing the microscopic features of the sample. (B) Schematic drawing of a structural model of the chiral mesoporous material for TEM simulation. (C) Cross-section. (D) One of the chiral channels in the material.[84]

Efforts have also been made impart chirality at a larger scale. MacLachlan and co-workers[86] developed a free-standing mesoporous silica films with long-range

chiral nematic ordering using a template-based method. The chiral nematic organization and the high surface area of nanocrystalline cellulose is accurately replicated in the inorganic solid. The helical structure of the films results in chiral reflectance that can be tuned across the entire visible spectrum and into the near-infrared (Figure 46). These materials can be used as templates to synthesize a variety of new materials with chiral nematic structures. Also, the mesoporous silica materials are imprints of chiral cellulose particles at multiple levels, and cellulose is a leading materials for chiral separation, these materials could be a candidate for separating enantiomers.

A more straightforward method for fabricating chiral metallic and inorganic shapes is the top-down approach. There are three types of plasmonic structures can be prepared by this top-down approach: (1) planar chiral structures,[87] those structures are typically intrinsically chiral because of the different interfaces on the two sides of the metal film pattern, glass-metal on one side and air-metal on the other side. (2) three-dimensional structures.[88] (3) Achiral plasmonic arrays that show chiroptical activity when tilted with respect to the light beam.[89]

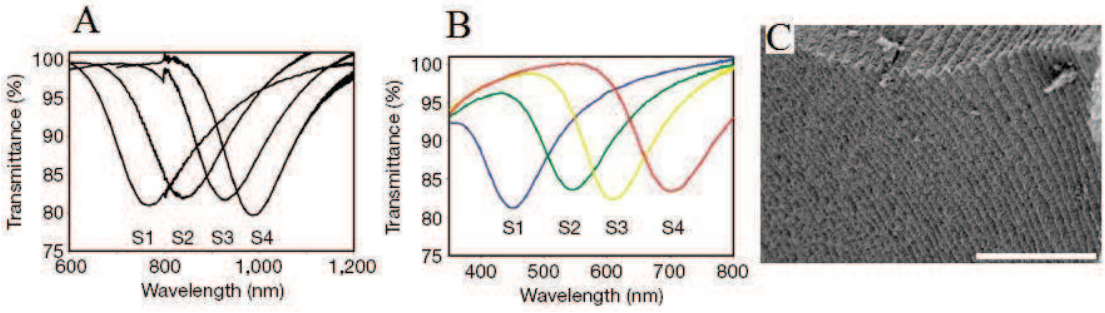

Figure 46. (A) Transmission spectra of four composite films with reflectance peaks in the near-infrared part of the spectrum. (B) Transmission spectra of the mesoporous silica films obtained from the calcination of composite films. The reflectance peaks were all blueshifted by about 300 nm. (C) Side view of a cracked film shows the stacked layers that result from the helical pitch of the chiral nematic phase.[86]

1.3.2 Chiral arrangement of interacting achiral NPs

1.3.2.1 Prepared by template induced assembly

When achiral NPs are arranged in a chiral configurations with strong inter-particle interaction, the nanostructure may show chiroptical activity. The most important part for the assembly of achiral NPs is the shape of the basic building blocks. The earliest approach for fabricating chiral nanostructures is to use existing organic structures as a template. Inorganic nanomaterials can be adsorbed or depostied on top of the template. This kind of template can be easily removed by calcination because the inorganic materials are usually more resistant to the high temperature. Normally, to form chiral plasmonic nanostructures, the inorganic materials must meet two requirements: (1) must have an affinity to the template. (2) must not cause significant disruption of the template. Also, in this approach, the nanomaterials should be prepared and purified before they are put together with the template. One challenge is the affinity between the template and the nanomaterials, which should be strong enough preventing the resulting complex separating from each other because of the shear force in the solution.

The most common used template is DNA, which has four basic pairs, so four different nanoparticles can be placed at its four corners, forming a chiral structure. The Liedl group reported the DNA scaffold enables the high-yield production of plasmonic structures that contain nanoparticles arranged in nanometre-scale helices (Figure 47).[90] An excess of AuNPs with multiple linker strands were employed to ensure linkage to the scaffold and thus, eliminate the purification step. In agreement of the computer simulation, the chiral structures in solution exhibited defined circular dichroism and optical rotatory dispersion effects at visible wavelengths that originate from the collective plasmon-plasmon interactions of the nanoparticles positioned with an accuracy better than two nanometers. The optical response of the nanoparticle assemblies is rationally designed and tunable in handedness, color and intensity-in accordance with the theoretical simulations.

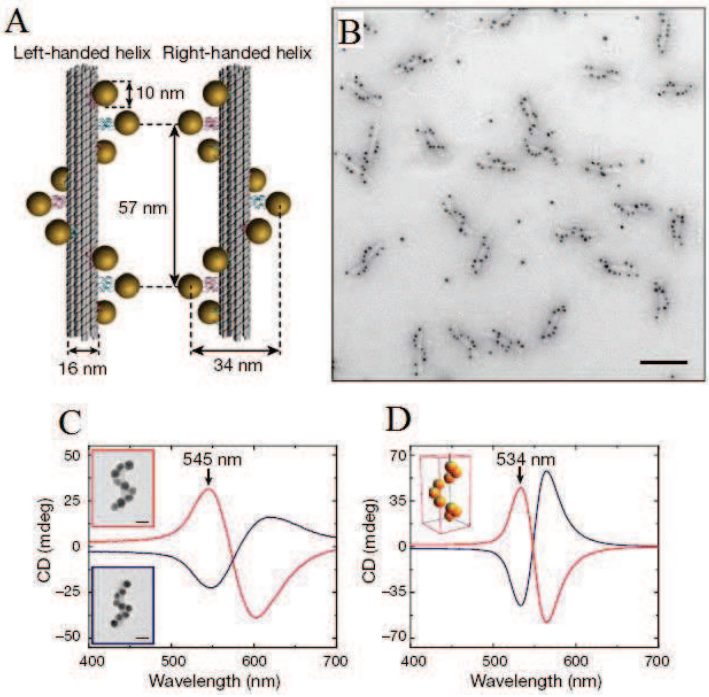

Figure 47. (A) Left- and right-handed nanohelices are formed by nine gold nanoparticles that are attached to the surface of DNA origami. (B) TEM image o assembled left-handed gold nanohelices. (scale bar: 100 nm) (C-D) Strongly interacting helical gold NPs held by DNA Origami and exhibiting strong chiroptical activity together with computer simulation.[90]

Recently, Wang and co-researchers successfully constructed anisotropic gold nanorod (NR) helical superstructures with tailored chirality in a programmable manner.[91] By designing the "X" shape of the arrangement of DNA capturing strands on both sides of a two-dimensional DNA template, AuNRs functionalized with the complementary DNA sequences were positioned on the origami intercalated between neighboring AuNRs. Left-handed (LH) and right-handed (RH) AuNR helices were conveniently achieved by simply tuning the mirrored "X" patterns of capturing strands on the origami. The inter-rod distance was 14 nm and twisted angle was 45 degree, thus a full helix contains 9 AuNRs with length up to about 220 nm. By changing the AuNR/origami molar ratio in the assembly system, the average number of AuNR in the helices was tuned from 2 to 4 and 9. The CD results (Figure 48) evidently demonstrated the dependence of optical activities of the AuNR helices on the 3D

configuration and the number of AuNR in the helices. The concentration of the assemblies that principally have 9 AuNRs is much lower than that of the two other smaller AuNR helices containing 4 and 2 AuNRs, but the CD signal of the 9 AuNR helices is higher, which demonstrated the chiroptical activities of AuNR helices can be greatly intensified by increasing the number of AuNR in the superstructures.

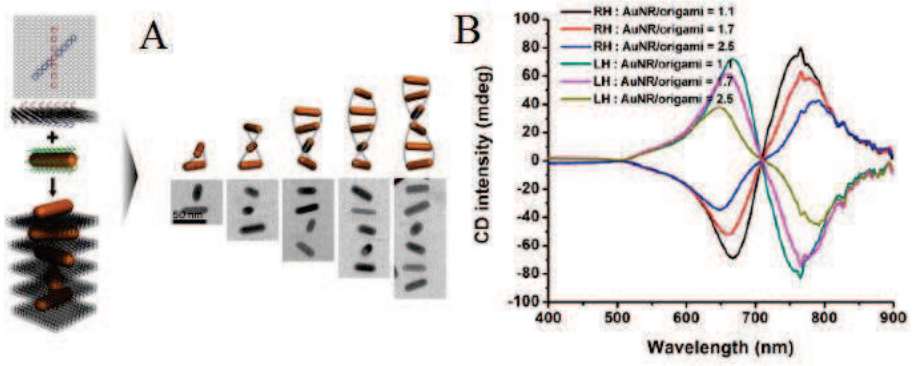

Figure 48. (A) Schematic illustration of the self-assembly of RH-AuNR helices. (B) The CD spectra of RH- and LH-AuNR helices containing varying numbers of AuNRs. With the AuNR/origami ratio increasing from 1.1 to 1.7 and 2.5, the number of AuNRs in the resulting structures decreased from 9 to 4 and 2, respectively.[91]

The template for the nanorod assembly can also extend to polymer fibers. Liz-Marzan et al.[92] reported a novel class of metamaterial composing of gold nanorods (NRs) organized in three-dimensional chiral structures and yielding a record circular dichroism anisotropy factor for metal nanoparticles across visible and near-infrared region. The fabrication involves the self-assembly of gold nanorods on a fiber backbone with chiral morphology. To prepare the nanocomposites, a solution of NRs was added to the fiber dispersion (right-handed (P) or left-handed (M)), leading to a assembly of nanoparticles onto the fiber surface (Figure 49A). Nanorods are preferentially aligned along the longitudinal direction of the fibers through non-covalent interactions, both enantiomeric nanocomposites show mirror-image CD response (Figure 49B).

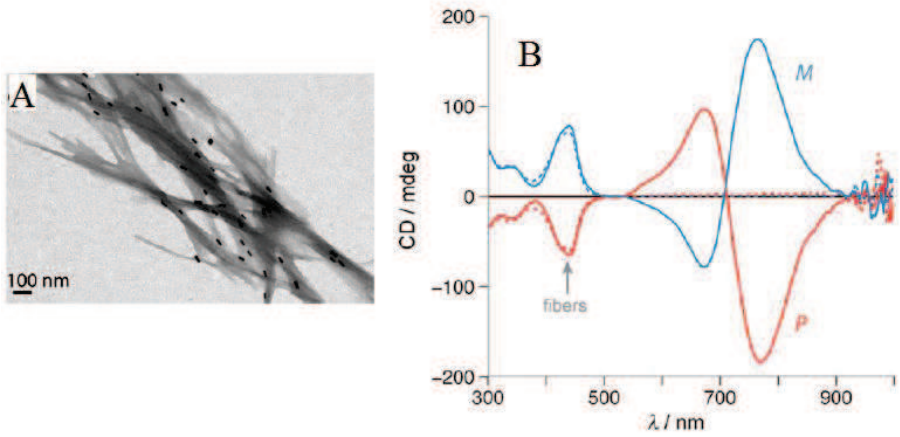

Figure 49. (A) TEM image of the M nanocomposite showing twisted fibers with adsorbed nanorods. (B) CD spectra of P and M nanocomposites.[92]

1.3.2.2 Prepared by co-assembly

Co-assembly is also a straightforward, cost-efficient method to fabricate the plasmonic materials. Recently, Kumacheva and co-workers reported the corporation of guest gold NRs into a macroscopic cholesteric solid film formed by cellulose nanocrystals (CNCs).[93] This method is based on the co-assembly of CNCs and gold NRs. The opposite electrostatic charges of the anionic CNCs and cationic NRs favor attraction between these species in the mixed suspension and lead to the chiral assembly of the NRs in the host cholesteric films (Figure 50). The interesting properties of the films originate from the interaction of the photonic properties of the CNC matrix and plasmonic properties of the gold NRs. These composite film show novel optical properties. With the concentration of the NRs increased, the CD peak exhibited blue-shift. The induced plasmonic chiroptical activity of the composite films can also be tuned. The composite films were prepared by changing the NRs with different aspect ratios. With the NR aspect ratio increasing from 2.4 to 3.0 and then to 4.0, the plasmonic bands red-shifted. These interesting properties are beneficial for fundamental studies of collective plasmonic chiroptical activity properties and their potential applications.

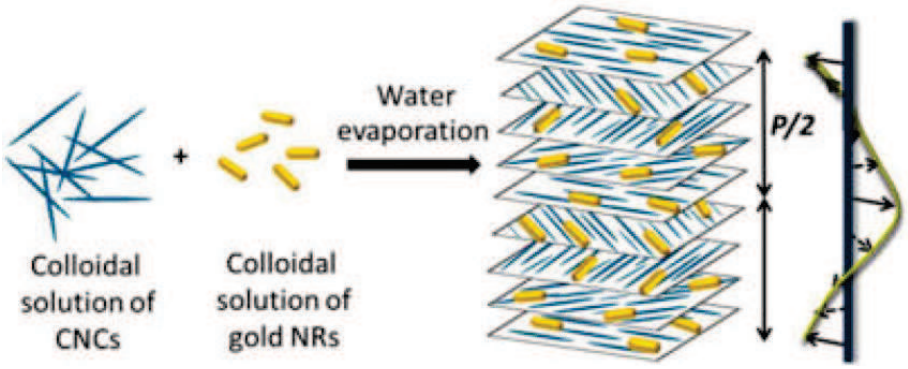

Figure 50. Schematic of the preparation of the composite plasmonic film by mixing aqueous suspension of CNCs and gold NRs.[93]

1.3.3 Nanomaterials made of intrinsically chiral inorganic crystals

An recent example for enantioelective synthesis of inorganic nanocrystals of an intrinsically chiral materials was given by Markovich and coworkers.[94] The main idea was to use colloidal chemistry in an environment of a relatively large concentration of chiral molecules that could bind strongly to the surface of the forming crystals. The synthesis makes use of chiral surfactant molecules (penicillamine), which direct the formation of these chiral nanocrystals from the achiral phase of β-HgS. Hg^{2+} and S^{2-} were precipitated in the presence of chiral molecules with thiolate groups, which can bind to Hg to form α phase crystal. The α-HgS crystal exhibited very strong CD responses at their excited absorption threshold, proving that the formation of enantiomeric materials. Figure 51 (A,B) shows the scheme of the chiral crystal structure and the high resolution TEM image of the nanocrystals. The opposite enantiomers of nanocrystals can be formed by using of opposite enantiomers of the capping chiral molecule penicillamine, no obvious change in absorption was observed between the two samples. A mixture of both enantiomers resulted in a CD signal with an amplitude proportional to the molar excess of one enantiomer (Figure 51C), which indicates that both enantiomorphic nanocrystals were formed statistically, whereby one enantiomer was formed in excess with respect to the other in proportion to the amounts of the two ligands present. This truly chiral nanocrystals with tailored size and shape is expected to be useful for many

applications, such as enantioselective cayalysis and sensing.

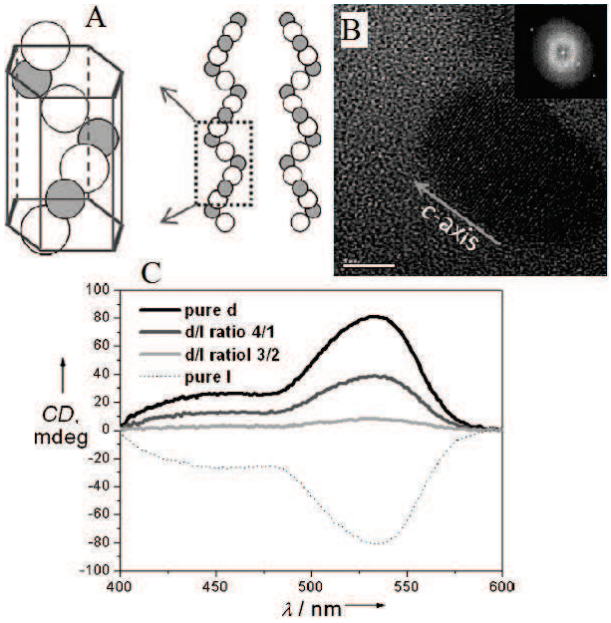

Figure 51. (A) Schematic illustration of the opposite spirals of atoms with a fraction of one spiral reconstructed inside the frame of the hexagonal unit. (B) High-resolution TEM image of individual nanocrystals. (C) CD spectra of samples obtained at different molar ratios of L- and D-penicillamine with the same total concentration of Hg and penicillamine.[94]

1.3.4 Achiral nanoparticles interacting with chiral molecules

The earliest observation of induced CD of achiral molecules at the absorption lines by chiral molecules was made by Bosnich.[95] Very recently, it was found that chiral molecules interacting with achiral nanoparticles can induced CD at the surface plasmon resonance. Maoz et al.[96] reported a simple system based on gold island films deposited on glass was used in conjugation with a natural chiral molecules such as riboflavin or polylysine without direct bonding to each other. It was found that the randomly oriented and shape gold islands were not chiral and do not exhibit any CD signal, on coating of riboflavin in the PMMA solution the Au islands, a new CD signal appeared at the plasmon resonance wavelength range (Figure 52A). When the PMMA layer with chiral molecules was washed away using organic solvent such as

acetone, the CD signal completely disappeared. These interesting resulted reveal important phenomenon of induced-CD. Also, achiral polyelectrolytes were used to build the LbL spacer, and the last two layers were alternating riboflavin 5'-monophosphate bound to the positively charged polymers. The spacing between the riboflavin and the gold surface can be tuned by changing the layer pair of the polyelectrolytes. The induced plasmonic CD signal was strong enough to be measured from a bilayer of riboflavin 5'-monophosphate at sub 10 nm separation distances (Figure 52B).

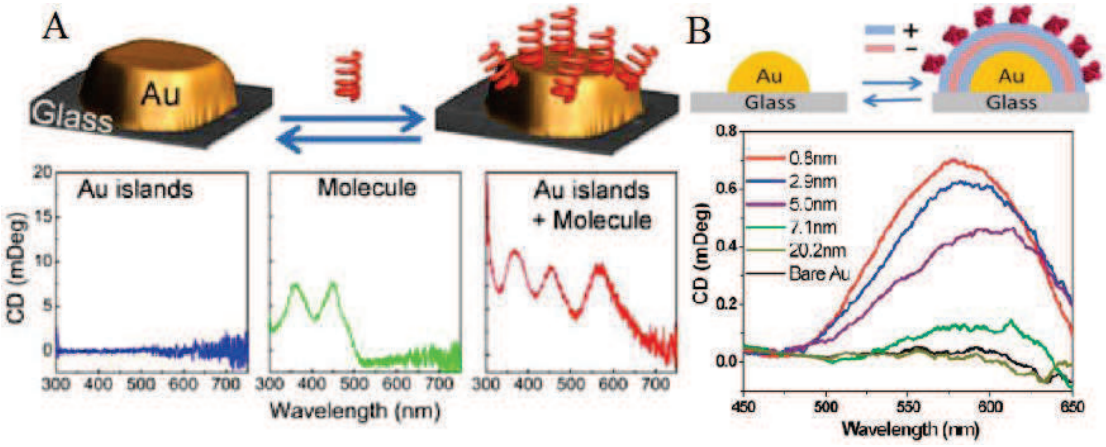

Figure 52. (A) Schematic illustration of the experiment on induced-CD by bringing chiral molecules (riboflavin), it can be seen that on combining the chiral molecules with gold particles a new CD peak appears at the metal plasmon resonance. (B) A scheme of the LbL experiment, CD spectra from Riboflavin derivative with different distance from Au surface.[96]

Tang and co-workers studied the induced CD response by one-dimensional (1D) assembly of cysteine (CYS) and gold nanorods (GNRs).[97] The gold nanorods form end-to-end assembly by the electrostatic interaction of CYS molecules preferentially attached on the ends of different GNRs. Interestingly, although three types of 1D assemblies containing L-, D- or DL-CYS, respectively, exhibit the same optical absorption in the UV-vis-NIR region (Figure 53A). Their CD responses in the same region are totally different (Figure 53C). L and D-CYS-assembled GNRs present

mirrored line shape in the CD spectra, but DL-CYS assembled GNRs show no chiral effect because of the compensation effect. In addition, the wavelength of the CD responses can be tuned from 550 nm to more than 900 nm by changing the aspect ratios of the gold nanorods. Anisotropic enhancement of the optical properties is observed, suggesting that the enhancement of the longitudinal surface plasmon resonance peak of GNRs in the CD response in more obvious than the transverse surface plasmon resonance.

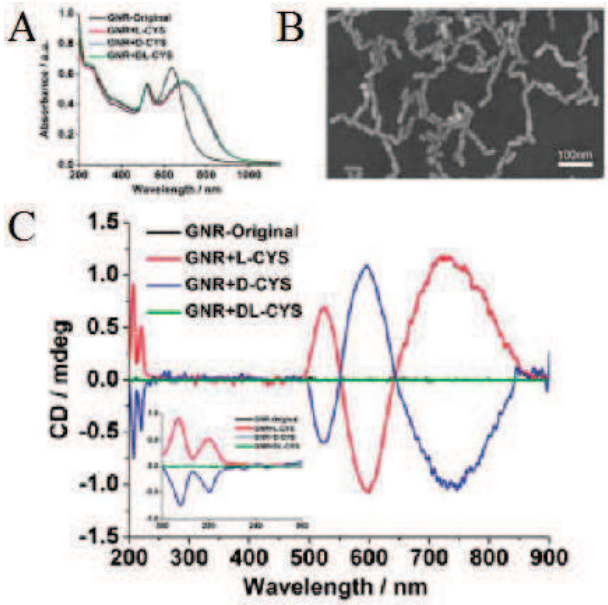

Figure 53. (A) UV-vis-NIR spectra of the GNRs and 1D self-assembled GNRs formed by three types of CYS. (B) SEM image of the self-assembled GNRs. (C) CD spectra of original GNRs and assembled GNRs by different type of CYS.[97]

The previous two examples of induced CD are originated from the chiral molecules. Thomas et al. reported the in situ growth of Au nanoparticles on D- and L-isomers of diphenylalanie peptide nanotubes (PNT), in which the chirality was transferred from the surfaces to the nanomaterials.[98] The ethylene glycol thiol protected gold nanoparticles were added to both D- and L-isomer of PNT, the PNT seeded with EG-Au nanoparticles was further mixed with an aqueous solution of $HAuCl_4$ and the

solution was irradiated at 300 nm in a photochemical reactor for 3 h. It was found that the EG-Au nanoparticles seeded on the PNT can act as the nucleation site and the the chiral molecules on their surface provide a restricted environment, which drives the selective growth of nanoparticles as bunches. The gold nanoparticle bunches on D-and L-isomers of PNT showed bisignated CD signal with symmetrical mirror images at the gold surface plasmon frequency (Figure 54). The D-isomers of PNT showed positive followed by negative cotton effects (positive couplet). However, an inversion of CD signal was observed with negative followed by positive cotton effects for the L-isomer (negative couplet).

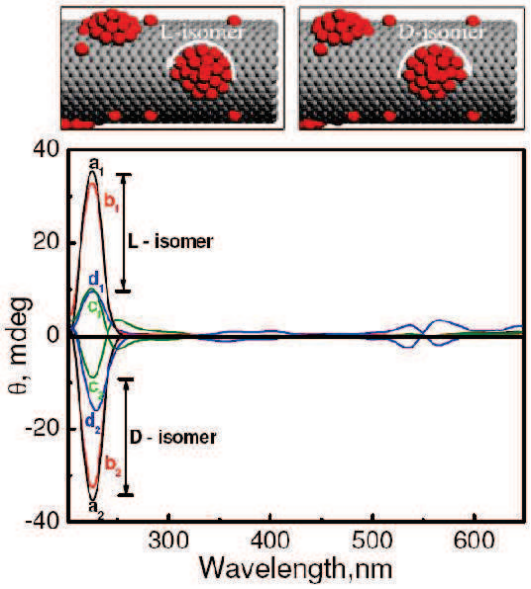

Figure 54. Schematic illustration of gold nanoparticle bunches on D- and L-isomers of PNT. CD spectra of (a_1, a_2, black trace) L- and D-isomers of PNT in a mixture of water and hexafluoro-2-propanol (99:1) at pH 10. CD spectra on subsequent addition of (b_1, b_2, red traces) EG-Au nanoparticles, (c_1, c_2, green traces) $HAuCl_4$ to L- and D-isomers of PNT and (d1, d2, blue traces) after photochemical irradiation of the resultant solution for 3 h.[98]

Bibliography

1. Xia, Y.; Yang, P.; Sun, Y.; Wu, Y.; Mayers, B.; Gates, B.; Yin, Y.; Kim, F.; Yan, H. *Adv. Mater.* **2003**, *15*, 353-389.

2. Liu, Z.; Xu, J.; Chen, D.; Shen, G. *Chem. Soc. Rev.* **2015**, *44*, 161-192.

3. Dasgupta, N. P.; Sun, J.; Liu, C.; Brittman, S.; Andrews, S. C.; Lim, J.; Gao, H.; Yan, R.; Yang, P. *Adv. Mater.* **2014**, *26*, 2137-2184.

4. Hochbaum, A. I.; Yang, P. D. *Chem. Rev.* 2010, 110, 527-546.

5. Yang, P. D.; Yan, R. X.; Fardy, M. *Nano Lett.* 2010, 10, 1529-1536.

6. Yan, H.; Park, S. H.; Finkelstein, G.; Reif, J. H.; LaBean, T. H. *Science* 2003, 301, 1882-1884.

7. Qing, Q.; Pal, S. K.; Tian, B.; Duan, X.; Timko, B. P.; Cohen-Karni, T.; Murthy, V. N.; Lieber, C. M. *Proc. Natl. Acad. Sci. U. S. A.* 2010, 107, 1882-1887.

8. Jiang, L.; Dong, H. L.; Hu, W. P.; *Soft Matter* 2011, 7, 1615-1630.

9. Su, B.; Wu, Y.; Jiang, L. *Chem. Soc. Rev.* 2012, 41, 7832-7856.

10. Ziegler, K. J.; Polyakov, B.; Kulkarni, J. S.; Crowley, T. A.; Ryan, K. M.; Morris, M. A.; Erts, D.; Holmes, J. D. *J. Mater. Chem.* 2004, 14, 585-589.

11. Liu, J. W.; Liang, H. W.; Yu, S. H. *Chem. Rev.* 2012, 112, 4770-4799.

12. Long, Y. Z.; Yu, M.; Sun, B.; Gu, C. Z.; Fan, Z. *Chem. Soc. Rev.* 2012, 41, 4560-4580.

13. Guo, Q. J.; Teng, X. W.; Rahman, S.; Yang, H. *J. Am. Chem. Soc.* 2003, 125, 630-631.

14. Cote, L. J.; Kim, F.; Huang, J. X. *J. Am. Chem. Soc.* 2009, 131, 1043-1049.

15. Yang, P. D. *Nature* 2003, 425, 243-244.

16. Tao, A. R.; Huang, J. X.; Yang, P. D. *Acc. Chem. Res.* 2008, 41, 1662-1673.

17. Liu, J. W.; Zhu, J. H.; Zhang, C. L.; Liang, H. W.; Yu, S. H. *J. Am. Chem. Soc.* 2010, 132, 8945-8952.

18. Whang, D.; Jin, S.; Wu, Y.; Lieber, C. M. *Nano Lett.* 2003, 3, 1255-1259.

19. Jin, S.; Whang, D. M.; McAlpine, M. C.; Friedman, R. S.; Wu, Y.; Lieber, C. M. *Nano Lett.* 2004, 4, 915-919.

20. Jana, N. R. *Angew. Chem., Int. Ed.* 2004, 43, 1536-1540.

21. Sau, T. K.; Murphy, C. J. *Langmuir* 2005, 21, 2923-2929

22. Singh, A.; Gunning, R. D.; Ahmed, S.; Barrett, C. A.; English, N. J.; Garate, J. A.; Ryan, K. M. *J. Mater. Chem.* 2012, 22, 1562-1569.

23. Du, Y. P.; Zhang, Y. W.; Yan, Z. G.; Sun, L. D.; Yan, C. H. *J. Am. Chem. Soc.* 2009, 131, 16364-16365.

24. Knowles, T. P. J.; Oppenheim, T. W.; Buell, A. K.; Chirgade, D. Y.; Welland, M. E. *Nat. Nanotechnol.* 2010, 5, 204-207.

25. Xu, W.; Leeladhar, R.; Tsai, Y. T.; Yang, E. H.; Choi, C. H. *Appl. Phys. Lett.* 2011, 98, 073101.

26. Shi, H. Y.; Hu, B.; Yu, X. C.; Zhao, R. L.; Ren, X. F.; Liu, S. L.; Liu, J. W.; Feng, M.; Xu, A. W.; Yu, S. H. *Adv. Funct. Mater.* 2010, 20, 958-964.

27. Liu, J. W.; Zhang, S. Y.; Qi, H.; Wen, W. C.; Yu, S. H. *Small* 2012, 8, 2412-2420.

28. Zhang, C. Y.; Zhang, X. J.; Zhang, X. H.; Ou, X. M.; Zhang, W. F.; Jie, J. S.; Chang, J. C.; Lee, C. S.; Lee, S. T. *Adv. Mater.* 2009, 21, 4172-4175.

29. Fragouli, D.; Buonsanti, R.; Bertoni, G.; Sangregorio, C.; Innocenti, C.; Falqui, A.; Gatteschi, D.; Cozzoli, P. D.; Athanassiou, A.; Cingolani, R. *ACS Nano* 2010, 4, 1873-1878.

30. Wang, B.; Ma, Y. F.; Li, N.; Wu, Y. P.; Li, F. F.; Chen, Y. S. *Adv. Mater.* 2010, 22, 3067-3070.

31. Ryan, K. M.; Mastroianni, A.; Stancil, K. A.; Liu, H.; Alivisatos, A. P. *Nano Lett.* 2006, 6, 1479-1482.

32. Carbone, L.; Nobile, C.; De Giorgi, M.; Sala, F. D.; Morello, G.; Pompa, P.; Hytch, M.; Snoeck, E.; Fiore, A.; Franchini, I. R.; Nadasan, M.; Silvestre, A. F.; Chiodo, L.; Kudera, S.; Cingolani, R.; Krahne, R.; Manna, L. *Nano Lett.* 2007, 7, 2942-2950.

33. Smith, P. A.; Nordquist, C. D.; Jackson, T. N.; Mayer, T. S.; Martin, B. R.; Mbindyo, J.; Mallouk T. E. *Appl. Phys. Lett.* 2000, 77, 1399-1401.

34. Huang, Y.; Dduan, X. F.; Wei, Q. Q.; Lieber, C. M. Science 2001. 291, 630-633.

35. Zhang, Q.; Gupta, S.; Emrick, T.; Russell, T. P. *J. Am. Chem. Soc.* 2006, 128, 3898-3899.

36. Nepal, D.; Onses, M. S.; Park, K.; Jespersen, M.; Thode, C. J.; Nealey, P. F.; Vaia, R. A. *ACS Nano* 2012, 6, 5693-5701.

37. Liu, S.; Tok, J. B. H.; Locklin, J.; Bao, Z. *Small*, 2006, 2, 1448-1453.

38. Liu, J. W.; Wang, J. L.; Huang, W. R.; Yu, L.; Ren, X. F.; Wen, W. C.; Yu, S. H. *Sci. Rep.* 2012, 2, 987.

39. Zan, X.; Feng, S.; Balizan, E.; Lin, Y.; Wang, Q. *ACS Nano* 2013, 7, 8385-8396.

40. Yu, G. H.; Cao, A. Y.; Lieber, C. M. *Nat. Nanotechnol.* 2007, 2, 372-377.

41. Merritt, S. R.; Exner, A. A.; Lee, Z. H.; von Recum, H. A.; *Adv. Eng. Mater.* 2012, 14, B266-B278.

42. Li, D.; Wang, Y. L.; Xia, Y. N. *Adv. Mater.* 2004, 16, 361-366.

43. Yang, H.; Liu, Y. Q.; Zhang, X. P.; Xia, Y. N. *Adv. Mater.* 2010, 22, 2454-2457.

44. Xu, C. Y.; Inai, R.; Kotaki, M.; Ramakrishna, S. *Biomaterials* 2004, 25, 877-886.

45. Yang, W.; Qu, L.; Zheng, R.; Liu, Z.; Ratinac, K. R.; Shen, L.; Yu, D.; Yang, L.; Barrow, C. J.; Ringer, S. P.; Dai, L.; Braet, F. *Chem. Mater.* 2011, 23, 2760-2765.

46. Leow, W. W.; Hwang, W. *Langmuir* 2011, 27, 10907-10913.

47. Li, Y.; Wu, Y. *J. Am. Chem. Soc.* 2009, 131, 5851-5857.

48. Assad, O.; Leshansky, A. M.; Wang, B.; Stelzner, T.; Christiansen, S.; Haick, H. *ACS Nano* 2012, 6, 4702-4712.

49. Freitag, M.; Martin, Y.; Misewich, J. A.; Martel, R.; Avouris, P. H. *Nano Lett.* 2003, 3, 1067-1071.

50. Srivastava, A.; Srivastava, O. N.; Talapatra, S.; Vajtai, R.; Ajayan, P. M. *Nat. Mater.* 2004, 3, 610-614.

51. Peng, X. S.; Karan, S.; Ichinose, I. *Langmuir* 2009, 25, 8514-8518.

52. Liang, H. W.; Wang, L.; Chen, P. Y.; Lin, H. T.; Chen, L. F.; He, D.; Yu, S. H. *Adv. Mater.* 2010, 22, 4691-4695.

53. Iler, R. K. *J. Colloid Interf. Sci.* 1966, 21, 569-594.

54. Decher, G.; Hong, J. D.; Schmitt, J. *Thin Solid Films* 1992, 210, 831-835.

55. Decher, G. Science 1997, 277, 1232-1237.

56. Schlenoff, J. B.; Dubas, S. T.; Farhat, T. *Langmuir* 2000, 16, 9968-9969.

57. Izquierdo, A.; Ono, S. S.; Voegel, J. C.; Schaaf, P.; Decher, G. *Langmuir* 2005,

21, 7558-7567.

58. Vozar, S.; Poh, Y.; Serbowicz, T.; Bachner, M.; Podsiadlo, P.; Qin, M.; Verploegen, E.; Kotov, N.; Hart, A. J. *Rev. Sci. Instrum.* 2009, 80, 023903.
59. Stockton, W. B.; Rubner, M. F. *Macromolecules* 1997, 30, 2717-2725.
60. Liang, Z. Q.; Wang, Q. *Langmuir* 2004, 20, 9600-9606.
61. Anzai, J. I.; Kobayashi, Y.; Nakamura, N.; Nishimura, M.; Hoshi, T. *Langmuir* 1999, 15, 221-226.
62. Muller, W.; Ringsdorf, H.; Rump, E.; Wildburg, G.; Zhang, X.; Angermaier, L.; Knoll, W.; Liley, M.; Spinke, J. *Science* 1993, 262, 1706-1708.
63. Lojou, E.; Bianco, P. *Langmuir* 2004, 20, 748-755.
64. Qureshi, S. S.; Zheng, Z. Q.; Sarwar, M. I.; Felix, O.; Decher, G. *ACS Nano* 2013, 7, 9336-9344.
65. Pichon, B. P.; Louet, P.; Felix, O.; Drillon, M.; Begin-Colin, S.; Decher, G. *Chem. Mater.* 2011, 23, 3668-3675.
66. Dontsova, D.; Keller, V.; Keller, N.; Steffanut, P.; Felix, O.; Decher, G. *Macromol. Rapid Commun.* 2011, 32, 1145-1149.
67. Schneider, G.; Decher, G. *Nano Lett.* 2004, 4, 1833-1839.
68. Jiang, C. Y.; Markutsya, S.; Tsukruk, V. V. *Langmuir* 2004, 20, 882-890.
69. Rogach, A. L.; Koktysh, D. S.; Harrison, M.; Kotov, N. A. *Chem. Mater.* 2000, 12, 1526-1528.
70. Detsri, E.; Popanyasak, J. *Colloids and Surfaces A: Physicochem. Eng. Aspects* 2015, 467, 57-65.
71. Sham, A. Y. W.; Notley, S. M. *Langmuir* 2014, 30, 2410-2418.
72. Xiao, F. X.; Miao, J.; Liu, B. *J. Am. Chem. Soc.* 2014, 136, 1559-1569.
73. Sakai, N.; Sasaki, T.; Matsubara, K.; Tatsuma, T. *J. Mater. Chem.* 2010, 20, 4371-4378.
74. Choi, W.; Choi, J.; Bang, J.; Lee, J. H. *ACS Appl. Mater. Interfaces* 2013, 5, 12510-12519.
75. Lutkenhaus, J. L.; Olivetti, E. A.; Verploegen, E. A.; Cord, B. M.; Sadoway, D. R.; Hammond, P. T. *Langmuir* 2007, 23, 8515-8521.

76. Podsiadlo, P.; Kaushik, A. K.; Arruda, E. M.; Waas, A. M.; Shim, B. S.; Xu, J.; Nandivada, H.; Pumplin, B. G.; Lahann, J.; Ramamoorthy, A.; Kotov, N. A. *Science* 2007, 318, 80-83.

77. Zhang, S. C.; Shen, J. D.; Fu, H. B.; Dong, W. Y.; Zheng, Z. J.; Shi, L. Y. J. Solid State Chem. 2007, 180, 1456-1463.

78. Podsiadlo, P.; Sui, L.; Elkasabi, Y.; Burgardt, P.; Lee, J.; Miryala, A.; Kusumaatmaja, W.; Carman, M. R.; Shtein, M.; Kieffer, J.; Lahann, J.; Kotov, N. A. Langmuir 2007, 23, 7901-7906.

79. Gunawidjaja, R.; Jiang, C. Y.; Peleshanko, S.; Ornatska, M.; Singamaneni, S. Tsukruk, V. V. *Adv. Funct. Mater.* 2006, 16, 2024-2034.

80. Vial, S.; Pastoriza-Santos, I.; Perez-Juste, J.; Liz-Marzan, L. M. *Langmuir* 2007, 23, 4606-4611.

81. Wang, Y.; Tang, Z. Y.; Podsiadlo, P.; Elkasabi, Y.; Lahann, J.; Kotov, N. A. *Adv. Mater.* 2006, 18, 518-522.

82. Ben-Moshe, A.; Maoz, B. M.; Govorov, A. O.; Markovich, G. *Chem. Soc. Rev.* 2013, 42, 7028-7041.

83. Wang Y.; Xu, J.; Wang, Y. W.; Chen, H. Y. *Chem. Soc. Rev.* 2013, 42, 2930-2962.

84. Che, S.; Liu, Z.; Ohsuna, T.; Sakamoto, K.; Terasaki, O.; Tatsumi, T. *Nature* 2004, 429, 281-284.

85. Liu, S.; Han, L.; Duan, Y.; Asahina, S.; Terasaki, O.; Cao, Y.; Liu, B.; Ma, L.; Zhang, J.; Che, S. *Nat. Commun.* 2012, 3, 1215.

86. Shopsowitz, K. E.; Qi, H.; Hamad, W. Y.; MacLachlan, M. J. *Nature* 2010, 468, 422-426.

87. Hentschel, M.; Wu, L.; Schaferling, M.; Bai, P.; Li, E. P.; Giessen, H. *ACS Nano* 2012, 6, 10335-10345.

88. Kuwata-Gonokami, M.; Saito, N.; Ino, Y.; Kauranen, M.; Jefimovs, K.; Vallius, T.; Turunen, J.; Svirko, Y. *Phys. Rev. Lett.* 2005, 95, 227401.

89. Maoz, B. M.; Ben-Moshe, A.; Vestler, D.; Bar-Eli, O.; Markovich, G. *Nano Lett.* 2012, 12, 2357-2362.

90. Kuzyk, A.; Schreiber, R.; Fan, Z.; Pardatscher, G.; Roller, E. M.; Hogele, A.; Simmel, F. C.; Govorov, A. O.; Liedl, T. *Nature* 2012, 483, 311-314.

91. Lan, X.; Lu, X.; Shen, C.; Ke, Y.; Ni, W.; Wang, Q. *J. Am. Chem. Soc.* 2015, 137, 457-462.

92. Guerrero-Martinez, A.; Auguie, B.; Alonso-Gomez, J. L.; Dzolic, Z.; Gomez-Grana, S.; Zinic, M.; Cid, M. M.; Liz-Marzan, L. M. *Angew. Chem. Int. Ed.* 2011, 50, 5499-5503.

93. Querejeta-Fernandez, A.; Chauve, G.; Methot, M.; Bouchard, J.; Kumacheva, E. *J. Am. Chem. Soc.* 2014, 136, 4788-4793.

94. Ben-Moshe, A.; Govorov, A. O.; Markovich, G. *Angew. Chem. Int. Ed.* 2013, 52, 1275-1279.

95. Bosnich, B. *J. Am. Chem. Soc.* 1966, 88, 2606.

96. Maoz, B. M.; Chaikin, Y.; Tesler, A. B.; Elli, O. B.; Fan, Z.; Govorov, A. O.; Markovich, G. *Nano Lett.* 2013, 13, 1203-1209.

97. Zhu, Z.; Liu, W.; Li, Z.; Han, B.; Zhou, Y.; Gao, Y.; Tang, Z. *ACS Nano* 2012, 6, 2326-2332.

98. George, J.; Thomas, K. G. *J. Am. Chem. Soc.* 2010, 132, 2502-25.

2 Materials and Methods

2.1 Materials

Poly(ethyleneimine) (PEI, $\overline{M_n}$ ≈ 60,000 g/mol), Poly(sodium 4-styrene sulfonate) (PSS, $\overline{M_w}$ ≈ 70,000), Poly(allylamine hydrochloride) (PAH, M_w ≈ 15,000), Polyvinylpyrrolidone (PVP, $\overline{M_w}$ ≈ 40,000), Silver nitrate and Glycerol, were purchased from Sigma-Aldrich, Sodium Chloride was purchased from Carl Roth GmbH Co. (Germany). All the chemicals were used without further purification.

Silicon wafers were bought from waferNet Inc. (San-Jose, USA) and quartz and glass slides from Thuet B. (Blodelsheim, France).

Ultrapure water with a resistivity of 18.2 MΩ.cm was obtained by purification with a Milli-Q Gradient system (Millipore, Molsheim, France) and was used directly after production.

1/4J-316SS air atomizing nozzles and accessories were bought from Spraying Synstems Co. (Wheaton, Unite States).

2.2 Methods

2.2.1 Model substrate cleaning procedures

The silicon wafers and glass slides used were initially rinsed extensively with ethanol and then with milli-Q water, blown dried with compressed air and then plasma activated for 3 minutes in the plasma cleaner from Harrick Plasma (Ithaca, NY, model PDC-002).

2.2.2 Synthesis of Silver nanowires

Uniform Ag nanowires were prepared according to the described method.[1-2] Briefly, 1.76 g of Polyvinylpyrrolidone (PVP) ($\overline{M_w}$ ≈ 40,000) was added into 57 mL of glycerol in a round bottom flask and the solution was kept at 90°C under stirring till a homogeneous solution was obtained. After cooling down to room temperature, 0.474 g of $AgNO_3$ was added into the solution. Then a NaCl solution (17.7 mg of NaCl

dissolving in 0.15 mL of ultrapure water and 3 mL of glycerol) was added into the flask. The flask was heated from room temperature to 210°C in 20 minutes under stirring. When temperature reached 210°C, the heating was stopped. 60 mL of ultrapure water was added and the temperature returned to room temperature. The solution was kept undisturbed for 1 week and the sediment at the bottom of the flask was collected carefully. The obtained Ag nanowires were washed several times with water by centrifugation at 4000 rpm for 30 min. Finally, the products were suspended in 170 mL of water. The concentration was found to be 1.17 mg/mL by freeze drying a portion of solution.

The obtained silver nanowire suspension was characterized by AFM, TEM, UV and Zeta-potential analyzer.

2.2.3 Preparation of polyelectrolyte solutions

Poly(ethylene imine) (PEI) solutions were freshly prepared by direct dissolution of 2.5 mg/mL of the polymer in ultrapure water. Poly(sodium 4-styrene sulfonate) (PSS) solutions were prepared in NaCl solution (0.5 M) at concentration of 0.618 mg/mL. Poly(allylamine hydrochloride) (PAH) solutions were prepared in NaCl solution (0.5 M) at concentration of 0.285 mg/mL.

2.2.4 Dip coating

For dip coating, the negatively charged substrate (silicon wafer, glass and quartz) is immersed in a beaker containing the polycation for 20 minutes followed by extensive rinsing by immersing it in a beaker of ultra-pure water for 3 times 3 minutes. This allows the removal of weakly adhered species. A layer of polyelectrolyte is deposited on the substrate. In order to deposit the oppositely charged polyelectrolyte, the coated substrate is immersed in a beaker containing a solution of the polyanion for 20 minutes followed by extensive rinsing by immersing in a beaker of ultra-pure water for 3 times 3 minutes. This leads to the deposition of a layer pair of polyelectrolyte on the substrate. The consecutive repetition of these steps leads to the preparation of a multilayerd film.

2.2.5 Film build-up by "Spraying"

Two different devices are used for the preparation of sprayed layer-by-layer assembled films.

The first spray device used is the "air-boy" spray bottle from Carl Roth GmH (Germany). It is a pressure atomizer made of poly(propylene) and poly(ethylene) with a monocomponent nozzle in which 200 mL of the liquid to be sprayed is under pressure. This pressure allows the liquid manually pumped from the spray bottle.

The second spray device is a home-made automated system connected to pumps and pressure gauges allowing the control of the air flow and the liquid flow rate in the spray via a connected computer (Scheme 1). The nozzle used in this case is an air assisted nozzle in which a high flow of air stream shear the liquid jet into spray droplets. Adjusting these parameters result in a spray with controllable velocity and droplet size.

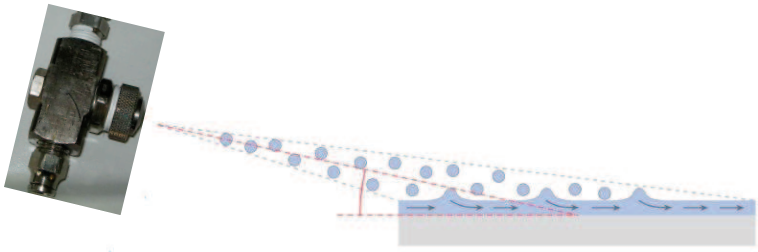

Scheme 1. Schematic representation of grazing-incidence spraying (GIS), the spraying direction is about 15° in related to the receiving surface.

For film build-up, the substrates were first orthogonally sprayed with the PEI solution for 10 seconds using Air-Boy spraying bottles followed by rinsing with pure water for 10 seconds using Air-Boy spraying bottles.

Silver nanowires were deposited on the PEI-coaded substrates for 200 seconds (unless otherwise specified) using an air atomizing nozzle. The liquid flow rate was set to 1 mL/min and the air flow to 30 L/min. The angle between the spray cone main axis and the receiving substrate was 15°. The deposition of AgNW was followed by a rinsing step with water for 100 seconds using a same kind of nozzle fed with air at 25

L/min and water at 10 mL/min. The nozzle was held at a distance of 1 cm from the substrate. Finally, the substrates were dried using a stream of air flow.

For AgNW multilayer buildup, PSS/PAH polyelectrolyte multilayers were deposited by orthogonal spraying using Air-Boy spraying bottles for 10 seconds. Each polyelectrolyte deposition was followed by a rinsing step with water for 10 seconds.

A multilayer of PEI/$(PSS/PAH)_5$/PSS/PEI was deposited on the PEI/AgNW films, followed by grazing-incidence spraying of a subsequent AgNW layer in the same conditions as those used for the first layer.

2.2.6 Transmission electron microscopy

The first TEM was built by Max Knoll and Ernst Ruska. TEM is a microscopy technique in which a beam of electrons is transmitted through an ultra-thin specimen, interacting with the specimen as it passes through. An image is formed from the interaction of the electrons transmitted through the specimen; the image is magnified and focused onto an imaging device: such as a fluorescent screen, on a layer of photographic film, or to the detected by a sensor such as a CCD camera.

TEMs are capable of imaging at a significantly higher resolution than light microscopes. This enables the instrument's user to examine fine detail-even as small as a single column of atoms, which is thousands of times smaller than the smallest resolvable object in a light microscope. TEM forms a major analysis method in a range of scientific fields, in both physical and biological sciences. TEMs find application in cancer research, virology, materials science as well as pollution nanotechnology and semiconductor research.

A TEM is composed of several components, which include a electron emission source for generation of the electron stream, a vacuum system in which the electrons travel, a series of electromagnetic lenses, as well as electrostatic plates. The latter two allow the operator to guide and manipulate the beam as required. Also required is a device to allow the insertion into, motion within, and removal of specimens from the beam path. Imaging devices are subsequently used to create an image from the electrons that exit the system.

The sample is usually placed on a standard size of grid, which is holded on a specimen holder. Standard TEM grid sizes are a 3.05 mm diameter ring, with a thickness and mesh size ranging from a few to 100 μm. The sample is placed onto the inner meshed area having diameter of approximately 2.5 mm. Usual grid materials are molybdenum, copper, gold or platinum.

Once inserted into a TEM, the sample often has to be manipulated to present the region of interest to the beam, such as in single grain diffraction, in a specific orientation. To accommodate this, the TEM stage includes mechanisms for the translation of the sample in the XY plane of the sample, for Z height adjustment of the sample holder, and usually for at least one rotation degree of freedom for the sample. Thus a TEM stage may provide four degrees of freedom for the motion of the specimen. Most modern TEMs provide the ability for two orthogonal rotation angles of movement with specialized holder designs called double-tilt sample holders.

Silver nanowire (1.17 mg/mL) suspension was placed on a copper grid by drop-casing and the solvent was evaporated, then the Transmission Electron Microscopy (TEM) was performed at 200 kV with a Tecnai G2 (FEI) microscope and an Eagle 2 k (FEI) ssCCD camera.

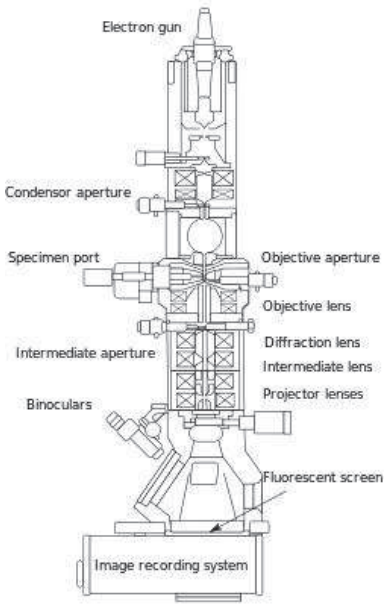

Figure 55. Schematic setup of a Transmission Electron Microscope. (https://en.wikipedia.org/wiki/Transmission_electron_microscopy) (24.09.2015)

2.2.7 Scanning electron microscopy

Scanning electron microscopy (SEM) is a type of electron microscopy that produces images of a sample by scanning it with a focused beam of electrons. The SEM consists of an electron optical column, a vacuum system, electronics and software. The electrons can interact with atoms in the sample, producing signals that can be detected and that contain information about the sample's surface morphology and composition. SEM can achieve a resolution of about 1 nanometer. Samples can be measured in low vacuum, in high vacuum and at a wide range of temperatures. Most SEM requires high conductive samples. In order to image non-conductive substrates, we usually sputter a thin layer of conductive material (gold, carbon, etc...) on the sample.

The kinds of signals produced by a SEM include back-scattered electrons (BSE), secondary electrons (SE), light (cathodoluminescence) (CL), characteristic X-rays, specimen current and transmitted electrons. In all SEM, the standard detector is the secondary electron detector. The signals developed from interactions between the electron beam and atoms at or near the surface of the sample. In the most common detection mode, secondary electron imaging or SEI, the SEM can produce very high-resolution images, showing details less than 1 nm. Because of the very narrow electron beam, SEM micrographs have a large depth of field yielding a characteristic three-dimensional appearance useful for understanding the surface structure of the sample.

Scanning electron microscopy (SEM) was performed with a JEOL 6700F equipped with a field emission gun operating at an accelerating voltage of 3 kV. The silver nanowire film can be measured directly because the conductive property of silver nanowire. To measure the side-view SEM of the multilayers, the silver nanowire thin

films on silica wafer was broken carefully with tweezer and measured immediately.

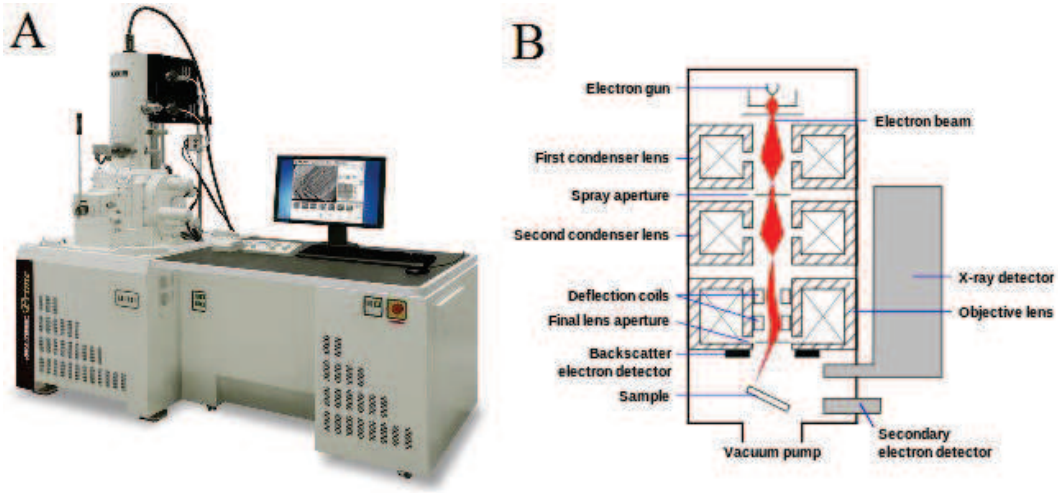

Figure 56. (A) Image of SEM from JEOL (www.jeol.com); (B) Schematic of an Scanning electron Microscopy.

(https://en.wikipedia.org/wiki/Scanning_electron_microscope) (24.09.2015)

2.2.8 Orientation analysis

The image analysis was performed using ImageJ. The nematic order parameters were got with OrientationJ, a plugin developed for ImageJ, which is based on the analysis of the structure tensor in a local neighborhood.[3] This plugin can provide a visual image and quantity of the direction and degree of orientation from a white and black image.

This software is based on the computation of the local structure tensor for each pixel of the image that is representative of the partial derevative along the x and y directions. So it is possible to calculated the direction of highest gradient of the grey, and the direction of orientation is normal to the this gradient. As a result, an orientation angle is given for each pixel, and a color-code which represents each angle by a color. Finally, the angle distribution can be extracted.

2.2.9 Atomic force microscopy

Atomic force microscopy was invented by Binning, Quate and Gerber.[4] The

resolution of AFM is in the order of 3 nm in the horizontal scale. The information is gathered by “feeling” the surface with a very sharp tip. The tip scans the surface using a piezoelectric scanner with a nanometric control of the displacement. When the tip is moved near to a sample surface, force between the tip and the sample lead to deflection of the candilever, the deflection is measured by reflecting a laser on its extremity toward a four quadrant photodiode. It is possible to image the morphology by measuring the variation of light intensity on the photodiode.

According to the nature of the tip motion, AFM is usually classified as three modes: contact mode, tapping mode and non-contact mode. Here we only discuss the contact and tapping modes.

In contact mode, the tip is close enough of the surface to feel the repulsive interaction from the surface. When the tip is moved close to the surface of the sample, the force on the cantilever will be higherand it will bend up. When the tip gets further from the substrate, the force on the cantilever will decrease and it will relax to contact with the substrate. Thus, this kind of AFM is based on the tight contact with the surface. It has the best resolution but sometimes distroy the surface.

In tapping mode, the cantilever is driven to oscillate by a small piezoelectric element mounted in the AFM tip holder. As the tip moves closer to the surface of the sample, the interaction of forces acting on the cantilever cause the amplitude of this oscillation to decrease, when the tips get further from the surface, the oscillation increase. The cantilever is oscillating near its resonance frequency. Thus, tapping AFM image is produced by imaging the force of the contact of the tip with the sample surface, the variations of the amplitude of oscillation are representative of the morphology of the surface.[5] The tapping mode is very suitable to measure the fragile samples such as polymers due to the short contact time and low force applied on the sample and it is possible to reduce the destruction of soft samples and contamination of the tip.

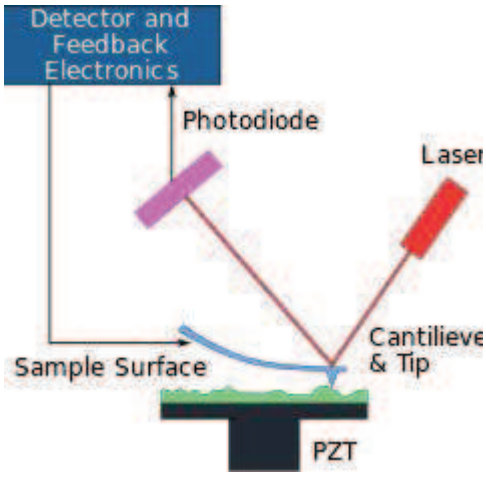

Figure 57. Block diagram of Atomic-force microscopy using beam-deflection detection.

(https://en.wikipedia.org/wiki/Atomic_force_microscopy) (24.09.2015)

The AFM images were measured in tapping mode on an AFM Multimode from Bruker Nano Surface (Palaiseau, France) with the controller Nanscope IV from Veeco (Mannheim, Germany) and non coated silicon cantilevers (resonance frequency 300 kHz, resonance constant of 40 N/m, and radius below 10 nm). The silver nanowire solutions were placed on silicon wafer and dried carefully with compressed air, then fixed on metallic supports with microscopy tape.

2.2.10 Zeta potential

Zeta potential is the electrokinetic potential in colloidal dispersions.[6] In colloidal chemistry, it is usually denoted with the Greek letter zeta (ζ).

The zeta potential plays a important role in the stability of the colloidal dispersitions. Because it indicates the degree of electrostatic repulsion between adjacent particles in the dispersion. For small molecules and particles, a high zeta potential will confer stability, so the dispersion will not precipitate. When the potential is small, attractive force may exceed this repulsion and dispersion may break and form aggregates.

The zeta potential measurements of silver nanowire suspension were performed with Zetasizer Nano Z, Malvern. The silver nanowire suspension was diluted and measured

twice at room temperature.

2.2.11 Ultraviolet-Visible Spectroscopy

Ultraviolet-Visible (UV-Visible) spectroscopy is most often used method for determining the concentrations of an absorbing species in solution. The concentration of absorbing species can be calculated using the Beer-Lambert law:

$$A = \log_{10}(I_0/I) = \varepsilon cL \qquad \textbf{Equation 1}$$

Where A is the measured absorbance, $\boldsymbol{I}_0$ is the intensity of the incident light at a given wavelength, $\boldsymbol{I}$ is the transmitted light intensity, L is the length of the cuvette containing the sample, and c is the concentration of the absorbing species. For each species an wavelength, ε is a constant known as the extinction coefficient.

The spectrophotometer measures the intensity of light after passing through a sample $\boldsymbol{I}$ and compares it to the intensity of light before it passes through the sample ($\boldsymbol{I}_0$). The ratio $\boldsymbol{I}/\boldsymbol{I}_0$ is called the transmittance and is usually expressed as a percentage (%T). The abosorbance $\boldsymbol{A}$ is based on the transmittance:

$$A = -\log(\%T/100\%) \qquad \textbf{Equation 2}$$

The basic parts of a spectrophotometer are a light source, a diffraction grating in a monochromator or a prism to separate the different wavelengths of light, and a detector.

UV-Visible-Near Infrared spectroscopy was measured with a Cary 5000 spectrometer (Agilent) in dual beam configuration. The extinction for the thin film samples was measured through a 5 mm diameter circular apperture and a blank substrate was used as a reference. A Glan-Taylor polarizer has been used for measurements under polarized light.

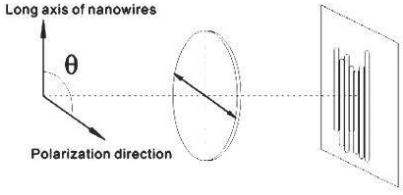

Figure 58. Schematic illustration of UV measured with a polarizer.

2.2.12 Sheet resistance measurement using 4-point probes method

Sheet resistance is a resistane of thin films that are uniform in thickness. It is usually used to characterize thin film prepared by deposition, doping or paste printing on isolated substrates such as glass and quartz slides.

The most commonly used method to characterize the sheet resistance is the 4-point probes method, which uses separate pairs of current-carrying and voltage-sensing electrodes. It is much more accurate than the two-terminal sensing technique.

The sheet resistance of the top layer can be measured very easily by four-point probe method. A current is passed through the outer probes and induces a voltage in the inner voltage probes. Using the voltage and current reading from the probe:

$$R_s = \frac{\pi}{\ln 2} \bullet \frac{V_{total}}{I} = 4.53 \frac{V_{total}}{I} \qquad \textbf{Equation 3}$$

Where R_s is the sheet resistance of the thin film, V_{total} is the voltage showed by the voltage analyzer, I is the current showed by the current analyzer. In case the sample area is large enough enough compared to the distance between the probes, the value of K is 4.53. In case the sample is very small, this value should be changed.[7]

In this thesis, the sheet resistance was measured with Agilent 34401A 6 1/2 Digit Multimeter, United Systems Corporation. The power of the equipment was set on Direct current source and the Digital multimeter was set to voltage analyzer. The voltage is supplied by Direct current source, the voltage was set to different values by a dial (for example, 1 V to 10 V), the following values of current and voltage showed by the current analyzer and voltage analyzer were recorded. Put the bottom of “reverse”, the voltage was changed from -10 to 0 V, the current was in the reverse direction. The resistance can be obtained from the slope.

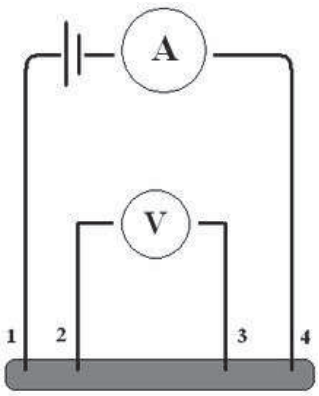

Figure 59. Schematic representation of four-point method.

(https://en.wikipedia.org/wiki/Four-terminal_sensing) (24.09.2015)

2.2.13 Circular dichroism

Circular dichroism is dichroism involving differential absorption of Left- and Right-handed polarized light.[8] This phenomenon was first discovered by Jean-Baptiste Biot, Augustin Fresnel, and Aime Cotton in 19th century.[9] It is existed in the absorption of optically active chiral molecules. CD has many applications in various fields. For instance, CD can be used to study the secondary structure of proteins.[10]

Electromagnetic radiation consists of a magnetic and electric field that oscillated vertical to each other and to the propagating direction. While linearly polarized light occurs when the electric field vector oscillates only in one plane, circularly polarized light occurs when the direction of the electric field vector rotates toward its propagation direction. Figure 60 shows the electric vectors of linearly and circularly polarized light. The plots of the circularly polarized electric vector forms a helix along the direction of propagation. For left circularly polarized light, the electric vector rotates counterclockwise. For right circularly polarized light, the electric vector rotates clockwise.[11]

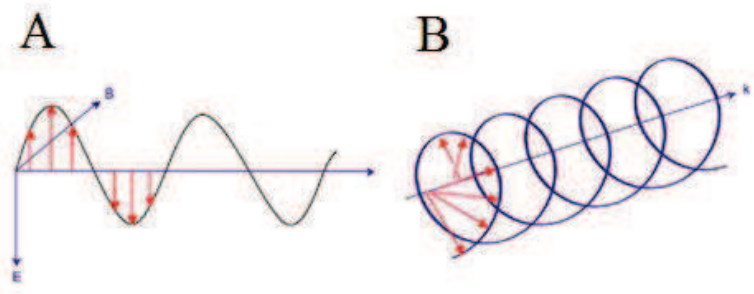

Figure 60. Schematic representation of linearly polarized light (A) and circularl polarized light (B).
(https://en.wikipedia.org/wiki/Circular_dichroism) (24.09.2015)

When circularly polarized light passes through an absorbing optically active medium such as chiral molecules or structures, it interacts differently with chiral molecules or structures, the two different types of circularly polarized light are absorbed to different extents. In a CD experiment, same amounts of left and right circularly polarized light at a selected wavelength are alternately radiated into a chiral sample. One of the polarized light is absorbed more than the other one, and this wavelength-dependent difference of absorption is measured, yielding the CD spectrum of the sample.

In this thesis, the CD measurement was done with Jasco J-1500 Circular Dichroism (CD) Spectrometer equipped with a Xenon arc lamp and the scanning speed was 200 nm/min. The chiral samples were usually measured with a 1 mm diameter pinhole sticked on the back side of the sample in order to focus on the cross point of every layer of silver nanowire, a blank substrate was used as a reference.

Delta absorbance

By definition,

$$\Delta A = A_L - A_R \qquad \textbf{Equation 4}$$

Where ΔA (Delta Absorbance) is the difference between absorbance of left circularly polarized (LCP) and right circularly polaried (RCP) light.

Molar circular dichroism

By applying Beer's law, as:

$$A = \varepsilon Cl \qquad \textbf{Equation 5}$$

We can conclude: $\Delta A = (\varepsilon_L - \varepsilon_R)Cl$ **Equation 6**

Where ε_L and ε_R are the molar extinction coefficients for LCP and RCP light, C is the molar concentration, l is the path length (cm). Then:

$$\Delta\varepsilon = \varepsilon_L - \varepsilon_R \qquad \textbf{Equation 7}$$

is the molar circular dichroism. Since $\Delta\varepsilon$ is a function of wavelength, a molar circular dichroism value ($\Delta\varepsilon$) must specify the wavelength.

Anisotropic factor (g-factor)

Generally:

$$g = \frac{\Delta\varepsilon}{\varepsilon} = \frac{\Delta A}{A} \qquad \textbf{Equation 8}$$

The ellipticity of the polarization can be defined as:

$$\tan\theta = \frac{E_R - E_L}{E_R + E_L} \qquad \textbf{Equation 9}$$

Where E_R and E_L are the magnitudes of the electric field vectors of the right-circularly and left-circularly polarized light, respectively. When E_R equals to E_L, θ is 0^o and the light is linearly polarized. When either E_R or E_L is equal to zero, θ is 45^o, the light is circularly polarized.

Uauslly, the circular dichroism effect is very small, so tanθ can be approximated as θ. Since the intensity I of light is propotional to the square of the electric-field vector, the ellipticity is:

$$\theta(radians) = \frac{(I_R^{1/2} - I_L^{1/2})}{(I_R^{1/2} + I_L^{1/2})} \qquad \textbf{Equation 10}$$

By using Beer's law:

$$I = I_0 10^{-A} = I_0 e^{-A\ln 10} \qquad \textbf{Equation 11}$$

Then the ellipticity can be written as:

$$\theta(radians) = \frac{(e^{\frac{-A_R}{2}\ln 10} - e^{\frac{-A_L}{2}\ln 10})}{(e^{\frac{-A_R}{2}\ln 10} + e^{\frac{-A_L}{2}\ln 10})} = \frac{e^{\Delta A\frac{\ln 10}{2}} - 1}{e^{\Delta A\frac{\ln 10}{2}} + 1} \qquad \textbf{Equation 12}$$

Since ΔA << 1, this expression can be approximated by expanding the exponentials in Taylor series to first-order and then discarding terms of ΔA in comparison with unity and coverting from radians to degrees:

$$\theta(\text{deg}) = \Delta A\left(\frac{\ln 10}{4}\right)\left(\frac{180}{\pi}\right) \qquad \textbf{Equation 13}$$

Therefore, g-factor can be calculated by:

$$g = \frac{\theta}{32.982 \times A} \qquad \textbf{Equation 14}$$

Bibliography

1. Yang, C.; Gu, H.; Lin, W.; Yuen, M. M.; Wong, C. P.; Xiong, M.; Gao, B. Silver Nanowires: From Scalable Synthesis to Recyclable Foldable Electronics. *Adv. Mater.* **2011**, *23*, 3052-3056.
2. Liu, J.-W.; Wang, J.-L.; Huang, W.-R.; Yu, L.; Ren, X.-F.; Wen, W.-C.; Yu, S.-H. Ordering Ag nanowire arrays by a glass capillary: A portable, reusable and durable SERS substrate. *Sci. Rep.* **2012**, *2*. 987.
3. Rezakhaniha, R.; Agianniotis, A.; Schrauwen, J. T. C.; Griffa, A.; Sage, D.; Bouten, C. V. C.; Vosse, F. N.; Unser, M.; Stergiopulos, N. *Biomech. Model. Mechanobiol.* **2012**, *11*, 461-473.
4. Binnig, G.; Quate, C. F.; Gerber, C. Atomic Force Microscope, *Phys. Rev. Lett.* 1986, 56, 930-933
5. Giesse, N. A. *Mater Today* 2009, 12, 40-45.
6. McNaught, A. D.; Wilkinson, A.; Blackwell Scientific Publications, Oxford (1997).
7. Rimini, E. Ion implantation: basics to device fabrication, 1995, pp 66-69.
8. Atkins P.; de Paula, J. Elements of Physical Chemistry. Oxford (2005), ISBN 0-7167-7329-5.
9. Fasman, G. D. Circular dichroism and the conformational analysis of biomolecules. Springer. pp.3-ISBN 978-0-306-45142-3.
10. Nakanishi, K.; Berova, N.; Woody, R. Circular dichrosim: principles and applications. VCH. pp. 473. ISBN 978-1-56081-618-8.
11. Solomon, E. I.; Lever, A. B. P. Inorganic electronic structure and spectroscopy Wiley-Interscience. pp. 78. ISBN 978-0-471-97124-5.

3 Results and Discussions

Introduction

The main goal of this thesis is to test, understand and optimize the alignment of siver nanowires by preparing challenging superstructures. In order to find the best parameter for the alignment, we first aligned the silver nanowires in monolayer, then the supertructures such as chiral plasmonic structures were prepared by combing Grazing-incidence-spraying (GIS) and Layer-by-Layer (LbL) technique . The optical properties of these structures were studied, but the goal is not to understand the optical properties in full detail.

3.1 Synthesis and characterization of Silver nanowires (AgNW)

In this thesis, the silver nanowire was prepared with polyol synthesis which involves heating a polyol with a salt precursor and polymeric capping agent to generate metal colloids. In the case of silver nanostructures, glycerol, $AgNO_3$, and poly(vinyl pyrrolidone) (PVP) serve as the polyol, salt precursor and polymeric capping agent, respectively.

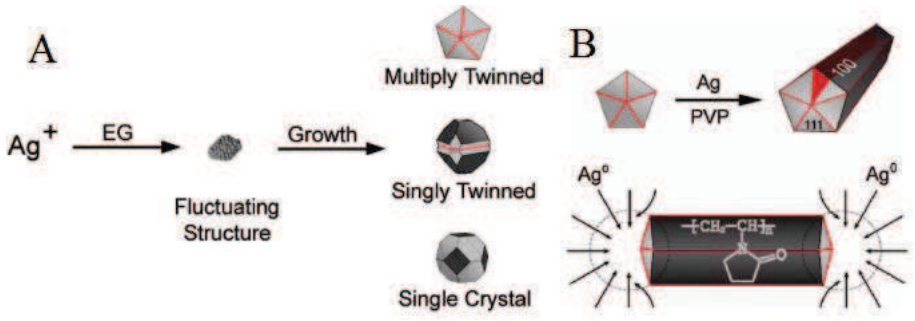

Figure 61. (A) Reduction of Ag^+ ions leads to the formation of nuclei. As nuclei grow, they are stuck as a multiply twinned, singly twinned, or single-crystal seed. (B) Once twinned seeds formed into rods. PVP selectively absorbed on {100} side facets so that silver nanowires could grow along the direction of {111} facets [1]

The nanowire suspension was imaged by AFM (Figure 62A) and TEM (Figure 62B) in order to measure their size distribution. This distribution has been determined on more than 100 nanowires in order to get a representative statistics. Nanowires have a diameter of 47 ± 6 nm and a length of 4.2 ± 1.5 µm. Figure 62C is a photograph of the silver nanowire suspension in water, which shows a greenish color.

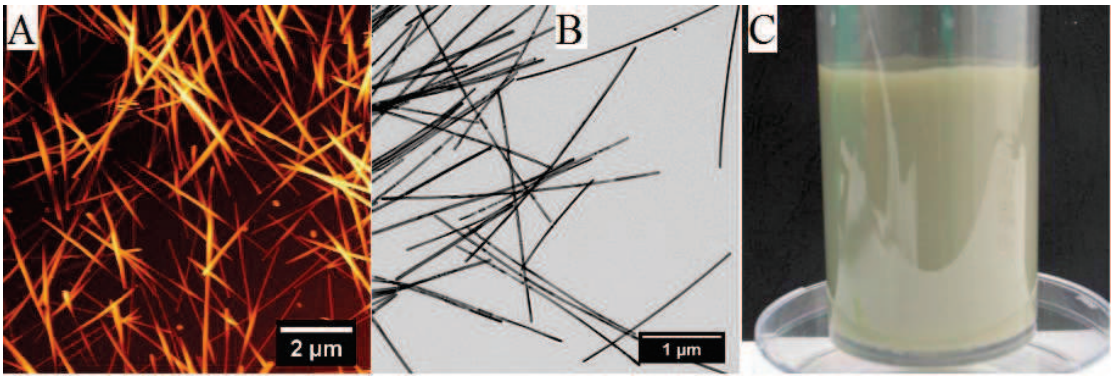

Figure 62. AFM (A), TEM (B) and the photograph (C) of the obtained AgNWs.

The silver nanowires solution was analyzed by UV-spectroscopy. The UV-spectra in Figure 63 shows that the silver nanowires have two mainly absorption peak: 350 nm and 375 nm, which may be assigned to the two different transverse modes for Ag nanowires with pentagonal cross section. Indeed, nanowires with non-circular cross-sections are known to display multiple resonance modes, and the two bands probably correspond to the out-of-plane quadrupole resonance (375 nm) and out-of-plane dipole resonance of nanowires respectively.[2] However, for the spherical metallic nanoparticles, they usually give a single peak.[3]

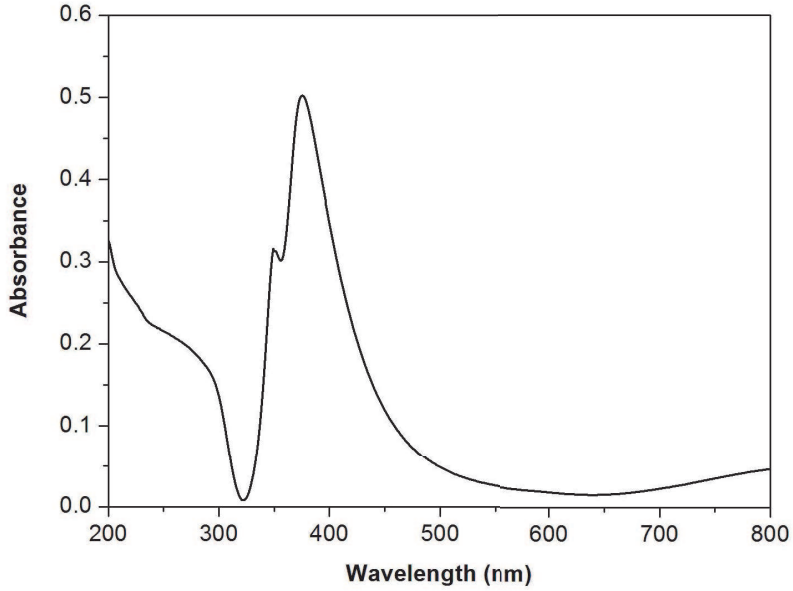

Figure 63. UV/Vis-spectrum of silver nanowire suspension in water (0.023 mg/mL).

Since the aim of this research is to align the silver nanowires in LbL coatings for different purposes, the first step is therefore to understand the construction of the LbL assembled films on standard surfaces such as silicon wafers , glass slides or quartz.

The silver nanowires solution was characterized with zeta-potential analyzer (Figure 64), which showed it is negative charged (-33.6 mV). When the silver nanowires are mixed with an oppositely charged polyelectrolyte, such as PEI, they can form particle/polyelectrolyte complexes in solution because of the electrostatic interactions. It is therefore very likely to prepare layer-by-layer assembled films from these charged materials.

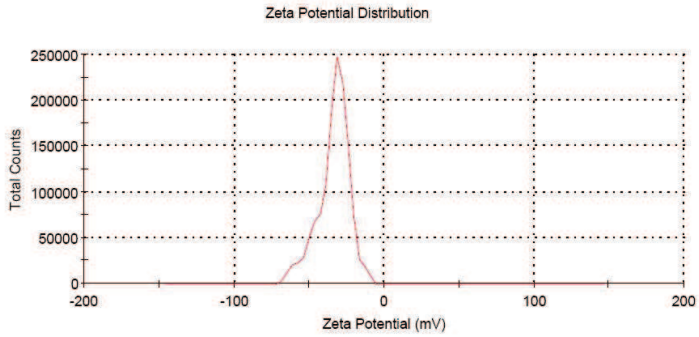

Figure 64. Zeta-potential of silver nanowire suspension in water.

3.2 Alignment of silver nanowires in monolayer

In this chapter, we try to aligned the silver nanowires with grazing-incidence spraying, a method developed in our group.[4] Grazing incidence spraying, compared to classic orthogonal spraying, has the axis of the spray jet almost in parallel to the receiving substrate and a shear force is induced along the flowing direction. It was performed using a high-speed spray-jet hitting the surface nearly parallel to the substrate at a distance of 1 cm from the nozzle.

Such aligned silver nanowire films can lead to materials with anisotropic mechanical, optical and electrical properties if the silver nanowire aligned in the same direction. Also, by combining the grazing-incidence spraying with Layer-by-Layer method, we can fabricate three dimensional architectures for example uniaxial and helical superstructures.

In order to understand the parameters can effect the alignment of the silver nanowires in the layers for each method, we first study the alignment of silver nanowires in monolayer and then alignment of silver nanowire in multilayers.

The silver nanowire deposition was carried out on a plasmon activated silicon wafer, glass or quartz slide by first spraying poly(ethylene imine) (PEI, $\overline{M_n} \approx 60{,}000$ g/mol, concentration = 2.5 mg/mL) orthogonally on the receiving surface for 10 seconds with aerosol spray bottles “Air Boy”, followed by rinsing with ultrapure water for 10 seconds. The first layer of PEI helps to promote the adhesion of the film of the substrate.

The "Grazing Incidence" spraying deposition was carried out with an automated spraying system composed of nozzles and pumps that allow the control of the air flow (AF) and the liquid flow rate (LF). The AgNW suspension was sprayed horizontally and nearly parallel to the surface at a grazing angle of 15 degree.

3.2.1 Influence of air flow (AF) on the alignment of AgNW

In order to understand the influence of the air flow on the AgNW alignment, one layer of AgNW was deposited on the PEI coated surface with different air flow (10 L/min, 20 L/min, 30 min/L and 40 min/L). These thin films were imaged by Scanning Electron Microscopy (SEM). The distribution of the angle θ between each nanowire main axis and the spraying direction is extracted from the SEM pictures. This angular distribution has been determined using the plugin OrientationJ developed for ImageJ. The nematic order parameter S can be calculated from this angle distribution and is used to characterize the quality of alignment.

$$S = \left\langle \frac{3\cos^2\theta - 1}{2} \right\rangle$$

Equation 15

The nematic order parameter S can take values between 0 and 1 where S = 0 corresponds to fully isotropic films and S = 1 corresponds to a perfectly parallel alignment (θ = 0°). Figure 65A shows the SEM image of silver nanowire film deposited at air flow of 30 L/min, the position is the 1 cm downstream from the impact point of the spray jet on the substrate. The SEM image was croped and adjusted, OrientationJ distribution was used to analysis the orientation. Then Gaussian Window was set as 1; the Hue was set as Orientation; the Saturation was set as Constant and Brightness was set as Original-Image, we got the colored image (Figure 65B), in which the nanowires are colored according to the orientation, for example, when the nanowire was perfectly aligned, the color should be almost the same as the color at 0^o (Figure 65D). The nematic order parameter S is determined as 0.90. This corresponds to ~ 77% of the nanowires aligned within ± 15° of the spraying direction, and to ~ 38% of the nanowires aligned within ± 5°.

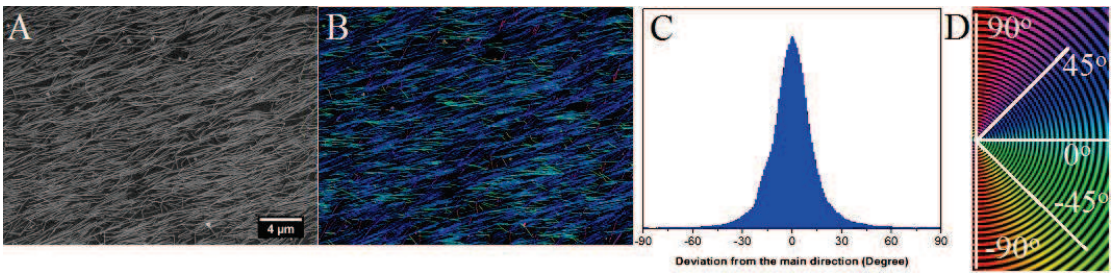

Figure 65. (A) SEM image of a silver nanowire monolayer deposited on PEI-coated silicon wafer at air flow of 30 L/min (B) Orientation analysis of (A), in which the nanowires are colored according to their orientation. (C) Distribution of angle θ in related to the spraying direction. (D) Color-code used for the orientation analysis.

Grazing-incidence spraying of AgNW with different air flow can lead to the alignment of the silver nanowire. This is due to the spraying at high spray speed nearly parallel to the receiving surface exert a shear force along the flowing direction. Figure 66 shows SEM images of silver nanowire aliged at different air flow, the distance is also 1 cm from the impact point of the spray jet. It can be seen alignment is improved as the air flow increased from 10 L/min to 30 L/min, this in mainly because the shear force increased as the increasing of the air flow. At 40 L/min, some silver nanowires are deformated with the very strong air flow. So the air flow of 30 L/min is fixed for the alignment of AgNW in the following experiments. All these samples have big oriented area, about 0.5-0.7 cm in width. It should be also noted that there are still some nanoparticles contained in these SEM pictures, maybe they were the twinned or silver nanoparticle from the synthesis.

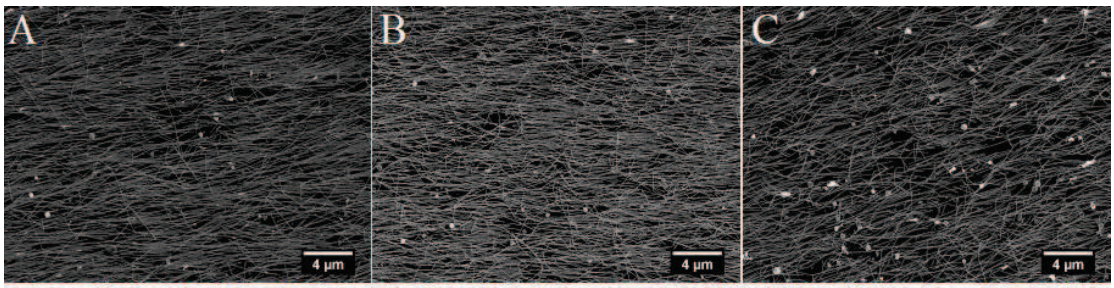

Figure 66. SEM images of silver nanowire monolayers deposited on PEI-coated silicon wafer with different air flow. (A): 10 L/min; (B): 20 L/min; (C): 40 L/min.

3.2.2 Influence of flowing distance on the alignment of AgNW

To investigate the flowing distance responsible for this controlled assembly, different positions (0.5 cm and 1.5 cm) of the monolayer silver nanowire thin film were imaged by SEM (Figure 67), it was found that silver nanowires can be ordered gradually along the flowing direction, the nematic order parameter is 0.81 at 0.5 cm downstream from the impact point of the spray jet on the substrate, when the flowing distance is about 1 cm, most of the silver nanowires are well aligned (Figure 65). Figure 67 B shows the SEM picture of the flowing distance for 1.5 cm, the density of the nanowires decrease dramatically, because the nanowires stick to the substrate gradually when it is flowing along the surface. So 1 cm is the best distance for the alignment of AgNW.

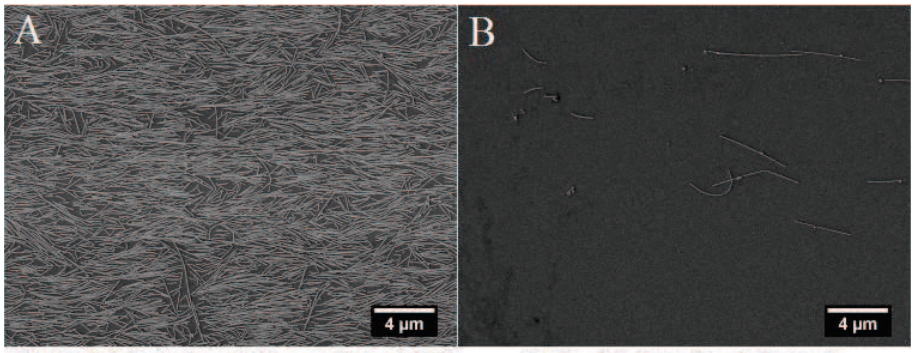

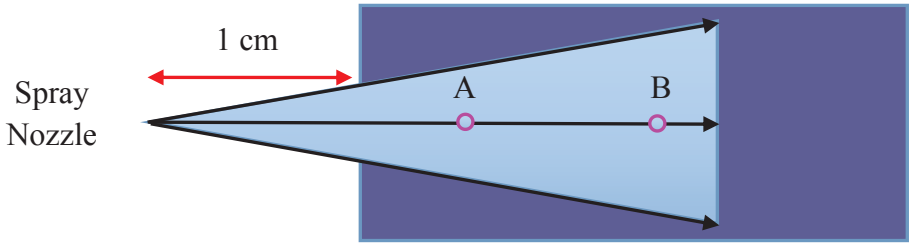

Figure 67. SEM imaged from different positions of a silver nanowire monolayer deposited on PEI-coated silicon wafer with air flow of 30 L/min. (A): 0.5 cm; (B): 1.5 cm.

3.2.3 Tuning the nanowire density by varying the spraying time

Furthermore, the nanowire density in the monolayer can be easily tuned by varying the spraying time (Figure 68). The density of nanowires was obtained by calculating the surface coverage. The SEM image was croped and adjusted by Image J, then "Shreshold" was used to make the SEM images only have two colors (white and black) and "Histogram" was run to calculate the amount of different colors. Finally, the amount of silver nanowires devided the sum amount of silver nanowires and the bare substrate yielded the surface coverage. The surface coverage was varied between 15% for 10 seconds spraying, up to 60% when the spraying is maintained for a few minutes.

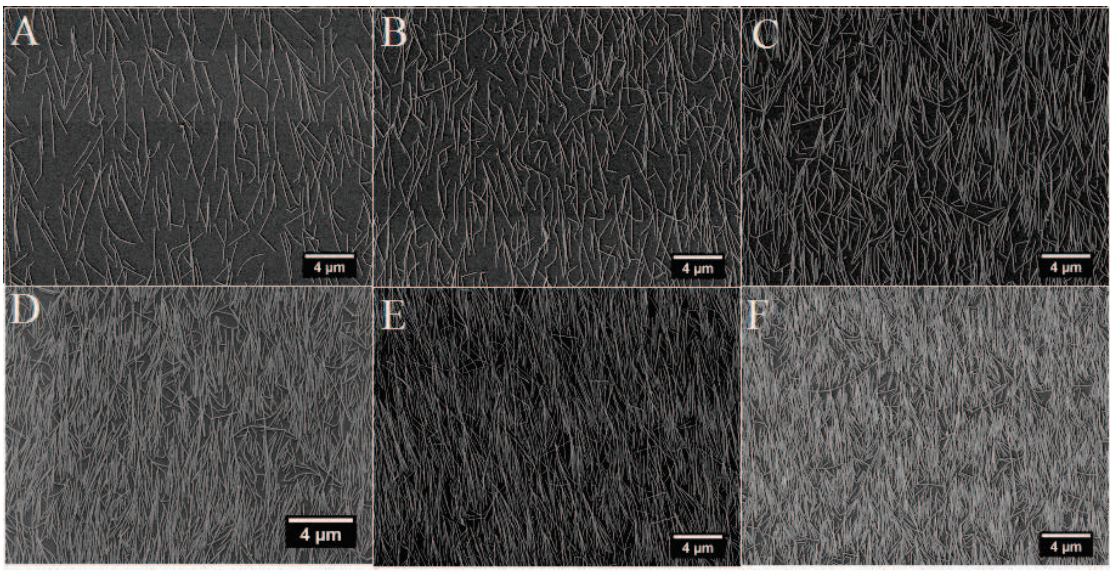

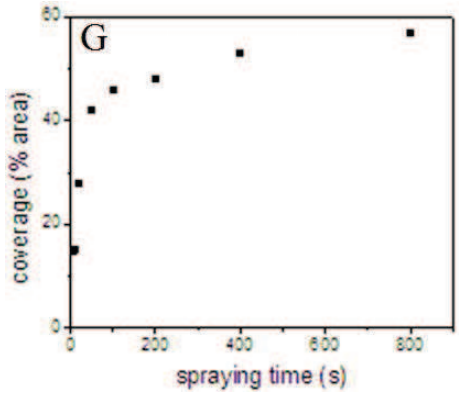

Figure 68. Alignment of silver nanowires on PEI-coated silicon wafer at different spraying times. (A) 10 s; (B) 20s; (C) 40 s; (D) 200 s; (E) 400 s; (F) 800 s. (G) Surface coverage of SEM images as function of spraying time.

3.2.4 Alignment of silver nanowires on various substrates

Silver nanowires were also sprayed on a bare silicon wafer (Figure 69A), the silicon wafer was just cleaned with ethanol and ultrapure water. From SEM piture, it can be got that most nanowires were ordered along the flowing direction, it was found that AgNWs can stick to many surfaces, the mechanism of surface-AgNW interaction not being clear. Also, some polyelectrolytes layers PEI/$(PSS/PAH)_5$/PSS/PEI were coated on the plasmon activated silicon wafer in order to keep some thickness, PEI on the top layer in used to adhere the following layer of nanowires, SEM pictures shows that the silver nanowire were also ordered along the flowing direction (Figure 69B).

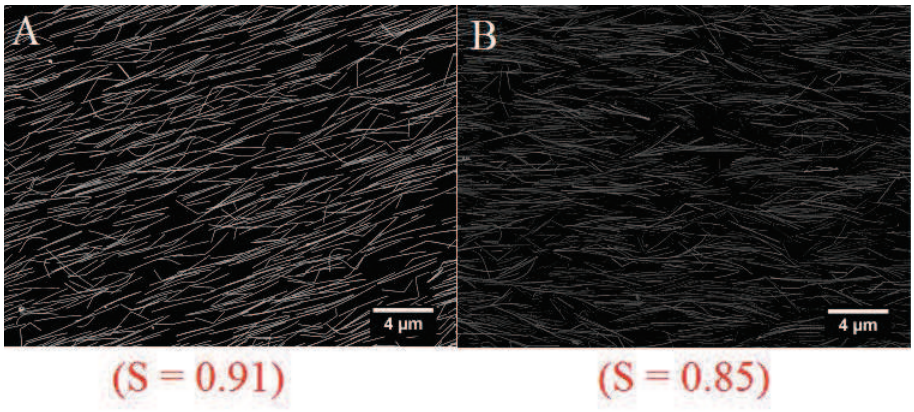

Figure 69. Alignment of silver nanowires on bare silicon wafer (A) and PEI/$(PSS/PAH)_5$/PSS/PEI coated silicon wafer.

3.2.5 Optical properties of monolayer oriented thin films of silver nanowires on silica

A oriented silver nanowire film is an anisotropic material that should exhibit an anisotropic refractive index. While standard ellipsometry is not capable of precisely determining this anisotropy, this would require general ellipsometry, it allows nevertheless to determine the anisotropy in a qualitative way. Figure 70 shows the variation of the refractive index of the film as a function of the in-plane rotation of the film. This data was obtained with ellipsometry by fitting the refractive index and keeping the film thickness constant while rotating the sample for every 20 degrees for the whole turn. When the direction of the incident light is parallel to the alignment direction of silver nanowire, the refactive index shows the minimum value. And the refractive index changed periodically as function of the in plane orientation angle, which indicated the anisotropic properties of the monolayer silver nanowire film. This method is not a highly accurate method. To further confirm the anisotropy of the monolayer thin film, we prepared the same on glass or quartz, and measure the optical properties with polarized UV.

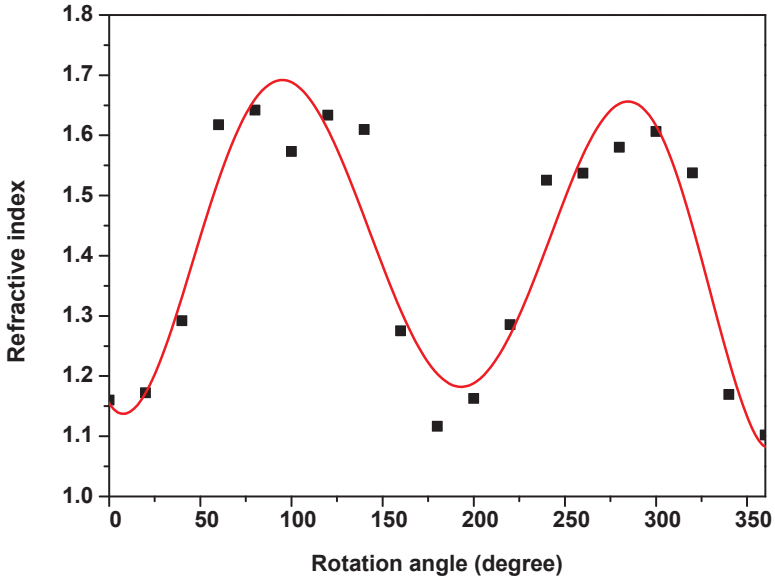

Figure 70. Dependence of refractive index as function of rotation angle of the plane. (The red line just shows a clear eye show, it doesn't have any physical meaning)

3.2.6 Optical properties of monolayer oriented thin films of Silver nanowires on glass

SEM picture (Figure 71A) shows the silver nanowires deposited on the glass slide by drop-casting, it is random oriented. The optical properties of disordered thin films display both longitudinal and transverse modes of the plasmon resonance independently of the polarization of the incident light, we measured the UV of the drop-casting silver nanowire thin film with a polarizer set in front of the thin film, the polarizer is rotated for the whole turn every 20 degrees. The polarized UV doesn't change too much from 0^{o} to 360^{o}, because the symmetric properties of the random oriented thin film (Figure 71B). The absorbance at 1500 nm is plotted as function of the rotation angle of the polarizer (Figure 71C), which presents an almost circular shape. The instrument was used without depolarizer, the spectra therefore show some artifacts from the residual polarization of the instrument.

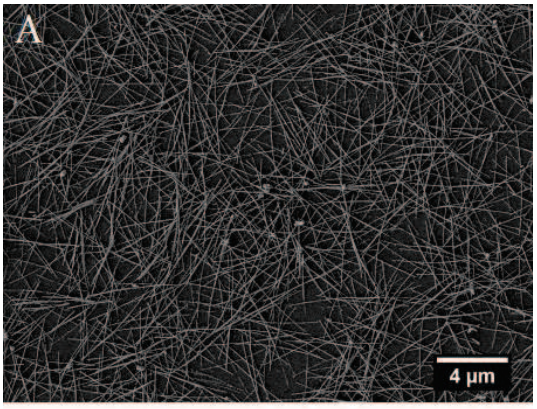

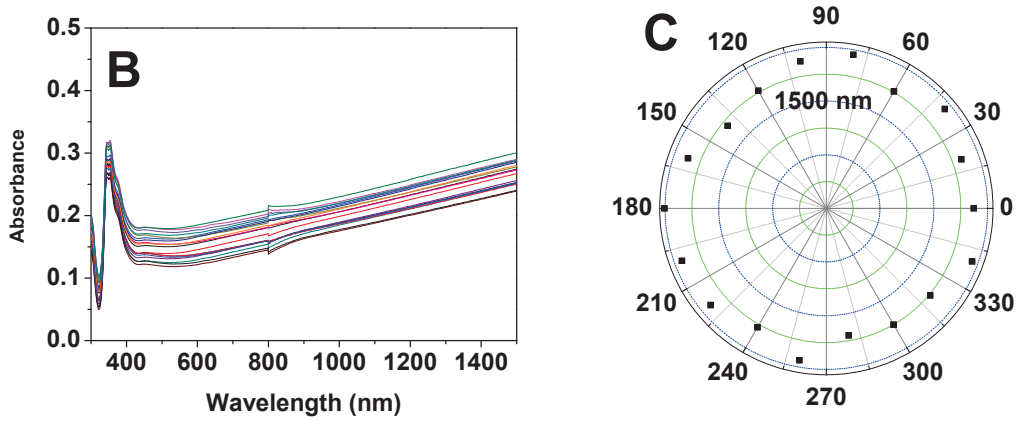

Figure 71. (A) SEM image of the random oriented silver nanowire film; (B) UV-Vis-NIR spectra of the random oriented silver nanowire film measured from 0° to 360° with a polarizer; (C) Polar plot of absorbance at 1500 nm as function of polarized angle.

When the nanowires are oriented, the optical response of the film becomes polarization-dependent. UV was measured as function of the angle Φ between the incident light beam polarization plane and the orientation direction. The spectra have been recorded for different polarization directions between 0° and 360° with 10° steps. Figure 72A shows the extinction spectra for polarization angles from 0° to 90°. When the polarization angle is increased from 0° to 90°, the absorbance in the NIR decreases, and that in the near-UV region increases. Indeed, for Φ = 0° (i.e. when the light is linearly polarized along the nanowire long axis), the longitudinal surface plasmon resonance mode is excited, which reflects in a high extinction in the NIR. Oppositely samples absorb light in the UV-visible region when the transverse surface resonance plasmon modes are excited, i.e. when the light is linearly polarized in the direction of the nanowires short axis, for Φ = 90°. For intermediate polarization angles, both modes are excited. The absorbance at 1500 nm and 378 nm (which corresponds to the resonance wavelength of the transverse dipole) is given in Figure 72B, Figure 72C is the polar plot as function of the polarization angle Φ, which shows a "8" shape. This representation underlines the polarization behavior of the nanowire oriented thin film:

in the NIR region, the extinction shows a maximum at Φ = 0 and 180° corresponding to the excitation of the SPR longitudinal modes when the polarization is collinear to the nanowire long axis and a minimum at Φ = 90 and 270°. For the transverse plasmon bands, the absorbance peaks in the near-UV range, the extinction being maximum at Φ = 90 and 270° corresponding to the excitation of the SPR transverse modes when the polarization is collinear to the nanowire short axis and a minimum at Φ = 0 and 180°. The extinction does not depend on the polarization for λ = 425 nm. Oriented nanowire thin films thus act as wavelength-dependent polarizers, in which light is polarized in the nanowire orientation direction for wavelengths below 425 nm, and light is polarized perpendicularly to the nanowire orientation direction for wavelength above 425 nm.

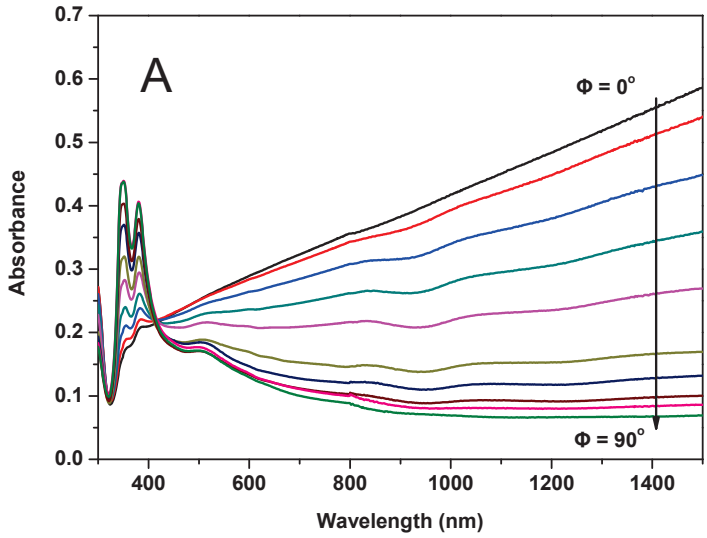

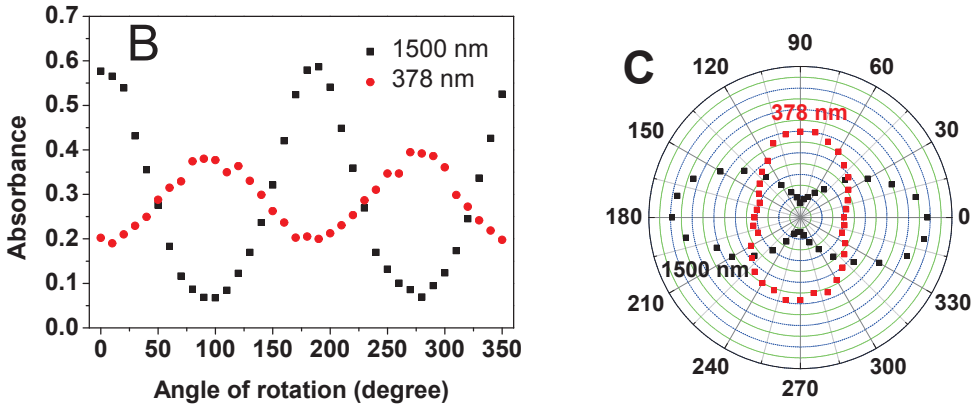

Figure 72. (A) Polarized UV-Vis-NIR spectra of oriented thin film measured from 0° to 90°; (B) Absorbance at 1500 nm and 378 nm as function of rotation angle. (C) Polar plot of B.

3.2.7 Influence of nanowire density on the optical property

The monolayer AgNW films with different spraying time (10 seconds, 50 seconds, 100 seconds and 400 seconds) were also prepared and measured with polarized UV (Figure 73A-D). We can see that all the UV curves depend on the rotation angles of the polarizer, when the polarization angle is increased from 0° to 90°, the extinction in the NIR decreases, and that in the near-UV region increases. Also the UV absorbance increased with the AgNW density. For the polarization angle of 90°, there is a peak appear at ~500 nm, the peak becomes more obviously as increasing of the silver nanowire density, it may be attributed to the transverse surface resonance modes between different nanowires. However, the peak position near 350 nm and 375 nm don't change too much, which indicates that the peak positions are little dependent on the AgNW density.

We take the UV curve at 0 degree and 90 degree to calculate the polarization efficiency. The polarization efficiency P.E. can be defined as the normalized difference between the transmittance with light polarization parallel and perpendicular to the nanowire orientation direction:

$$PE = (T_{\parallel}-T_{\perp})/(T_{\parallel}+T_{\perp}) \qquad \textbf{equation 16}$$

The polarization efficiency shows a positive maximum in the near-UV range, and becomes more and more negative when extending towards the NIR range (Figure. 73E). And the polarization efficiency increases strongly with the density of deposited silver nanowire. When the silver nanowire is coated on glass for 10 seconds, the polarization efficiency is equal to 10% at 350 nm and 11% at 1500 nm. As the spraying time increased, the polarization efficiency increased, for instance, when the spraying time increased to 400 seconds, the polarization efficiency is 33% at 350 nm and 62% at 1500 nm. However, the polarization of these monolayer films does not reach the theoretical value of 100%, if we want to go to even higher polarization efficiency (near 100%), we need to prepare the AgNW thin film in multilayers.

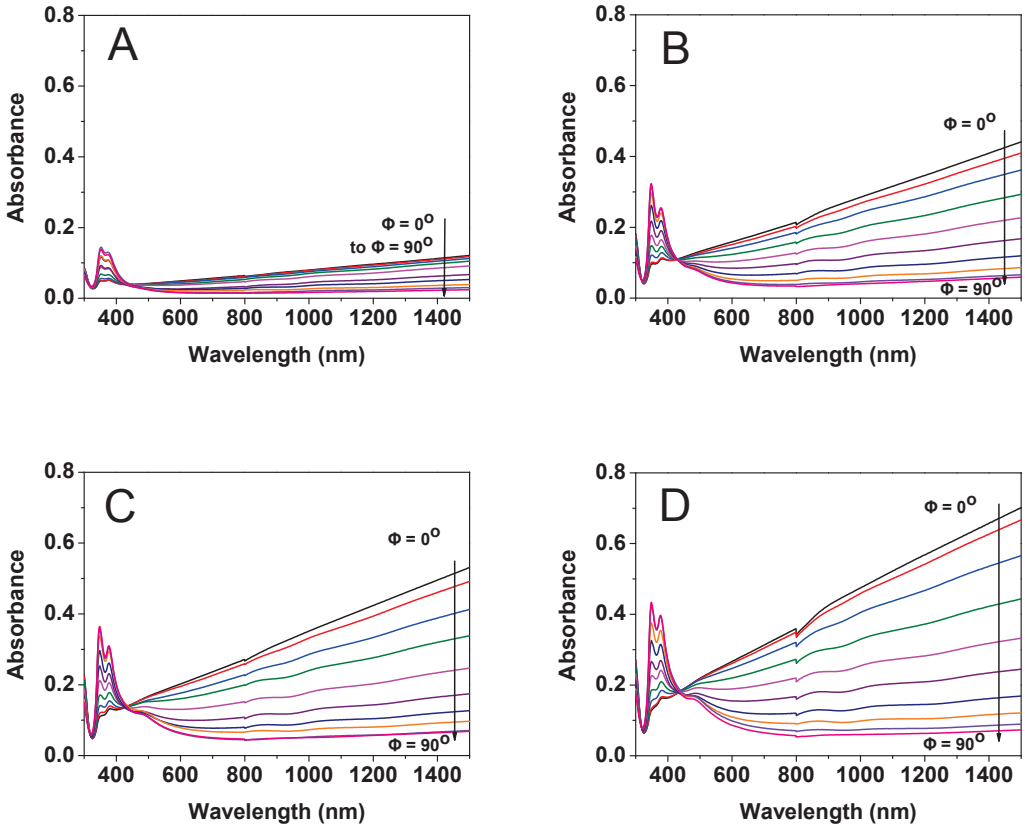

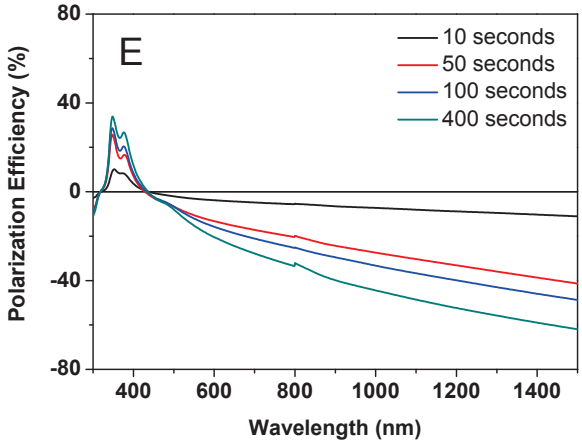

Figure 73. Polarized UV-Vis-NIR spectra of oriented thin film deposited with silver nanowire with different spraying time. (A) 10 seconds; (B) 50 seconds; (C) 100 seconds; (D) 400 seconds. (E) Polarization efficiency as function of spraying time.

3.3 Alignment of silver nanowires in multilayers

In the previous part, the influences of the different "grazing-incidence spraying" parameters on the alignment of silver nanowires in monolayer were investigated. SEM is used to show the morphology of the layer and the silver nanowire orientation direction. The optimal spraying parameters were defined. For an optimal orientation of the nanowires in the monolayer, an air flow of 30 L/min and a liquid downstream distance of 1 cm are to be used for the film preparation.

Here, the best parameters for building multilayer oriented thin films are investigated. Anionical silver nanowires are assembled with positively charged polyelectrolytes such as PAH and PEI. These LbL oriented thin films are then characterized with SEM for the morphology.

Polarized UV will be used to measure the UV-curve changes as function of the rotation angle of the polarizer. The four-point method will be used to measure the electrical transport properties of multilayer oriented thin films from different direction. These two methods are mainly used to characterize the anisotropic property of the multilayer thin film.

3.3.1 Alignment of silver nanowires in two layers

Two layers of silver nanowires were oriented by grazing-incidence spraying with the air flow of 30 L/min and flowing distance of 1 cm. First film was prepared like this, silver nanowires were sprayed on the pure silicon wafer, then the second layer of silver nanowire were sprayed perpendicularly on the first layer directly. From the SEM picture (Figure 74), as expected that the second layer can not stick to the first layer very well, and also the first layer was also destroyed a little bit because of the air flow, which means that a polyelectrolyte is necessary for increasing the adhesion between silver nanowire and the silicon wafer or between neighboring layers of silver nanowires.

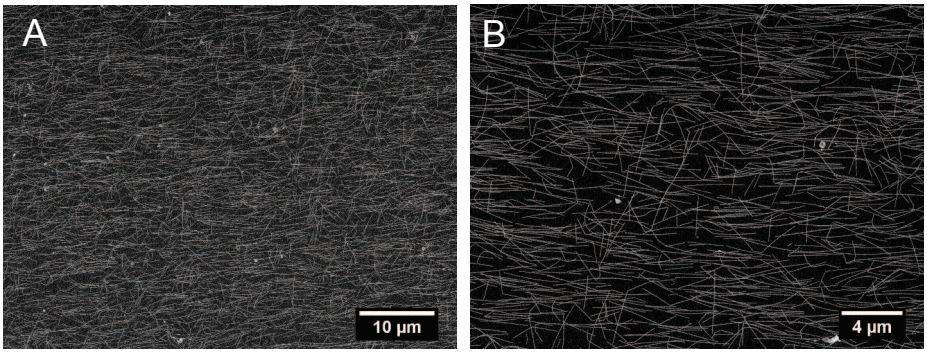

Figure 74. (A) SEM image of two layers silver nanowires deposited on silicon wafer without electrolytes; (B) Magnified SEM image of (A).

Second film was prepared using PEI as the first layer for the film growth: the initial silver nanowires were sprayed on PEI-coated silicon wafer, second layer was sprayed perpendicularly on it. From the SEM (Figure 75), we can get that the first layer has not been influenced by the second layer, the second layer also can not stick to the second layer.

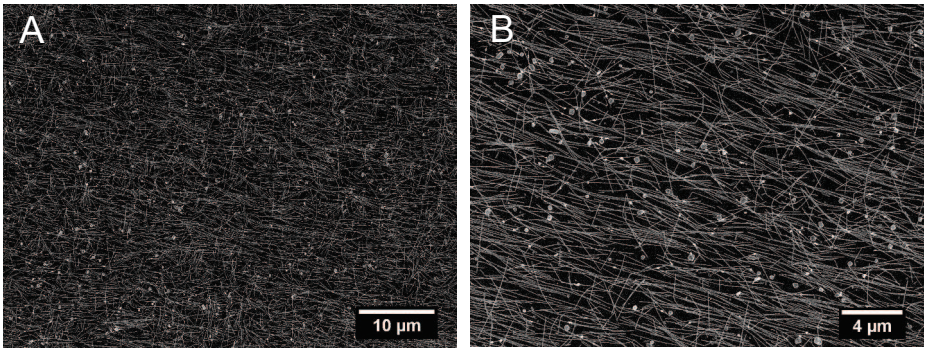

Figure 75. (A) SEM image: first layer of silver nanowire deposited on PEI-coated electrolytes, second layer of silver nanowire coated on it vertically; (B) Magnified SEM image of (A).

For the next experiments, we tried to keep some special distance between these two neighbored silver nanowire layers, we found this condition can be achieved by inserting some polyelectrolyte pairs. The polyelectrolyte was coated by orthogonally spraying with the "air-boy", (PSS/PAH) was used as the electrolytes pair, for one layer pair of PSS/PAH, the thickness is about 3 nm, the distance between every neighbored nanowire layer can be tuned very easily by varying the numbers of PSS/PAH layer pair. For the third film, PAH was coated directly on the first layer of AgNW, then PSS and PAH were coated alternatively for the LbL film growth, $PAH(PSS/PAH)_5$ was coated on the first layer of the silver nanowire, the last layer of polyelectrolyte was positively-charged PAH, which is used to stick the second layer of AgNW. The SEM (Figure 76) shows that the density of second silver nanowire layer is very low, which is mainly due to the interaction between the PAH and silver nanowire is not strong enough for silver nanowire deposition.

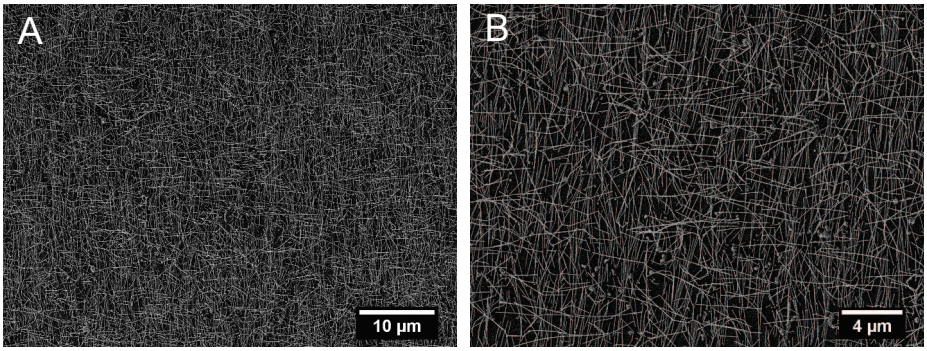

Figure 76. (A) SEM image of PEI/AgNW/PAH(PSS/PAH)$_5$/AgNW, the second layer of AgNW was prayed vertically from the first layer. (B) Magnified SEM image of (A).

For the forth sample, silver nanowire was sprayed on PEI coated silicon wafer by grazing incidence spraying, PEI was coated on the first layer of silver nanowire, also PSS and PAH was sprayed alternatively on PEI for the film growth, final layer pair was PSS/PEI, then the second layer of silver nanowire was sprayed vertically from the first silver nanowire direction. SEM picture show that the orientation of the second layer was successful, also the density of the second layer nanowire was almost the same as the first layer (Figure 77). So in the following experiment, PEI(PSS/PAH)$_n$PSS/PEI was used as a model for building the multilayers oriented silver nanowire films.

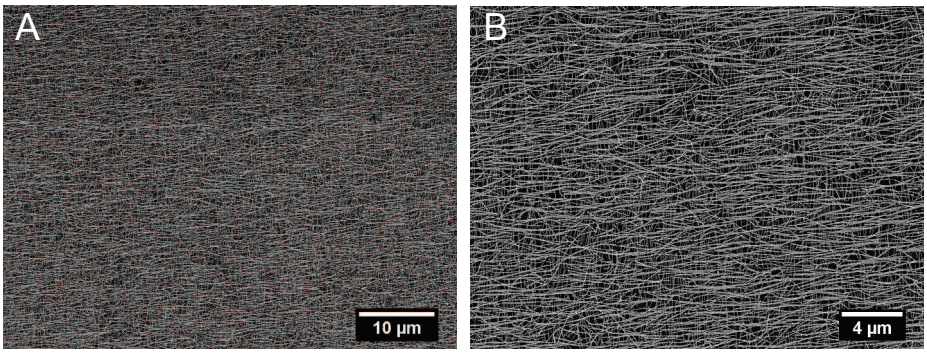

Figure 77. (A) SEM image of PEI/AgNW/PEI(PSS/PAH)$_5$PSS/PEI/AgNW, the second layer of AgNW was prayed vertically from the first layer. (B) Magnified SEM image of (A).

The following scheme describes the method to fabricate the multilayer oriented AgNW thin films. The alignment direction of the silver nanowire is determined by the spraying direction, the alignment of silver nanowire can be easily adjusted by rotating the substrate. Also, the distance between every neighbored silver nanowire layers can be adjusted very easily. Therefore, multilayered and three-dimensional structure in which each layer has same or different alignment direction can be fabricated simply by controlling the orientation and position of the receiving substrate.

3.3.2 Layer-by-Layer assembly of non-oriented silver nanowire in multilayers

PEI is generally used as the first layer and the neighboring layer of silver nanowire in the preparation of LbL assembled films because of its very good adhesive properties. It allows the formation of a very homogeneous and acts as a good promoter layer. In this section, the LbL assembled films of PEI and AgNW were prepared using two LbL preparation methods. The different steps in the preparation methods are described in the materials method chapter. The solution pH, concentration are kept constant.

The first methd was LbL assembly of PEI and AgNW by dipping, it was found that the silver nanowire formed precipitation after 3 LbL steps, this was very strange because we rinsed the substrate for 3 × 3 mins with ultrapure water after each dipping step, it maybe because some PEI came out from the film and formed the complex with silver nanowire.

The second method was LbL assembly of silver nanwire by orthoganal spraying using the spraying nozzle, the receiving substrate was vertical to the spraying direction. The air flow was set at 15 L/min and the liquid flow was set 1 mL/min. The polyelectrolyte such PEI, PSS and PAH were orthoganal sprayed with the “air-boy” bottle. The first layer of AgNW was orthogonal sprayed on PEI coated quartz slide

directly, then PEI/(PSS/PAH)$_5$PSS/PEI multilayers were coated on the first layer of AgNW, followed by depositing of the second layer of AgNW. Four layers of AgNW were incoporated in the LbL film, PEI/AgNW[/PEI(PSS/PAH)$_5$PSS/PEI/AgNW]$_3$. Figure 78A shows the polarized UV-Vis-NIR sprectra of the LbL assembled film by orthogonal spraying from 0 degree to 360 degree, it can be seen that there was still some polarization of the thin film, which means that the silver nanowire in the film was oriented to some extent. This result can be explaned like this: first may be the spraying direction was not exactly vertical to the receiving substrate; second when the AgNW suspension arrived at the center of the receiving substrate, the suspension flowed to the edge from different direction, so there was a shear force induced, which made the orientation of the silver nanowires.

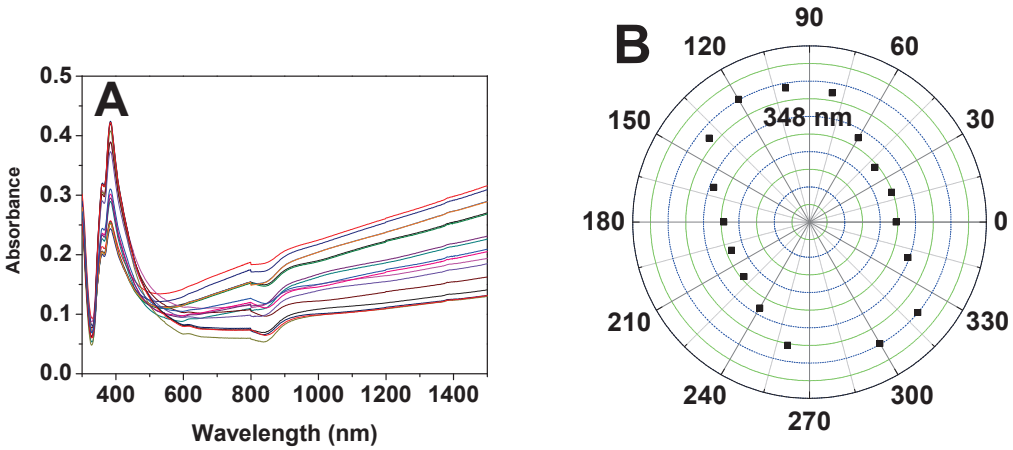

Figure 78. (A) Polarized UV-Vis-NIR spectra of non-oriented thin film measured from 0^o to 360^o; (B) Polar plot of absorbance at 348 nm as function of rotation angle.

3.3.3 Principle for building of multilayered thin films of silver nanowires

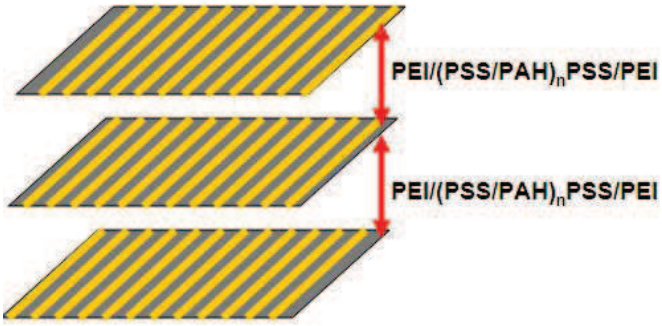

Scheme 2. Principle of fabricating LbL assembled silver nanowire multilayers (The red arrow indicates the spaccing and the spacing depends on n value).

The multilayer films of PEI/AgNW/[PEI(PSS/PAH)$_n$PSS/PEI/AgNW]$_{m-1}$ were prepared by a LbL method and grazing-incidence sprayed of AgNW and orthogonal sprayed of polyelectrolytes between every two neighbored AgNW layers. PEI helps to promote the adhesion AgNW on the film and to prevent delamination.

Multilayer buildup of the film was monitored by side-view of the SEM in the case of deposition on silicon wafers, and UV-vis spectroscopy in the case of deposition on quartz slides. Figure 79A shows representative scanning electron microscopy (SEM) side-view image of PEI/AgNW/[PEI(PSS/PAH)$_5$PSS/PEI/AgNW]$_{m-1}$ (m = 2, 4, 6, 8) film prepared on silica wafers which was carefully broken after film deposition and investigated. Silver nanowires were aligned in the same direction. From the images, the films are quite homogeneous and relatively dense. Figure 79B shows the UV spectra as function of layers of AgNW, the UV was measured after depositing every layer of AgNW (from 1 layer to 8 layers). Figure 79C show that film growth in linear growth at these conditions with a roughly increment of 50 nm per layer of silver nanowire (thickness of AgNW plus thickness of polymer) and an absorbance increment of 0.11 per layer pair (at 349 nm).

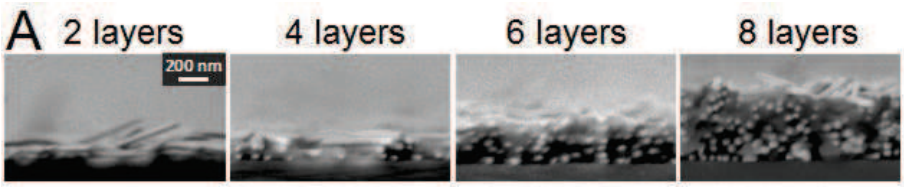

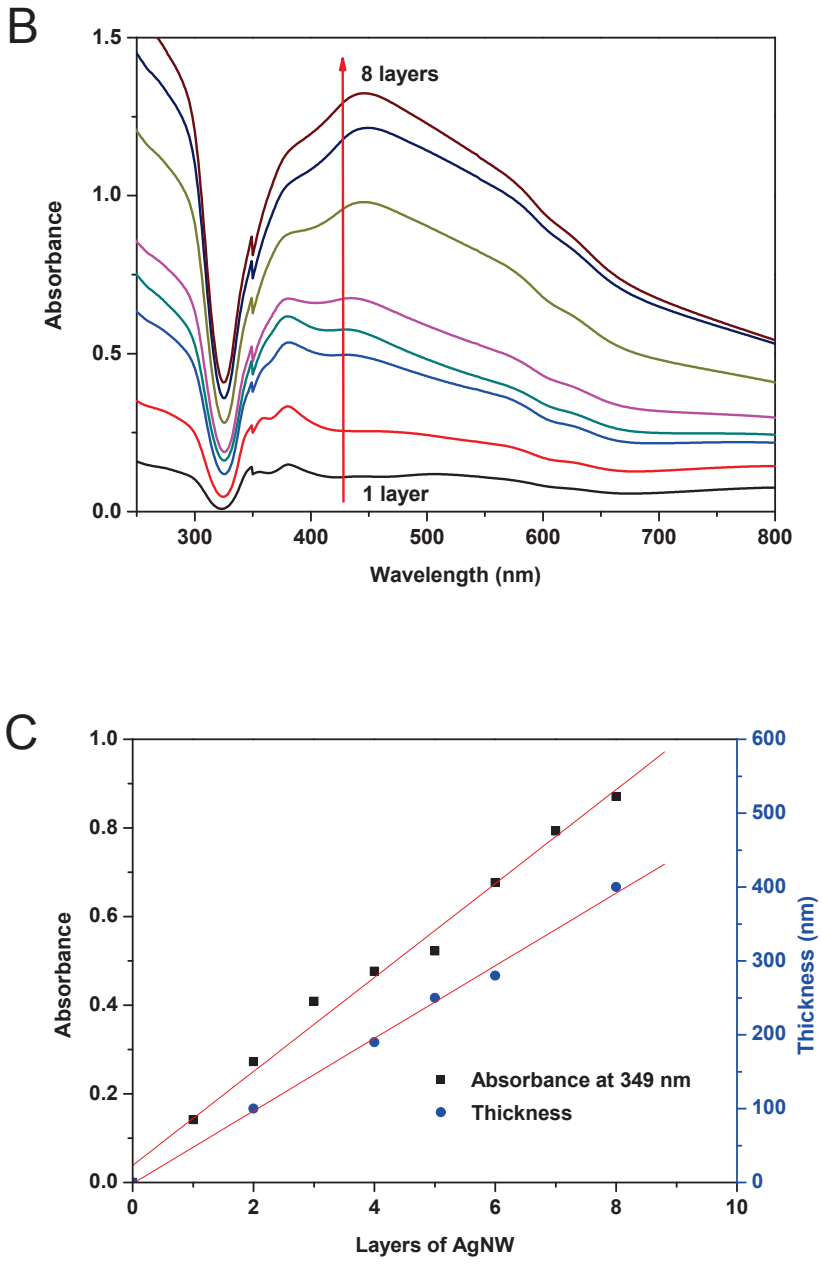

Figure 79. (A) Side-view SEM images of oriented thin films composed m = 2, 4, 6, 8 layers of silver nanowires; (B) Unpolarized UV spectra of thin films of different layers of AgNW; (C) Absorbance at 349 nm and thickness measured from side-view SEM as function of layers of silver nanowires.

3.3.4 Optical properties multilayered thin films of silver nanowires

3.3.4.1 Influence of layers of silver nanowire on the optical properties

The multilayers of silver nanowire films were prepared, the AgNW was sprayed in the same direction for 200 seconds by GIS and washed with water for 100 seconds and the polymers were sprayed for 10 seconds and washed for 10 seconds with the "air boy". These films are named PEI/AgNW/$[PEI(PSS/PAH)_5/PSS/PEI/AgNW]_{m-1}$ (m = 2, 3, 4). The film thicknesses are about 100 nm, 150 nm and 200 nm for m = 2, 3, 4, respectively. The films were characterized with the polarized UV, the polarizer was rotated from 0 degree to 90 degree. Similarly to the oriented monolayer discussed above, the optical response of oriented multilayer thin films is polarization-dependent. The polarized UV spectra are shown in Figure 80. The behavior of multilayer films is similar to the monolayer: the absorbance in the NIR range is high when the longitudinal SPR band is excited by shining light linearly polarized in the direction of the nanowire long axis, and the absorbance in the near-UV range is high when the transverse SPR bands are excited by using light polarized in the direction perpendicular to the orientation direction. Obviously, as the silver nanowire layer increased, the absorbance increased. When measuring at 70 degree to 90 degree, as the AgNW layers increased, the positions of the two peaks ~ 360 nm (peak 1) and ~ 380 nm (peak 2) don't change too much, however the difference of the absorbance between these two peaks becomes more obvious, the Abs ratio of peak 1/peak 2 are 0.973, 0.903, 0.879 for 2, 3, 4 layers of silver nanowire directly (Table 1), this means that the peak at ~ 360 nm decreases but the peak ~ 380 nm increases.

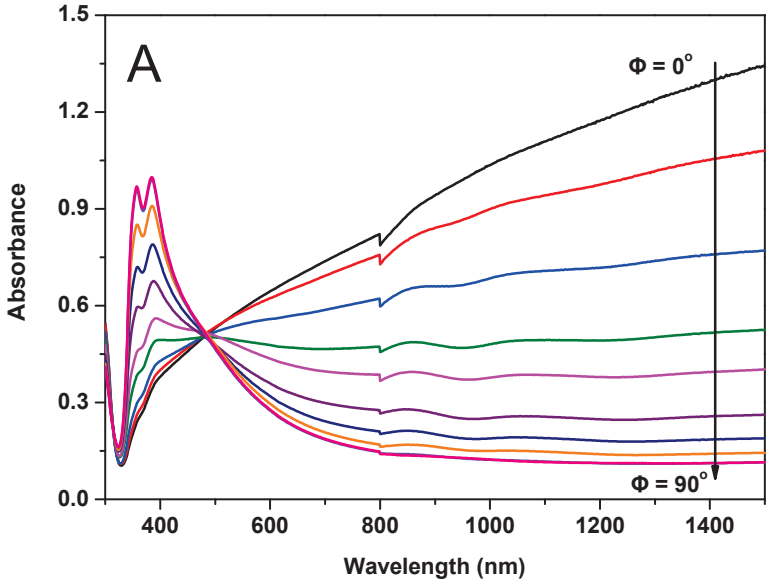
A
Φ = 0°
Φ = 90°
Absorbance
Wavelength (nm)
1.5
1.2
0.9
0.6
0.3
0.0
400
600
800
1000
1200
1400

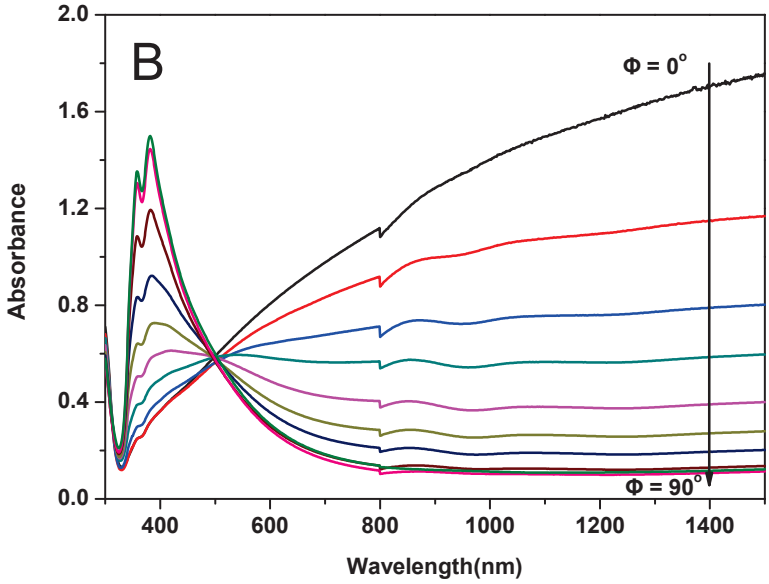
B
Φ = 0°
Φ = 90°
Absorbance
Wavelength(nm)
2.0
1.6
1.2
0.8
0.4
0.0
400
600
800
1000
1200
1400

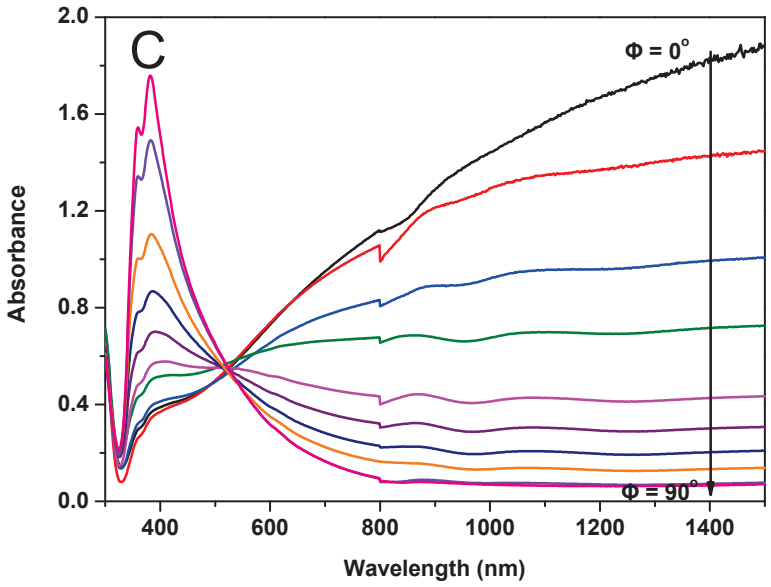

Figure 80. Polarized UV spectra of oriented thin films composed m = 2, 3, 4 layers of silver nanowires. (A) m = 2; (B) m = 3; (C) m = 4.

Table 1. Ratio of Abs $_{peak\ 1}$/Abs $_{peak\ 2}$ as function of layers of silver nanowire. These values are obtained from the polarized UV of different samples. (**Figure 72** and **Figure 80**)

Layers of silver nanowire	Ratio of Abs $_{peak\ 1}$/Abs $_{peak\ 2}$
1	1.08
2	0.973
3	0.903
4	0.879

We also take the UV curve at 0 degree and 90 degree (Figure 81A) to calculate the polarization efficiency according to **equation 16**. As the silver nanowire aligned in multilayers, the polarization efficiency is obviously higher than the monolayer silver nanowire film. Furthermore, the polarization efficiency increases strongly with the

number of deposited silver nanowire layers (Figure 81B). The polarization efficiency is equal to 31% at 347 nm and 57% at 1500 nm for the monolayer sample, and reaches respectively 92% and 97% for the 4-layer samples. This effect can be explained by the fact that as the number of layers increases, more and more oriented plasmonic material is coated and the polarization efficiency of the thin film increases accordingly. The polarization efficiency is not much increased when comparing the films with n = 3 and n = 4, which is due to the fact that the polarization efficiency is getting close to its maximum theoretical value of 100%.

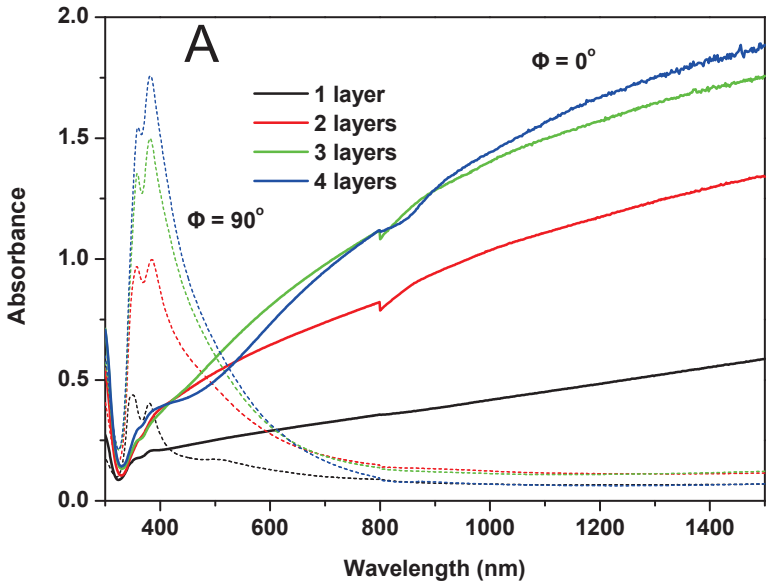

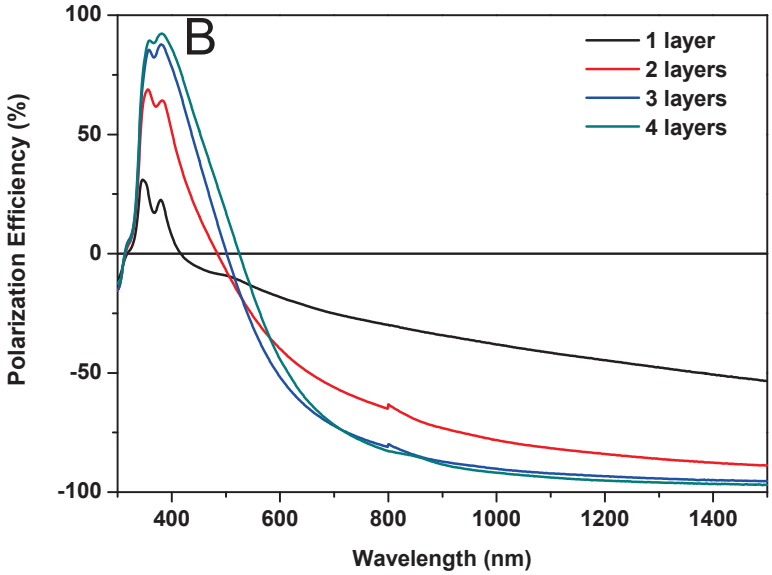

Figure 81. (A) UV spectra for light polarized parallely (full lines) and perpendicularly (dashed lines) to the orientation direction for various layer numbers; (B) Polarization Efficiency for various samples.

3.3.4.2 Influence of spacing between neighbored layers of silver nanowire on the optical properties (this experiment was done with a new batch of AgNW)

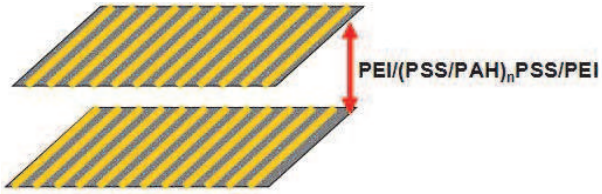

Scheme 3. Schematic representation of two layers of silver nanowires aligned in the same direction. (The red arrow indicates the spaccing and the spacing depends on n value).

In order to investigate the spacing on the optical properties. We prepared the samples with two layers of silver nanowire sprayed in the same direction for 200 seconds, this means the density of the silver nanowire is kept almost consistent. However, the spacing is varied by just changing the layer pairs of PSS/PAH. We prepared a series of

samples named PEI/AgNW/PEI(PSS/PAH)$_n$/PSS/PEI/AgNW (n = 1, 3, 5, 20, 60). These samples were characterized with the polarized UV, with the polarized angle varied from 0 degree to 90 degree. The UV spectra are shown in Figure 82. Figure 82A is the polarized UV of the monolayer of AgNW film. For the near UV range, it shows the typical peaks at ~ 350 nm (peak 1) and ~ 375 nm (peak 2), when the polarizer turned to 90 degree the absorbance at ~ 350 nm is much higher than ~ 375 nm, the ratio of Abs $_{peak\ 1}$/Abs $_{peak\ 2}$ is 1.53.

For two layers of AgNW, as the spacing increased we can see that the shape of the UV curve at polarized angle of 90 degree changed dramatically. As the spacing increased, the peak at ~ 350 nm (peak 1) decreases and the peaks at ~ 380 nm (peak 2) increases. For example, for n = 1, Abs $_{peak\ 1}$/Abs $_{peak\ 2}$ is 1.08. The ratio of Abs $_{peak\ 1}$/Abs $_{peak\ 2}$ are 1.05, 1.06, 0.934, 0.882 for n = 3, 5, 20, 60 respectively (Table 2 and Figure 83). This can be explained like this, maybe the peak at ~350 nm is mainly due to the coupling between these two different layers of silver nanowires, as the spacing increased, the interaction between these two layers decreased, which is reflected in the UV curve as the absorbance at the peak at 350 nm decreased. As the spacing decreased to (PSS/PAH)$_1$, the shape of the UV curve is similar to monolayer of the AgNW thin film.

Also as the spacing between two layers silver nanowires increased, the peak position shifted a little bit, and this two peaks separate from each other. The peak distances are 23 nm, 26 nm, 31 nm, 32 nm, and 36 nm for n = 1, 3, 5, 20, 60 respectively (Table 3 and Figure 84).

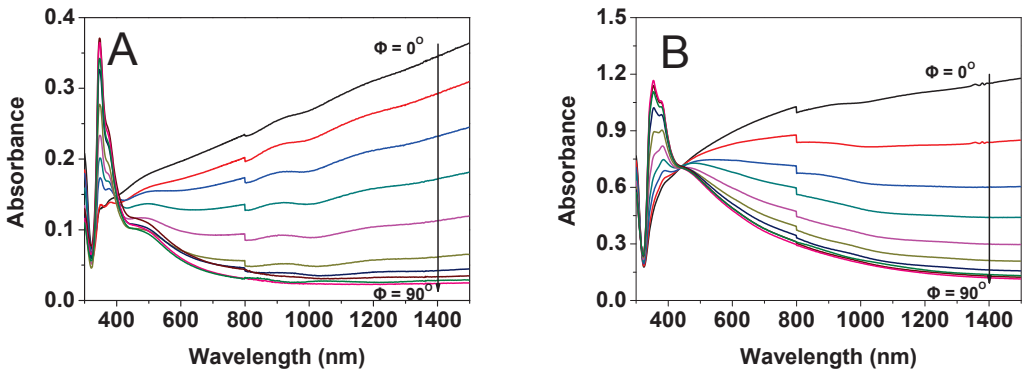

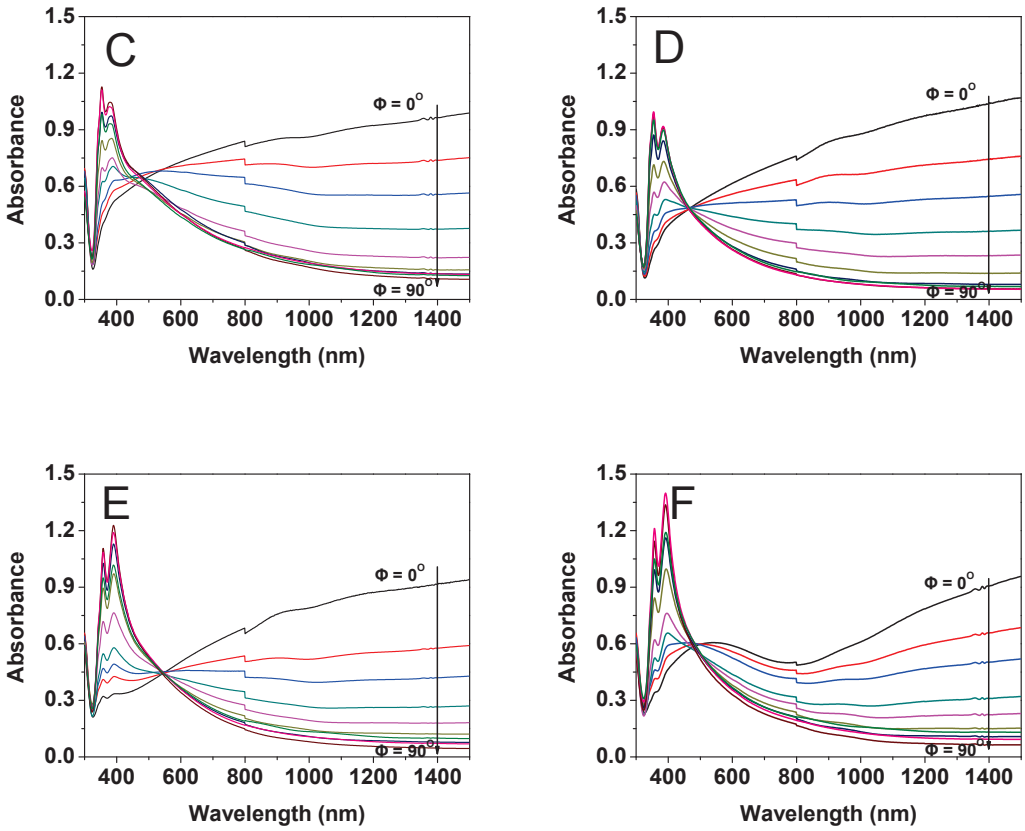

Figure 82. Polarized UV of different samples measured from 0° to 90°. (A) monolayer; (B) n = 1; (C) n = 3; (D) n = 5; (E) n = 20; (F) n = 60

Table 2. Ratio of Abs $_{peak1}$/Abs $_{peak\ 2}$ as function of layers of PSS/PAH. These values are obtained from the polarized UV of different samples. (**Figure 82**)

Spacing: (PSS/PAH) layer pairs	Ratio of Abs $_{peak\ 1}$/Abs $_{peak\ 2}$
1	1.08
3	1.05
5	1.06
20	0.934
60	0.882

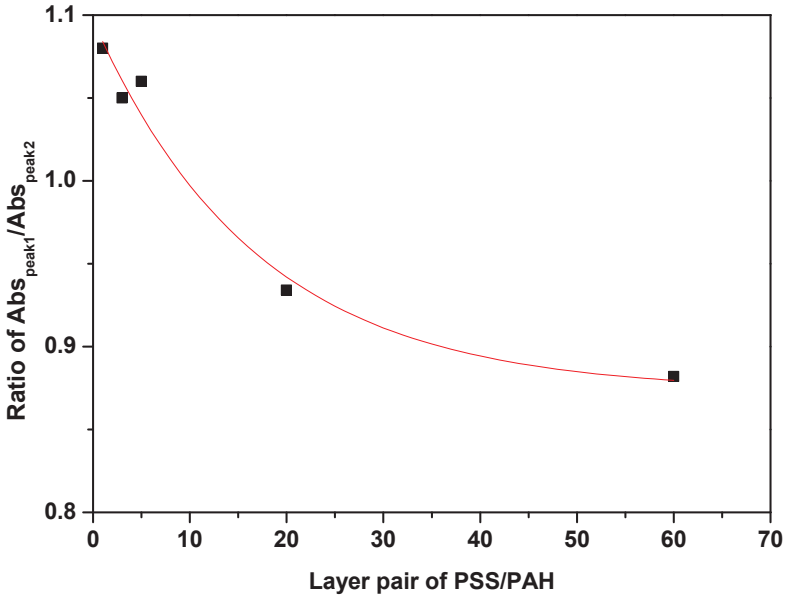

Figure 83. Ratio of Abs $_{peak1}$/Abs $_{peak\ 2}$ as function of layers of PSS/PAH. (The red line just shows a clear eye show, it doesn't have any physical meaning)

Table 3. Peak distance as function of layers of PSS/PAH. These values are obtained from the polarized UV of different samples. (**Figure 82**)

Spacing: (PSS/PAH) layer pairs	Peak distance (nm)
1	23
3	26
5	31
20	32
60	36

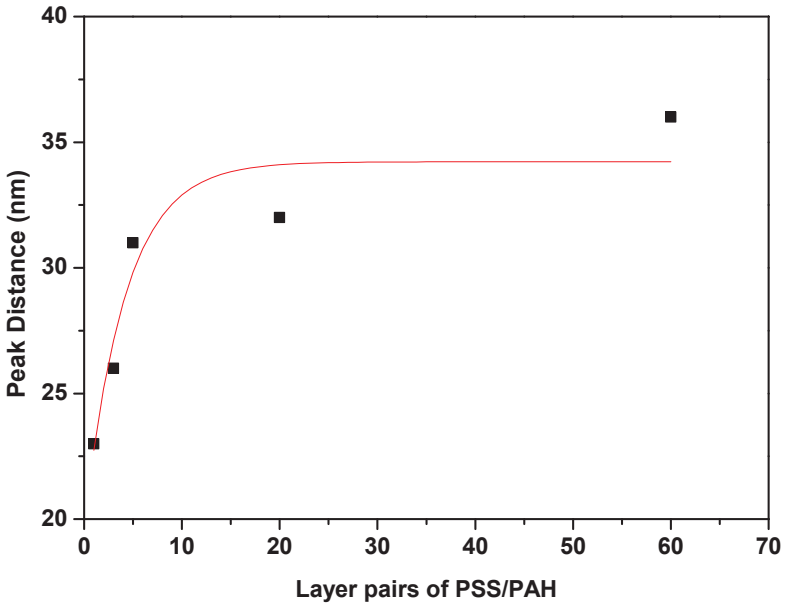

Figure 84. Peak distance as function of layers of PSS/PAH. (The red line just shows a clear eye show, it doesn't have any physical meaning)

3.3.5 Electrical properties of multilayers oriented thin films of silver nanowires on quartz

If the silver nanowires are coated randomly on the substrate, it should showed the same conductivity for all the directions because of the isotropic properties. However, when the silver nanowires are aligned, the conductivity along the silver nanowire orientation direction should be higher than the vertical direction. We first measured the conductivity of the monolayer film. However, it was impossible to do this measurements because of the conductivity is too low. So 6 layers of silver nanowire PEI/AgNW/$[PEI(PSS/PAH)_5PSS/PEI/AgNW]_5$ was prepared. Figure 85A and B show the top-view SEM of PEI/AgNW/$[PEI/(PSS/PAH)_5/PSS/PEI/AgNW]_{m-1}$ (A: m = 5; B: m = 3).

To determine the effect of AgNW orientation on macroscopic electrical transport, I/V curves were measured on PEI/AgNW/$[PEI(PSS/PAH)_5PSS/PEI/AgNW]_5$ film with the four-point method in two directions: 0^o and 90^o with respect to the aligned

direction. For instance, when measuring the resistance at 0° for the aligned film, the electrical probes were aligned in parallel to the orientation direction. Oppositely, for the measurement at 90°, the probes aligned vertical to the orientation direction. Figure 80C shows the conductivity measured in these two directions. When measured in parallel to the aligned direction (0°), it displayed a sheet resistance of 0.91 $k\Omega\square^{-1}$. However, in the case of 90° to the aligned direction, the resistance is about 10 times higher, 8.15 $k\Omega\square^{-1}$ (Figure 85C). This is because it needs electron transport from wire to wire for conduction, it has more wire-to-wire contacts parallel to the alignment direction and much more gaps perpendicular to the alignment direction.

The conductive properties of the direction 30° and 60° in relate to the silver nanowire orientation direction were also measured. In the case of 30 degree in relate to the silver nanowire orientation direction, the sheet resistance is 2.32 $k\Omega\square^{-1}$. For the sample 60 degree to the orientation direction, the sheet resistance increased to 3.14 $k\Omega\square^{-1}$. So the conductivity: 0 degree > 30 degree > 60 degree > 90 degree (Table 4). The anisotropy in electrical response indicated that the alignment direction of the AgNW has a strong effect on the macroscopic electrical properties of the multilayer architectures.

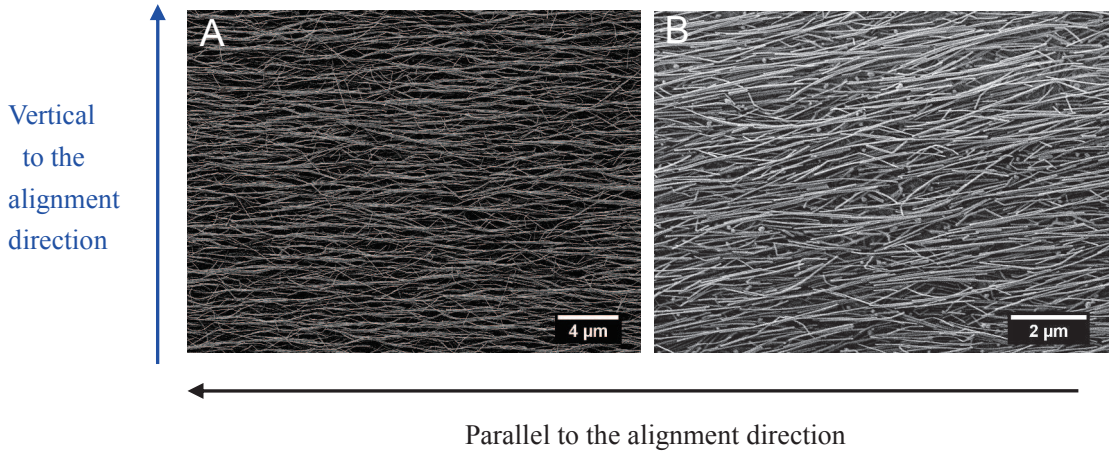

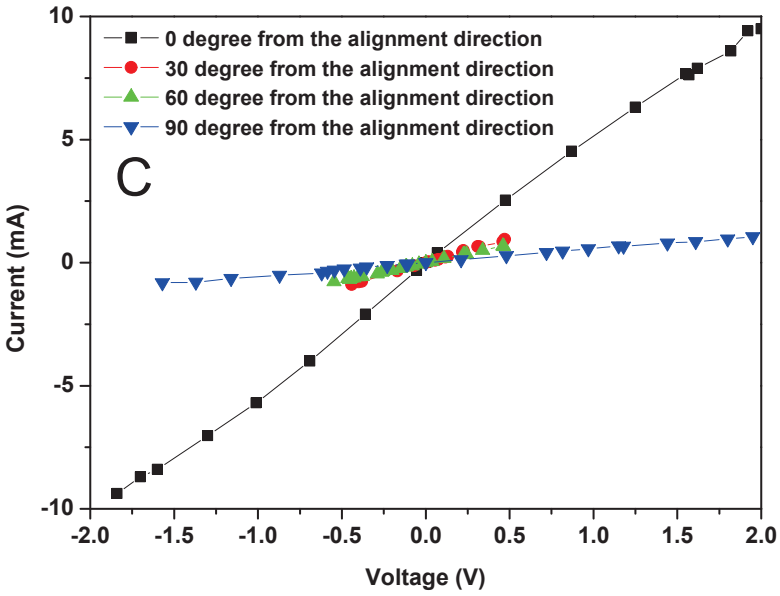

Figure 85. Top-view SEM images of PEI/AgNW/[PEI(PSS/PAH)$_5$PSS/PEI/AgNW]$_4$ (A) and PEI/AgNW/[PEI(PSS/PAH)$_5$PSS/PEI/AgNW]$_2$ (B); (C) I-V curve of PEI/AgNW/[PEI(PSS/PAH)$_5$PSS/PEI/AgNW]$_5$ on quartz measured from 0 degree to 90 degree in related to the alignment direction.

Table 4. Sheet resistances measured from different directions in relate to the alignment direction. These values are calculated from **Figure 85.**

Different directions in relate to the alignment direction	Sheet resistance (kΩ/sq)
0 degree	0.91
30 degree	2.32
60 degree	3.14
90 degree	8.15

3.3.6 Various novel 3D structures prepared and characterized by SEM

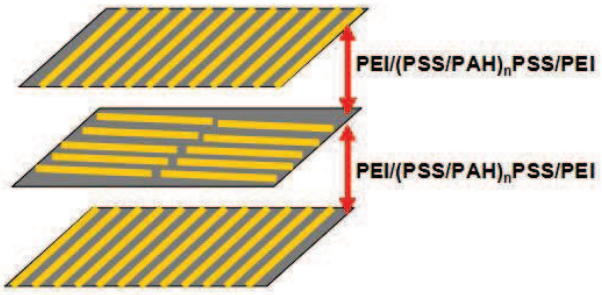

Scheme 4. Schematic representation of LbL assembled silver nanowires from different direction. (The red arrow indicates the spacing and the spacing depends on n value).

The advantage of GIS is that it allows us to assemble nanowires in large area. Also, the alignment direction of the NWs in controllable by changing the spraying direction. Figure 86 is the SEM pictures of two layers silver nanowire sprayed perpendicularly with each other, with the distance of $(PSS/PAH)_{10}$ and $(PSS/PAH)_{15}$ respectively. From the SEM, it can be concluded that, the distance between the neighbored silver nanowire layers influence the alignment and the density of the second silver nanowire layer to some extent, this might be due to that as the distance increased, the films became thicker, which has the influence on the silver nanowire sticking to the PEI. And we found that, as the distance increased, the first layer of AgNW become less obviously in the top-view SEM image.

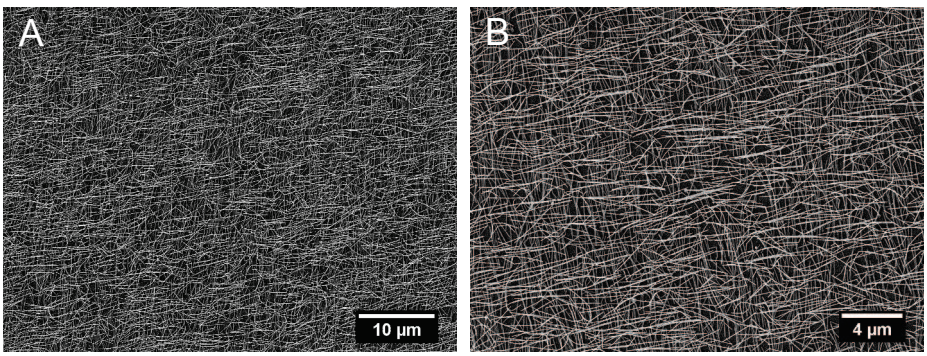

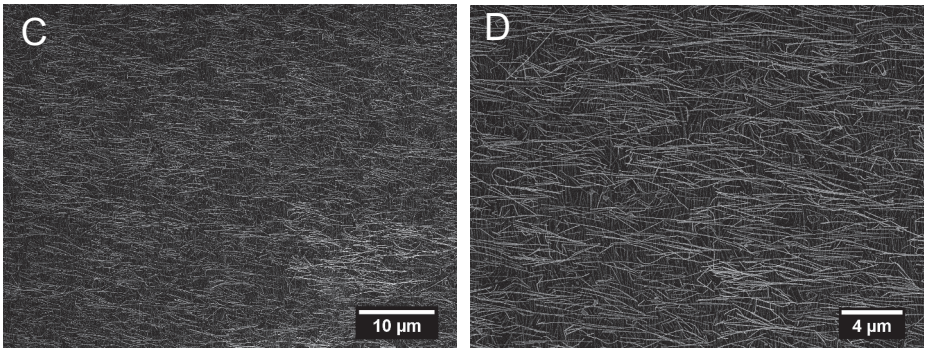

Figure 86. (A) SEM images of PEI/AgNW/PEI(PSS/PAH)$_{10}$PSS/PEI/AgNW; (B) Enlargement of (A); (C) SEM images of PEI/AgNW/PEI(PSS/PAH)$_{15}$PSS/PEI/AgNW; (D) Enlargement of (C).

Three layers of silver nanowires with different orientation direction were also fabricated. Figure 87 shows the three layers of silver nanowires sprayed from different direction with the distance of (PSS/PAH)$_5$, (PSS/PAH)$_{10}$, (PSS/PAH)$_{15}$, the twist angle is 60^o between every neighbored silver nanowires, it can also be seem that the distance also influence the density of following layer silver nanowire density. We can even build more layers of nanowire structures by combing the Layer-by-Layer method and grazing-incidence spraying. Figure 88 is the top view and the side view of 6 layers of silver nanowires sprayed on silicon wafer from different direction, the twisted angle is 30^o. As the layers of silver nanowire > 3, this kind of helical structures can be considered as chiral nanoassemblies. Chiral nanoassemblies usually defined as Left-handed and Right-handed. Figure 89 shows two layers of silver nanowires aligned perpendicularly on glass slide, this kind of structure can be considered as neutral sample in the chiral plasmonic systems, since its posses the same effect from the left and right direction.

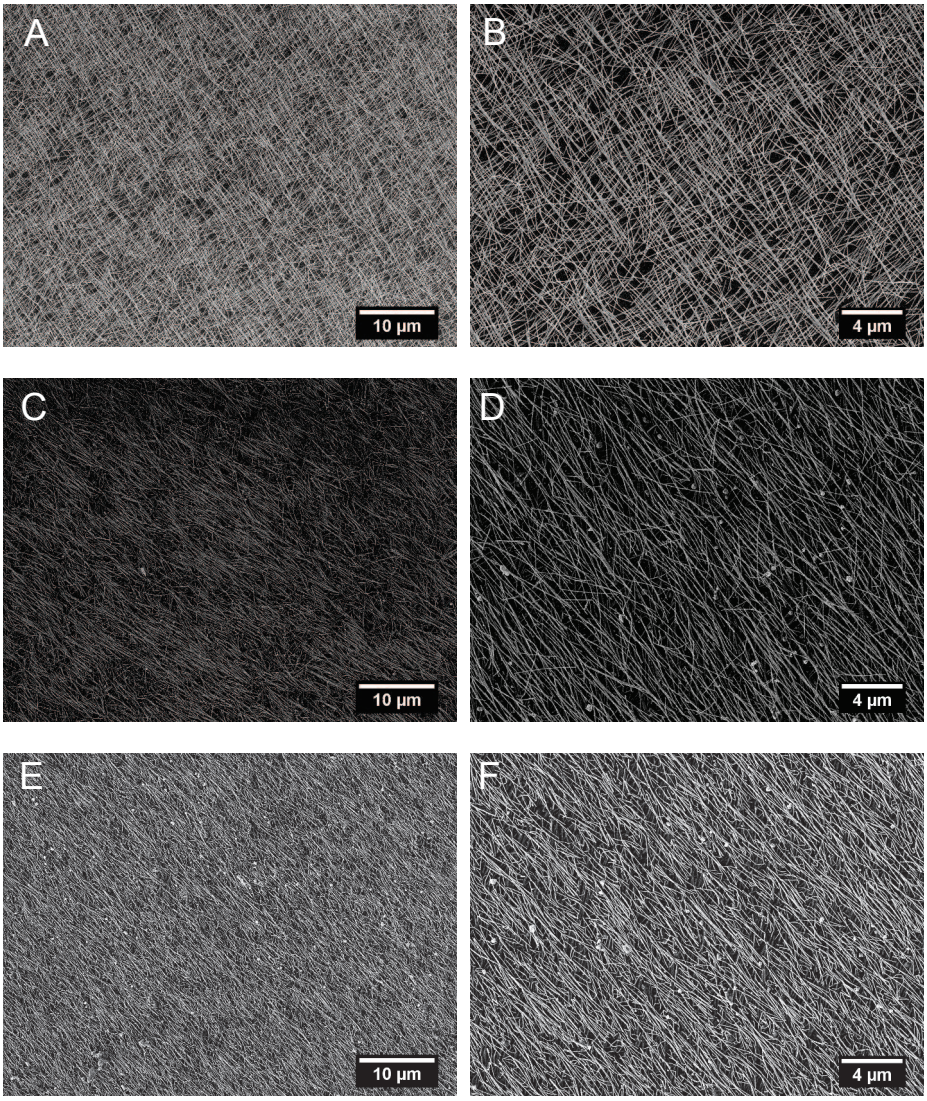

Figure 87. (A) SEM images of PEI/AgNW/[PEI(PSS/PAH)$_5$PSS/PEI/AgNW]$_2$; (B) Enlargement of (A); (C) SEM images of PEI/AgNW/[PEI(PSS/PAH)$_{10}$PSS/PEI/AgNW]$_2$; (D) Enlargement of (C). (E) SEM images of PEI/AgNW/[PEI(PSS/PAH)$_{15}$PSS/PEI/AgNW]$_2$; (F) Enlargement of (E)

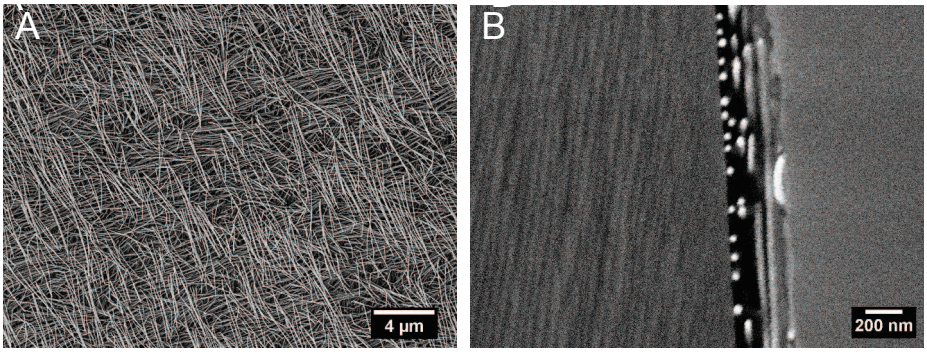

Figure 88. (A) Top view (A) and Side view (B) SEM images of PEI/AgNW/[PEI(PSS/PAH)$_5$PSS/PEI/AgNW]$_5$

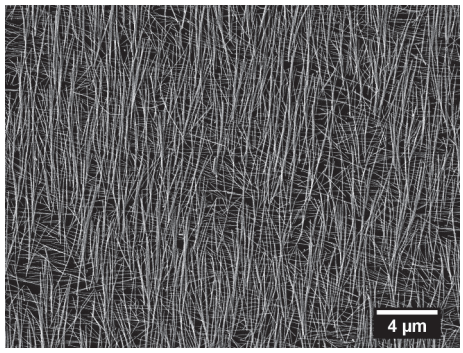

Figure 89. Top-view SEM image of PEI/AgNW/PEI(PSS/PAH)$_4$PSS/PEI/AgNW

3.4 Chiral plasmonic nanostructures based on multilayers of helically twisted silver nanowires

Chiral plasmonic systems have recently attracted substantial interest among materials scientists since they provide the opportunity to achieve strong optical circular dichroism (CD) activity over a broad spectral range[5-7]. Materials derived from these systems are expected to open up the field of metamaterials with nonlinear optics[8], catalyst[9] and nanolevitation[10] properties. Promising applications of man-made chiroptical materials with controlled right- (R-) and left- (L-) handedness also include biosensors[11], negative refractive index media[12], detectors for circularly polarized light[13] and drug development[14].

In this thesis, we present a new chiroptical plasmonic material and a simply, low-cost strategy for its fabrication. The approach utilizes the incorporation of aligned silver nanowire (NW) into a Layer-by-Layer polymeric film. This method and the materials offer the following potentially useful features: (i) the chiral optical activity of the

plasmonic NWs is obviously stronger than that chiral nanostructures prepared with other techniques; (ii) parallel alignment of the AgNWs, perpendicular to the direction of the left-handed or right-handed helices, yielding of new type of chiral pattern; (iii) the tunability of distance and twisted angle between every adjacent nanowire layers; (iv) very large area of the plasmonic structure; (v) the simplicity of film preparation.

Scheme 5 illustrate the approach to the preparation of chiral plasmonic films, which is based on the Layer-by-Layer assembly and grazing-incidence-spraying. The AgNW was aligned on the PEI-coated substrate with the grazing-incidence spraying, then PSS/PAH polyelectrolyte layer pairs were deposited with orthogonal spraying using the Air-Boy spraying bottles for 10 seconds, each polyelectrolyte deposition was followed by rinsing with mili-Q water for 10 seconds, the thickness for one layer pair of PSS/PAH is about 3 nm. A multilayer of PEI/$(PSS/PAH)_n$/PSS/PEI was coated on PEI/AgNW, followed by spraying of the subsequent layer of AgNW with special twisted-angle. To keep the nanosystem symmetric, the twisted angles are fixed to 60° and 45° between neighboring AgNW layer for 3-layer and 4-layer silver nanowire chiral plasmonic film, respectively. Furthermore, the handedness of the AgNW helices can be reversed by changing the spraying direction of the silver nanowire, for instance, spraying of silver nanowires with angle of -60° will lead to the formation of left-handed C3 chiral plasmon.

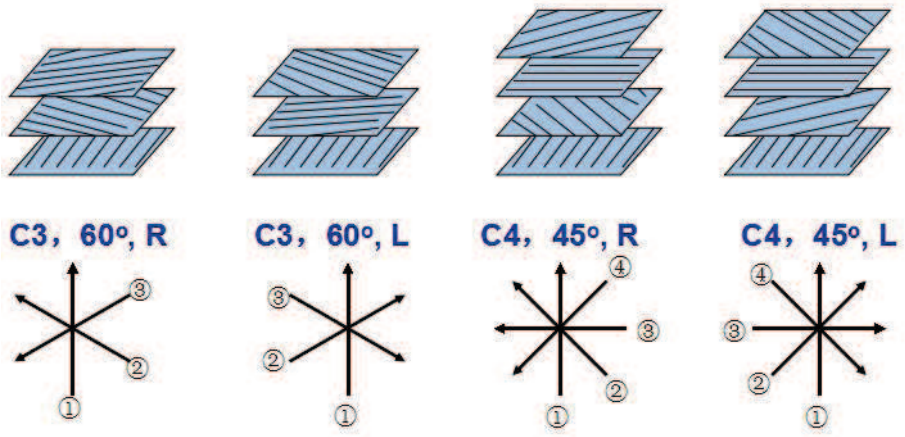

Scheme 5. Schematic illustration of the self-assembly of Right-handed and Left-handed chiral plasmonic structures.

Samples list

HH 3-69 Three layers of silver nanowires (C3) (Right-handed) Spacing: ~ 15 nm

PEI/AgNW/[PEI(PSS/PAH)$_5$PSS/PEI/AgNW]$_2$ Twisted angle: 60°

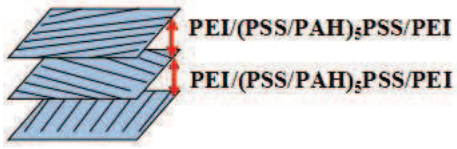

HH 3-72 Three layers of silver nanowires (C3) (Left-handed) Spacing: ~ 15 nm

PEI/AgNW/[PEI(PSS/PAH)$_5$PSS/PEI/AgNW]$_2$ Twisted angle: 60°

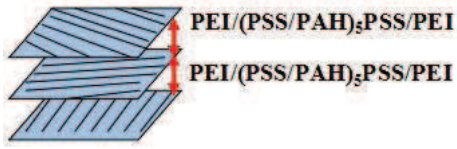

HH 3-33 Four layers of silver nanowires (C4) (Right-handed) Spacing: ~ 15 nm

PEI/AgNW/[PEI(PSS/PAH)$_5$PSS/PEI/AgNW]$_3$ Twisted angle: 45°

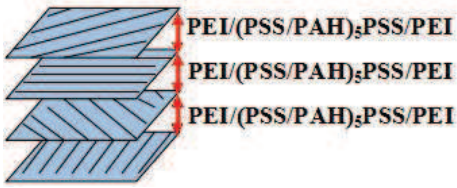

HH 3-88 Four layers of silver nanowires (C4) (Left-handed) Spacing: ~ 15 nm

PEI/AgNW/[PEI(PSS/PAH)$_5$PSS/PEI/AgNW]$_3$ Twisted angle: 45°

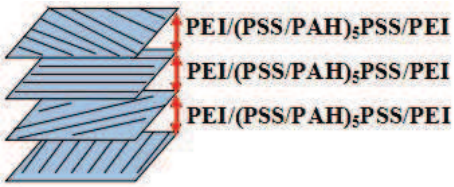

HH 3-84 Four layers of silver nanowires (C4) (Right-handed) Spacing: ~ 30 nm

PEI/AgNW/[PEI(PSS/PAH)$_{10}$PSS/PEI/AgNW]$_3$ Twisted angle: 45°

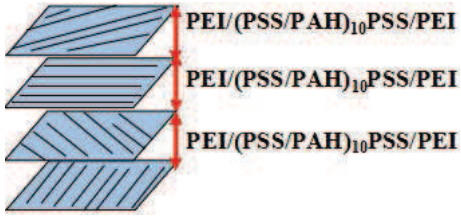

HH 3-86 Four layers of silver nanowires (C4) (Left-handed) Spacing: ~ 30 nm

PEI/AgNW/[PEI(PSS/PAH)$_{10}$PSS/PEI/AgNW]$_3$ Twisted angle: 45°

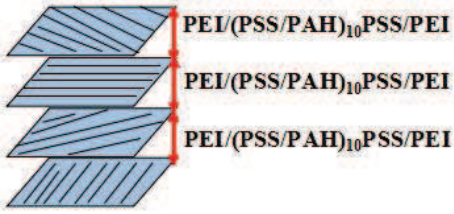

HH 3-73 Four layers of silver nanowires (C4) (Right-handed) Spacing: ~ 60 nm

PEI/AgNW/[PEI(PSS/PAH)$_{20}$PSS/PEI/AgNW]$_3$ Twisted angle: 45°

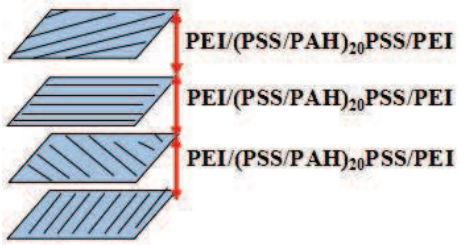

HH 3-71 Four layers of silver nanowires (C4) (Left-handed) Spacing: ~ 60 nm

PEI/AgNW/[PEI(PSS/PAH)$_{20}$PSS/PEI/AgNW]$_3$ Twisted angle: 45°

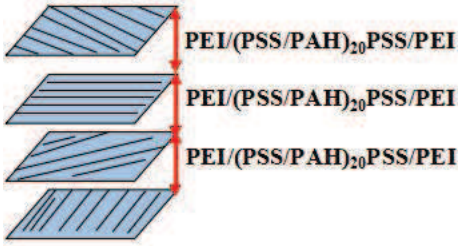

HH 2-127 Three layers of silver nanowires (C3) (Right-handed) Spacing: ~ 15 nm

PEI/AgNW/[PEI(PSS/PAH)$_5$PSS/PEI/AgNW]$_2$ Twisted angle: 60°

Siver nanowire was diluted for 10 times

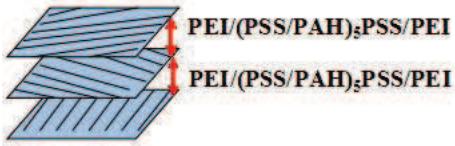

HH 2-130 Three layers of silver nanowires (C3) (Left-handed) Spacing: ~ 15 nm

PEI/AgNW/[PEI(PSS/PAH)$_5$PSS/PEI/AgNW]$_2$ Twisted angle: 60°

Siver nanowire was diluted for 10 times

HH 2-136 Four layers of silver nanowires (C4) (Right-handed) Spacing: ~ 15 nm

PEI/AgNW/[PEI(PSS/PAH)$_5$PSS/PEI/AgNW]$_3$ Twisted angle: 45°

Siver nanowire was diluted for 10 times

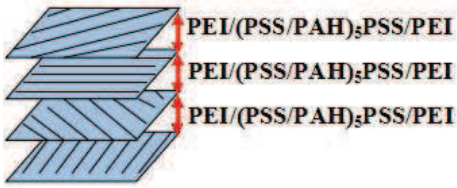

HH 2-137 Four layers of silver nanowires (C4) (Left-handed) Spacing: ~ 15 nm

PEI/AgNW/[PEI(PSS/PAH)$_5$PSS/PEI/AgNW]$_3$ Twisted angle: 45^o

Siver nanowire was diluted for 10 times

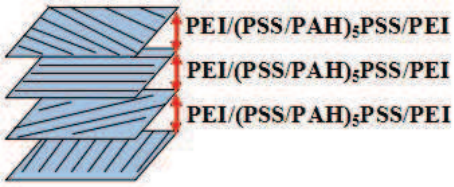

3.4.1 Chiral plasmonic nanostructure built with 3 layers of silver nanowires (C3) (HH 3-69 and HH 3-72)

Silver nanowire, with the zeta-potential of -33.6 mV, can form the Layer-by-Layer film with the positive-charged polyelectrolytes such as PEI, and it was sprayed for 200 seconds for every layer by grazing-incidence spraying. The silver nanowire chiral plasmon was fabricated by combing grazing-incidence spraying with Layer-by-Layer technique. Scanning Electronic Microscopy was used to characterize the assembled three-dimensional AgNW helices. Figure 90A shows the SEM images of C3 right chiral plasmon, which revealed the chiral nematic structure, the density of every layer of silver nanowire is almost the same. Importantly, the handedness of the AgNW helices can be easily fabricated by simply changing the spraying direction of the silver nanowire. When we changed the spraying direction of AgNW oppositely from 60^o to -60^o, a mirrored-symmetric C3 chiral plasmon can be formed (Figure 90B). The C3 chiral plasmon can be noted as PEI/AgNW/[PEI(PSS/PAH)$_5$PSS/PEI/AgNW]$_2$. The

top-view of SEM clearly verified the fabrication of LH- and RH-AgNW helices. It is worth noting that, because of the silver nanowire was sprayed with a strong air flow, a bit AgNW were broken down, but the configuration of LH and RH helices can be discriminated. The different orientation of the AgNWs in the 2D images are highly related to the 3D configurations in LH- and RH-AgNW helices, respectively.

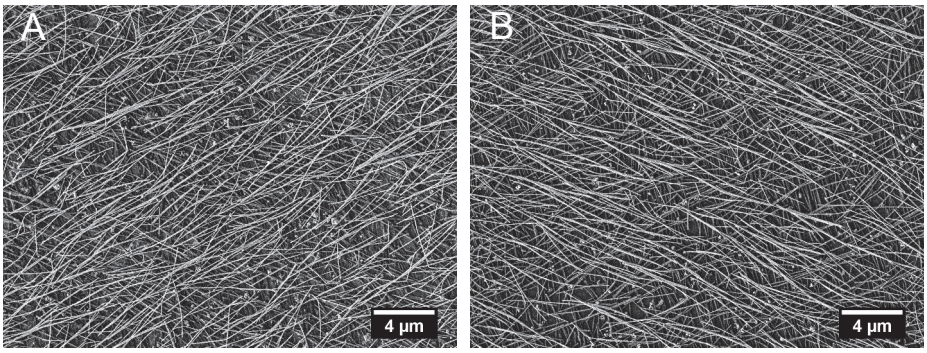

Figure 90. Top-view SEM image of HH 3-69 (A) and HH 3-72 (B)

The optical properties of these plasmonic assemblies were the primary foci of this work. The UV-Vis spectra was also measured with a polarizer set in front of the sample. The polarized UV-Vis-NIR of the RH C3 (HH 3-69) and LH C3 (HH 3-72) chiral plasmonic nanostructure were shown in Figure 91 A and B, the extinction spectrum of silver nanowires displays two peaks at 349 and 376 nm in the UV-Vis region and a broad band starting at ~600 nm and extending towards the near infrared. While the transverse plasmon bands shift in multilayers with uniaxial orientation by coupling between adjacent layers, this is not the case for helically twisted superstructures with identical (or similar) distance between the AgNW layers.

As shown in the previous part of the thesis, both the longitudinal and the transverse mode of the surface plasmon resonance are dependent of the polarization of the incident light in the monolayer oriented thin film. However, when the nanowires are oriented into three dimensional chiral plasmonic structures, the optical response of the film becomes polarization-independent. The extinction was measured as function of the angle Φ between the incident light beam polarization plane and the orientation

direction. The spectra have been recorded for polarization directions Φ varying from 0° to 360° with 20° steps. It can be seen that the absorbance from the UV region to the NIR does not change too much for the whole turn because it is symmetric for every layer of AgNW and every layer has almost the same nanoparticle density. The absorbance at 1500 nm is given in a polar plot as function of the polarization angle Φ in Figure 91 C, it has an circular shape for the whole turn. For RH C3 (HH 3-69) and LH C3 (HH 3-72), the absorbances from UV range to NIR range are almost the same, which indicates the same nanowire density in both of these two samples.

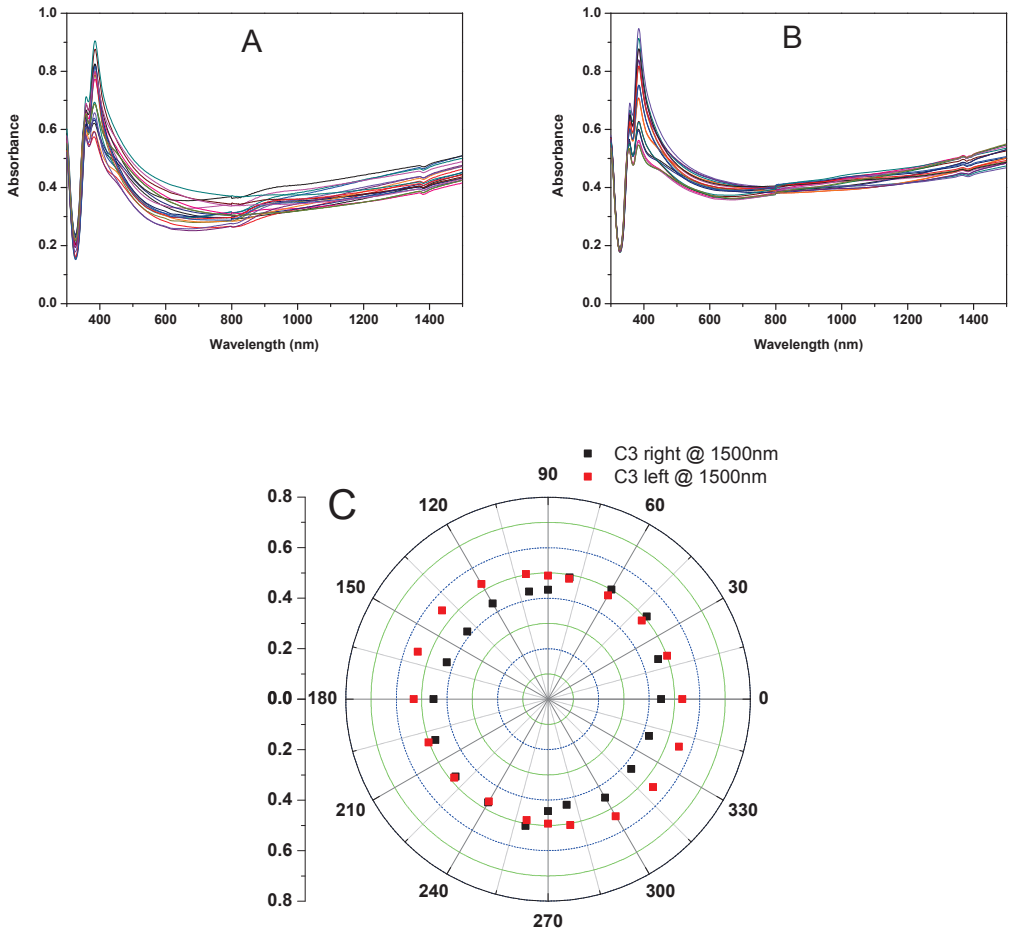

Figure 91. Polarized UV spectra of C3 chiral plasmon thin film as function of rotation angles. (A) right-handed (HH 3-69); (B) left-handed (HH 3-72); (C) Polar plot of absorbance at 1500 nm as function of rotation angles.

The chiral properties of the assembled C3 RH- and LH-AgNW helices were

systematically investigated with CD spectrometer. The CD spectra of the RH and LH C3 chiral plasmon show a clear mirror image relation as depicted in Figure 92A, These responses arise because the helical assembly of the oriented silver nanowires results in coupled plasmon waves along the helical path and causing increased absorption of component of the incidence light along the axis of the helices.

In the CD spectra region of 370-500 nm of the CD spectra, a broad monosignated peak with a maximum at around 410 nm can be seen that nicely correlates with the absorption maximum at 384 nm. In the CD region of 370-500 nm, the RH C3 has a positive signal and LH C3 has a negative signal. In the CD region of 320-370 nm, a characteristic bisignate dip-peak shape was observed, with the peak centered around the absorbance frequency. The RH C3 shows first a positive cotton effect at a longer wavelength followed by a negative one at a shorter wavelength (positive couplet). In contrast, LH C3 shows first a negative followed by a positive cotton effects (negative couplet). In both cases, the peak maxima of the first cotton effects are located at around 367 nm and those of the shorter wavelength are found about 347 nm with a crossover point at 358 nm. This zero transition corresponds well to the absorption peak at 358 nm (Figure 92A). The dotted lines are used to show the positions in the CD and UV spectra at the same wavelength more clearly. The CD signal is as high as thousands of mdeg, which to our knowledge has not been reported before.

However, in the original result, the RH and LH are not fully symmetric, for example, the CD value is not 0 mdeg at the crossover point 358 nm. To force the CD result symmetrically, we deal with the CD result in a tricky way. First, we reverse the CD value of LH chiral plasmon, the mirrored CD value can be got. Then the mirrored CD value is averaged with the CD result of RH chiral plasmon, C3 RH sum/2 is obtained in this way (Figure 92B black line). Second, we reverse the CD value of RH chiral plasmon, the mirrored CD value can be got. The mirrored CD value is also averaged with the CD result of the LH chiral plasmon, C3 LH sum/2 is obtained. By doing this, the LH and RH are fully symmetric, the CD value is 0 mdeg at the cross point at 358 nm and 510 nm. Also, it can be found that the position of the cross point around 358 nm and 510 nm don’t change. This can further testify the bisignate dip-peak shape at

358 nm and the monosignate peak at 410 nm.

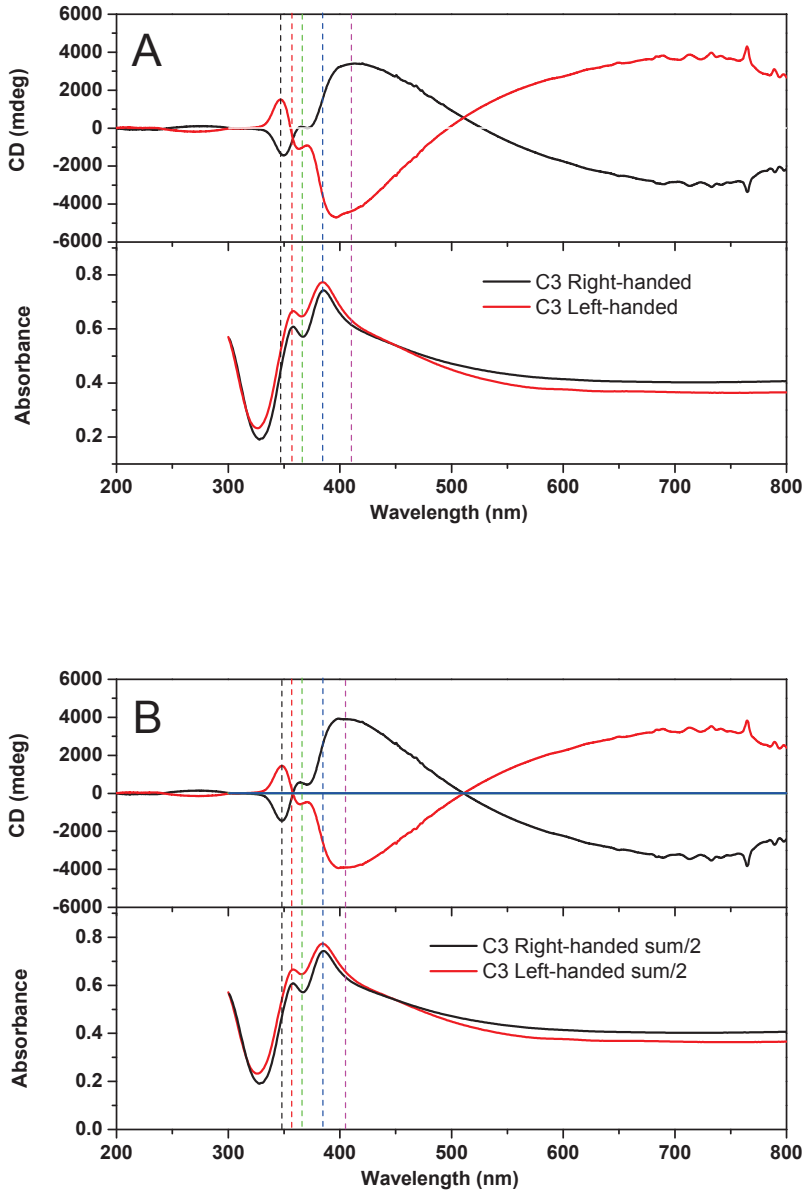

Figure 92. (A) CD spectra and UV spectra of the Right-handed (HH 3-69) and Left-handed (HH 3-72) sample. (B) CD spectra (averaged) and UV spectra of RH and LH sample.

In order to further check we got the true CD, we measured the CD from both the front side and the backside. In principal, the chiral plasmon films (LH and RH) are expected to produce same CD signal if it is measured from front side and back side.

Indeed, CD spectra measured on samples from both sides exhibit the anticipate results (Figure 93A). The CD spectra measured from the front side overlap with the CD spectra from the back side, which means that the configurations from the front side and back side are almost the same because of the same silver nanowire density in every layer and nice symmetry of the system.

The CD measurement were also performed with Mueller Matrix Polarimetry at the University of Barcelona (determination of the full Mueller Matrix), Scheme 6 presents the "Muellerimaging" results for the linear dichroism and circular dichroism of a helical superstructure. The parabolas and arrows indicate the approximate intersection of the spray cones with the receiving surface, the arrows indicates the spraying directions. The helix was built by spraying from three different directions onto the surface that differ by 60 degrees from one to the next. Purple, blue, yellow and red colors indicate strong dichroism, green color indicates weak dichroism. As expected, the helix structure is only present in the area where the three different spray jets overlapped (purple-bluish spot on the right), whereas high amounts of linear polariation are observed where only one spray jet has wetted the surface (blue, yellow and red areas on the left). The helical part of the film shows almost exclusively circular dichroism and almost no linear dichroism.

Figure 93B shows the comparison of the CD results of C3 samples measured from Mueller Matrix Polarimetry and Jasco, it can be seen that the shape of CD curve are almost the same, however the CD intensity measured from Mueller Matrix is higher than the CD measured from Jasco, this is because we measure the CD with a 1 mm pinehole sticked on the back side of the thin film, it measured the average value of the whole area, but the Mueller Matrix can find the position with highest CD intensity and measure it, so the CD intensity is higher than the CD result from the Jasco.

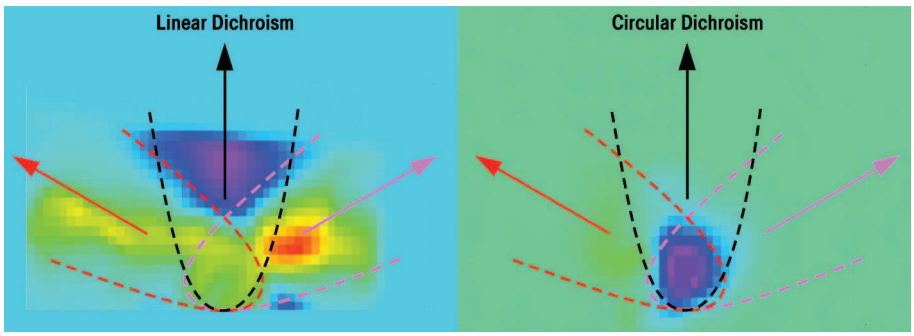

Scheme 6. Schematic representation of the "Muellerimaging" for the linear dichroism and circular dichroism of a helical superstructure.

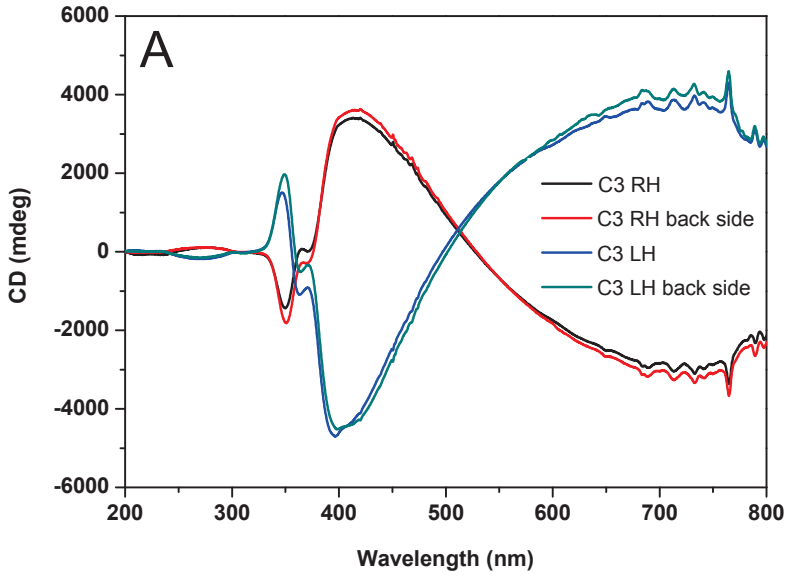

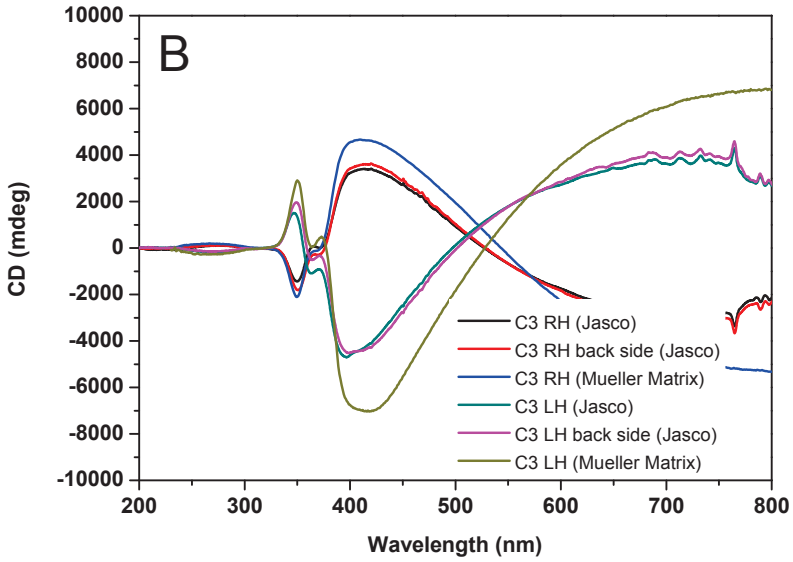

Figure 93. (A) CD spectra measured from front side and back side of RH sample (HH 3-69) and LH sample (HH 3-72) with Jasco; (B) Comparison of CD results from Jasco and Mueller Matrix.

The optical activity of chiral structures are usually dependent on their structrual asymmetry. The chiral response of the AgNW chiral plasmon can be characterized by the dissymmetry or anisotropy factor (g-factor):

$$g = \frac{\Delta\varepsilon}{\varepsilon}$$

Where Δε and ε are the molar circular dichroism and molar extinction, respectively. The g-factor can be calculated according to **Equation 14**. Figure 94 shows the anisotropy factor of RH and LH C3 helices. We obtained the maximum g-factor of ~ 0.2 around the peak at about 410 nm for RH-AgNW helices (C3), and ~ -0.2 around the peak at about 410 nm for LH-AgNW helices (C3). Our measured g-factors are about 10 times higher than the reported macroscopic gold nanorod systems[15]. Also, our g-factors are higher than the reported chiral plasmonic systems based on the silver nanowires[16]. This large g-factors of the AgNW helices maybe caused by the idealy alignment of silver nanowires and well-controlled arrangement of the helical configuration, aside from the contribution of the plasmon coupling among different

layers of silver nanowires.

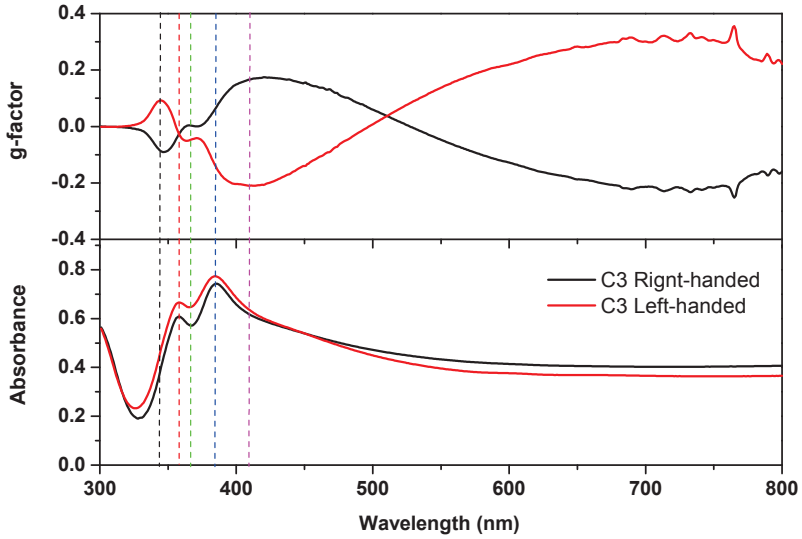

Figure 94. The anisotropy factors of RH- and LH- AgNW helices corresponding to the structures in **Figure 92**.

3.4.2 Chiral plasmonic nanostructure built with 3 layers of silver nanowires (AgNW suspension was diluted for 10 times) (HH 2-127 and HH 2-130)

In order to gain more insights into the mechanism behind the observed chiroptical response, we tried to prepare the C3 chiral plasmon with diluted silver nanowire suspensions since CD values depend on the concentration of the nanoparticles incorporated in the chiral system. Silver nanowire suspension was diluted for 10 times with ultrapure water, then it was incorporated into the chiral system in the same experimental condition as described before (same spraying time, same spacing between neighbored layers of AgNW).

Figure 95 A and B show the polarized UV-Vis-NIR of the diluted samples of RH C3 and LH C3 chiral plasmon, the extinction spectrum of silver nanowires displays two peaks at 362 and 380 nm in the UV-Vis region, the distances between these two peaks are smaller than the non-diluted samples, which maybe because the density is decreased and the coupling among the nanowires in the same layer is decreased

accordingly.

The spectra have also been recorded for polarization directions Φ varying from 0° to 360° with 20° steps. It can be seen that the absorbance from the UV region to the NIR does not change too much for the whole turn neither. The absorbance at 1500 nm is given in a polar plot as function of the polarization angle Φ in Figure 95 C.

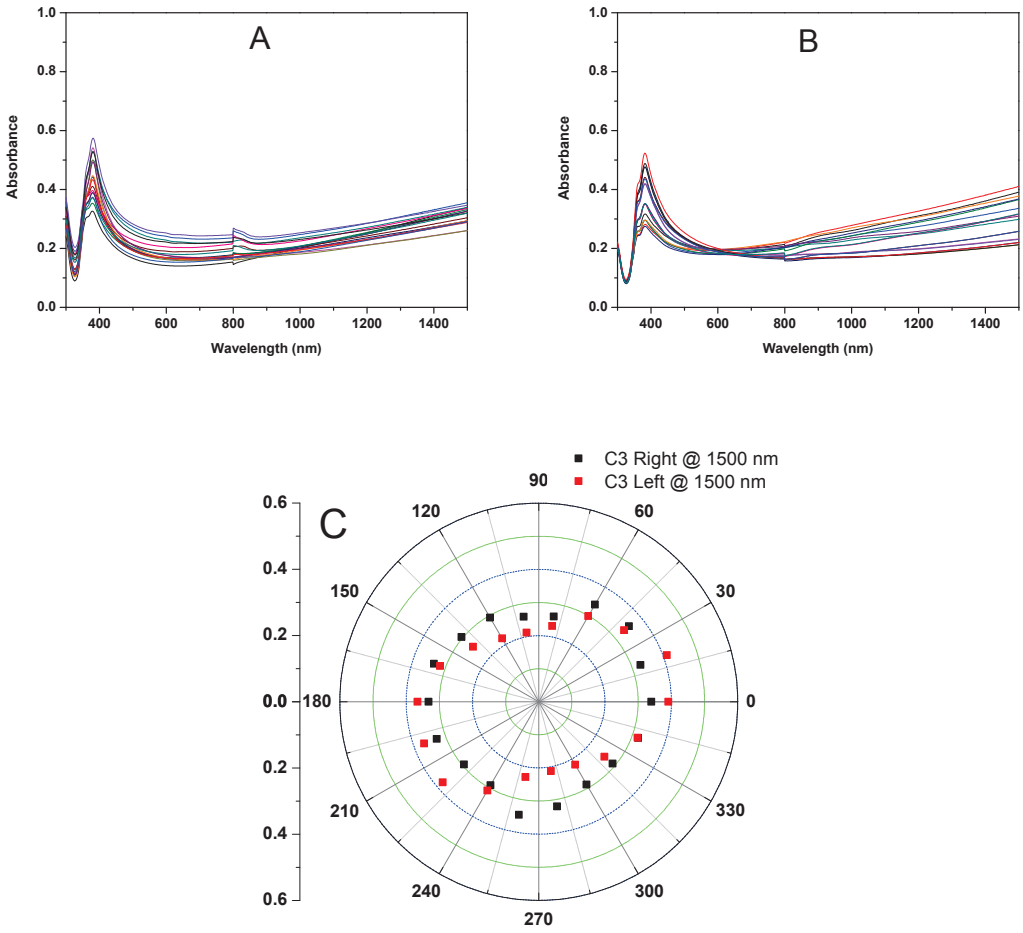

Figure 95. Polarized UV spectra of C3 chiral plasmonic nanostructure with lower AgNW density. (A) right-handed (HH 2-127); (B) left-handed (HH 2-130); (C) Polar plot of absorbance at 1500 nm as function of rotation angles.

Also, the chiral properties of the diluted C3 RH- and LH-AgNW helices were also investigated with CD spectrometer. Figure 96 shows the CD spectra and

non-polarized UV of the diluted C3 samples. Obviously, the CD signal decreased as the silver nanowire density decreased.

In the CD spectra region of 370-500 nm of the CD spectra, a broad monosignated peak with a maximum at around 400 nm can be seen that correlates with the absorption maximum at 380 nm. This peak blue-shifted about 10 nm compare to the higher concentration C3 samples, which may due to the lower density of silver nanowire. In the CD region of 320-370 nm, a characteristic bisignate dip-peak shape was observed, with the peak centered around the absorbance frequency. In both cases of RH and LH, the peak maxima of the first cotton effects located at around 364 nm becomes less obviously as the AgNW concentration decreased, which matches well with the UV result showed below.

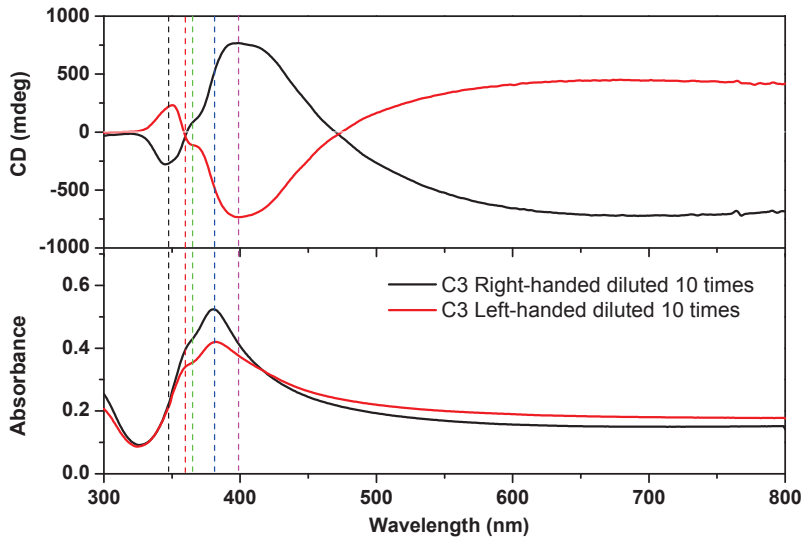

Figure 96. CD spectra and UV spectra of the RH (HH 2-127) and LH (HH 2-130) diluted C3 chiral plasmon sample.

Figure 97 shows the anisotropy factor of diluted RH and LH C3 helices. Almost all the peaks correspond well to the CD spectra, the monobisignated peak around 400 nm red-shifts 10 nm to 410 nm. For the diluted C3 samples, the obtained maximum g-factor of ~ 0.06 around the peak at about 410 nm for RH-AgNW helices (C3), and ~

-0.06 around the peak at about 410 nm for LH-AgNW helices (C3). Usually, for the same configuration with the same materials (same layers of silver nanowires and same spacing), it should have the same g-factor since it doesn't depend on the concentration of the nanoparticle, also all the parameters along the direction of light propagation are the same. However, in our cases the g-factor decreased obviously as decreasing the density of silver nanowires. This means that the coupling among the silver nanowires in the same layer also plays an important role in the optical properties. As the density of silver nanowire increased, the coupling among the AgNWs increased, which leads to improve the optical properties of the chiral plasmonic systems.

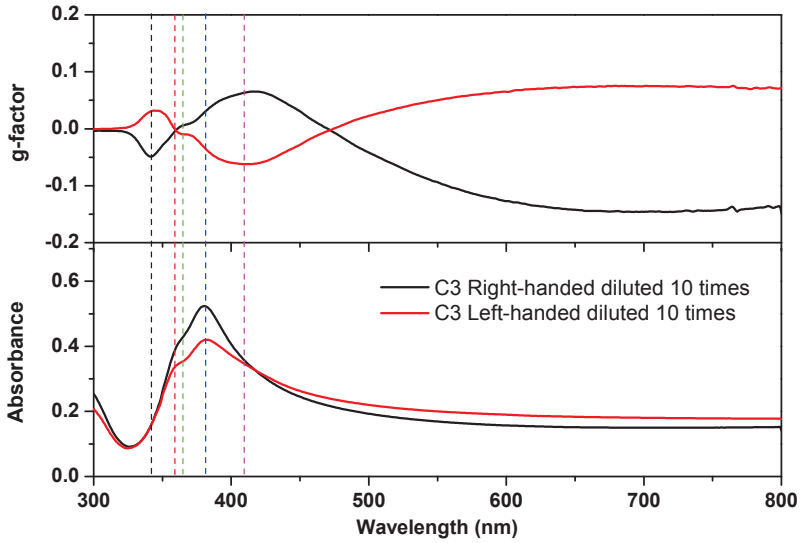

Figure 97. The anisotropy factors of RH- and LH- AgNW helices corresponding to the structures in **Figure 96**.

3.4.3 Chiral plasmonic nanostructure built with 4 layers of silver nanowires (C4) (HH 3-33 and HH 3-88)

The C4 chiral plasmonic nanosystems were prepared with the same method as C3 by just changing the twist angle, and C4 samples can be notes as PEI/AgNW/[PEI(PSS/PAH)$_5$PSS/PEI/AgNW]$_3$. Figure 98A and B show the SEM images of C4 RH and LH chiral plasmon, respectively. For C4 chiral nematic

structure, the silver nanowire density of every layer is also almost the same, and from the top-view SEM, the first layer of silver nanowire is not very obvious any more since the films are very thick and the nanowires are very dense. The twisted angle of C4 helices are 45° and - 45° for RH and LH, respectively.

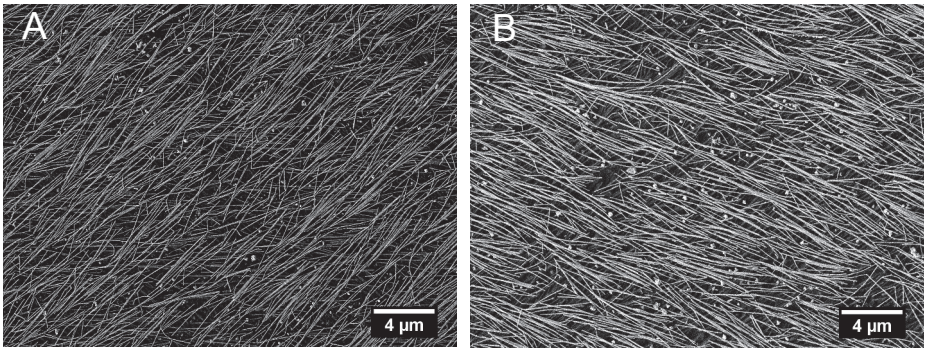

Figure 98. Top-view SEM image of HH 3-33 (A) and HH 3-88 (B)

Figure 99 A and B show the polarized UV-Vis-NIR of the RH C4 and LH C4 chiral plasmon. Again the absorbance was measured as function of the angle Φ between the incident light beam polarization plane and the placed C4 samples. The spectra have been recorded for the whole turn with 20° steps. It can be seen that the absorbances from the UV region to the NIR almost keep constant for the whole turn because it is symmetric for every layer of AgNW. The absorbance at 1500 nm is given in a polar plot as function of the polarization angle Φ in Figure 99 C, it has an circular shape for the whole turn. From UV range to NIR range, the absorbances of C4 samples are bigger than C3 samples because they have one more layer of silver nanowire.

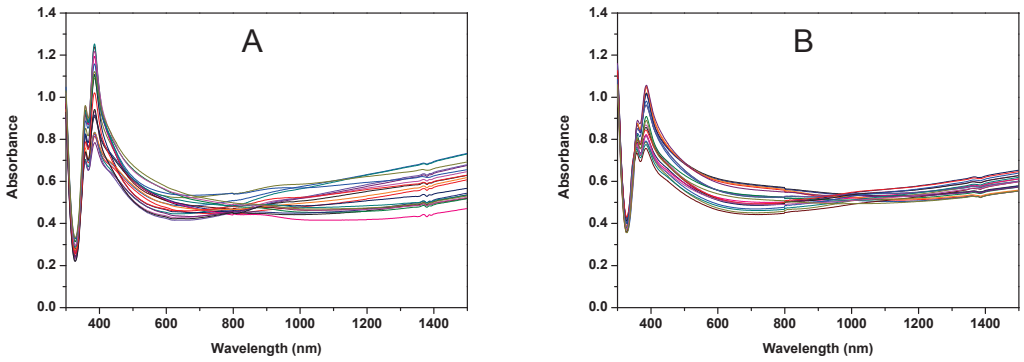

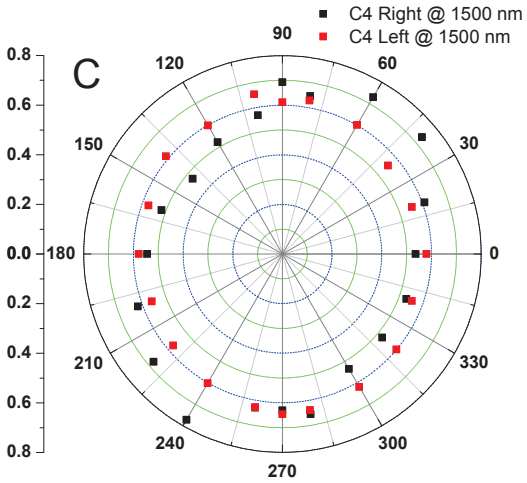

Figure 99. Polarized UV spectra of C4 chiral plasmon thin film as function of rotation angles. (A) right-handed (HH 3-33); (B) left-handed (HH 3-88); (C) Polar plot of absorbance at 1500 nm as function of rotation angles.

The CD spectra and non-polarized UV of assembled C4 RH- and LH-AgNW helices are shown in Figure 100A, Figure 100B show the CD spectra dealt with the method as C3 spectra used in order to force them fully symmetric. The CD spectra of the RH and LH C4 samples also show a nice symmetry. And the CD intensity of C4 samples is higher than C3. For example, at the wavelength of 410 nm, the CD intensities are ~ 7000 mdeg and ~ -7000 mdeg for RH C4 and LH C4 respectively. However, the CD intensities for C3 samples are around 4000 mdeg and -4000 mdeg. This is reasonable because the CD intensity is usually dependent on the amount of the nanoparticles in the helices. As the layers of AgNW increases, the number of nanoparticles increases, which leads to a higher CD signal.

From these two CD spectra, we can also conclude: in the CD spectra region of 370-500 nm, a broad monosignated peak with a maximum at around 415 nm can be seen that correlates with the absorption maximum at ~384 nm. As the layers of silver nanowires increased, this broad peak around 410 nm has red-shift in CD. In this region, RH C4 has a positive signal and LH C4 has a negative signal. In the CD region of 320-370 nm, the peak shape changes dramatically compare to C3 spectra. At

368 nm, the CD value of RH C4 is lower than 0 mdeg, and the CD value of LH C4 is higher than 0 mdeg, which make these two CD curves can not cross with each other around the absorption peak at 358 nm. Also, comparing the CD spectra of C3 with CD spectra of C4, we can see that the peaks at 373 nm of C4 samples become more obvious than C3 sample, this maybe because as the layers of AgNW increased, the twisted angle is smaller than C3 samples, which makes the samples more "dense", the coupling between neighbored layers of AgNW becomes stronger, so the peak at 373 nm becomes more clear, but this explaination is still lack of evidence, this phenomenon can be explained when we do the theoretical simulations. Anyway, the CD spectra of RH sample is mirrored to the CD spectra of LH sample.

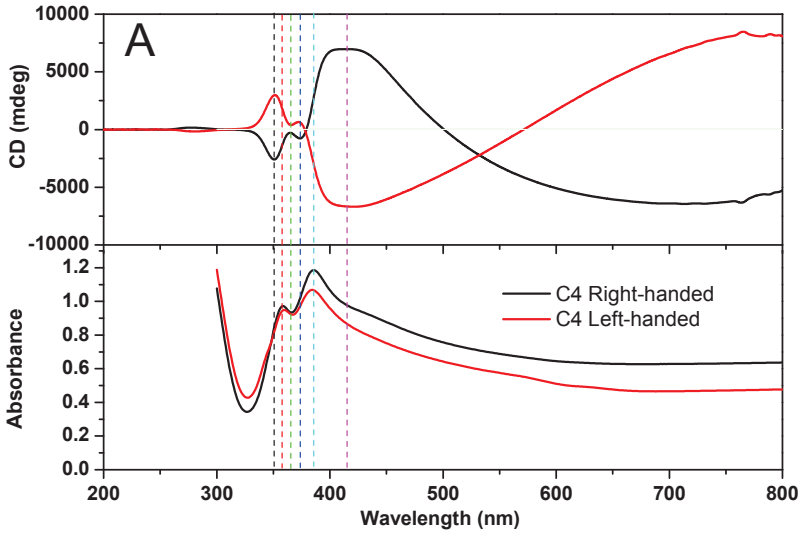

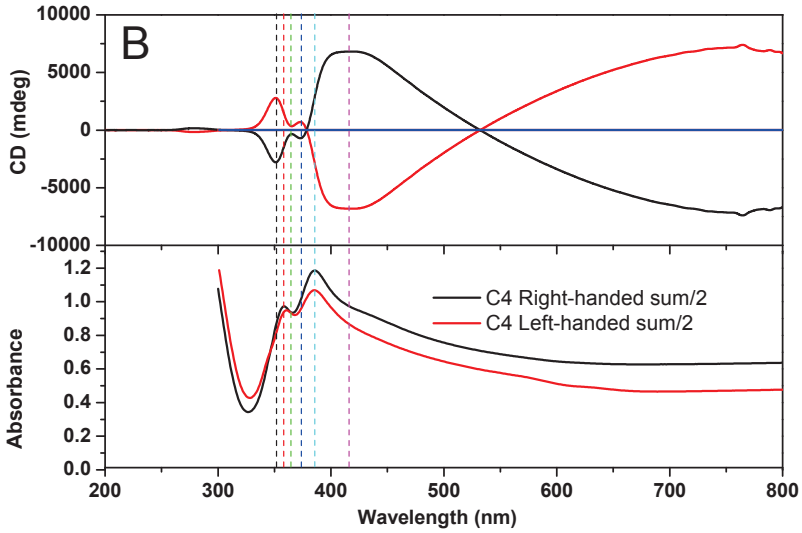

Figure 100. (A) CD spectra and UV spectra of the Right-handed (HH 3-33) and Left-handed (HH 3-88) sample. (B) CD spectra (averaged) and UV spectra of RH and LH sample.

Figure 101 shows the CD spectra measured from front side and back side of C4 samples. For both RH and LH C4 samples, the CD spectra from front side and back side is almost the same, which further confirms that the CD we obtained is true CD.

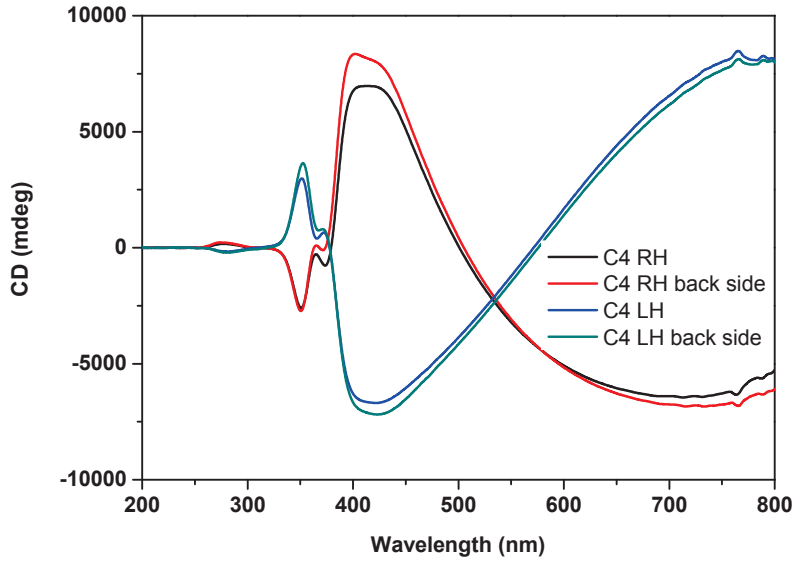

Figure 101. CD spectra measured from front side and back side of RH (HH 3-33) and LH (HH 3-88) C4 samples.

Figure 102A shows the comparison of the data of RH C4 sample measured from Mueller Matrix Polarimetry and Jasco with the same pinehole, it can be seen that these two technique give us almost the same results if we measured the CD with exactly same condition (same CD intensity and CD curve).

Figure 102B shows the comparison of the data of C4 samples from Jasco and Mueller Matrix Polarimetry, because the CD measured without pinehole on Mueller Matrix Polarimetry, so it measured the highest CD, the CD intensity from MMP is also much higher than the CD result from Jasco.

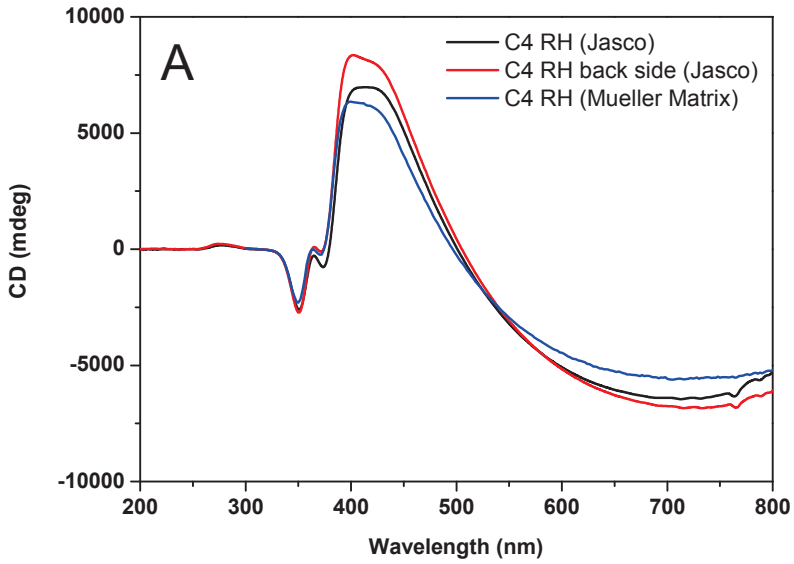

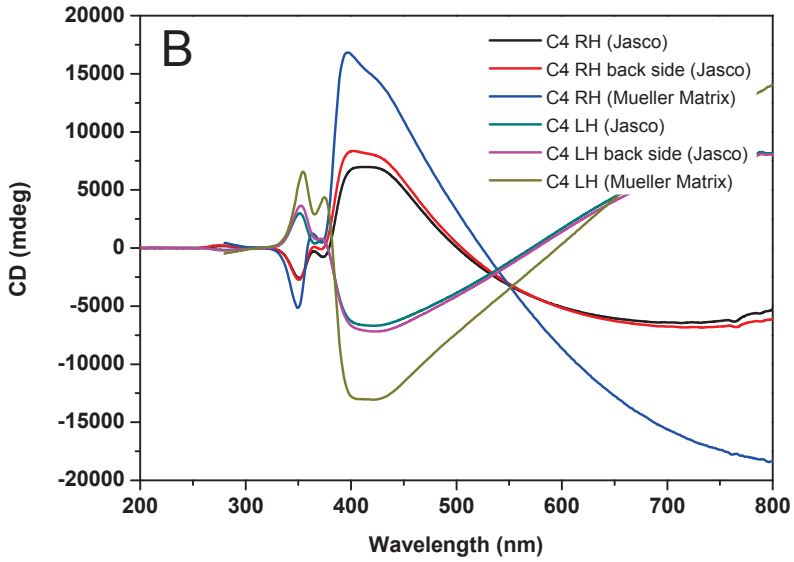

Figure 102. (A) Comparison of the CD data of RH (HH3-33) sample measured from Mueller Matrix Polarimetry and Jasco with pinehole; (B) Comparison of the CD data of C4 samples measured from Mueller Matrix Polarimetry and Jasco (on MMP, CD were measured without pinehole).

The g-factor of HH 3-33 and HH 3-88 helices is shown in Figure 103. The g-factor of the helices has the almost the same shape as the CD spectra. At 372 nm, the g-factor of RH C4 is lower than 0, and the g-factor of LH C4 is higher than 0, and two g-factor curve can not cross with each other around the peak at 358 nm, this is different from C3 sample, which means that the shape of g-factor curve and the CD spectra depend on the layers of silver nanowires.

And we can see that the maximum g-factor of RH C4 around the peak 420 nm is ~ 0.2, and the maximum g-factor of LH C4 at this wavelength is ~ -0.2. This means that the g-factor does not depend on the layers of silver nanowires, and if the chiral plasmonic nanostructure is prepared with the same concentration of silver nanowires, the g-factors keep constant for different configurations (C3, C4, C5, double C3 etc). We can estimate the approximate CD spectra from the configuration of the chiral plasmon. For example, he CD intensity of double C3 helix at around 420 nm should be about ±

8000 mdeg, the CD intensity of double C4 helix at around 420 nm should be about ± 14000 mdeg.

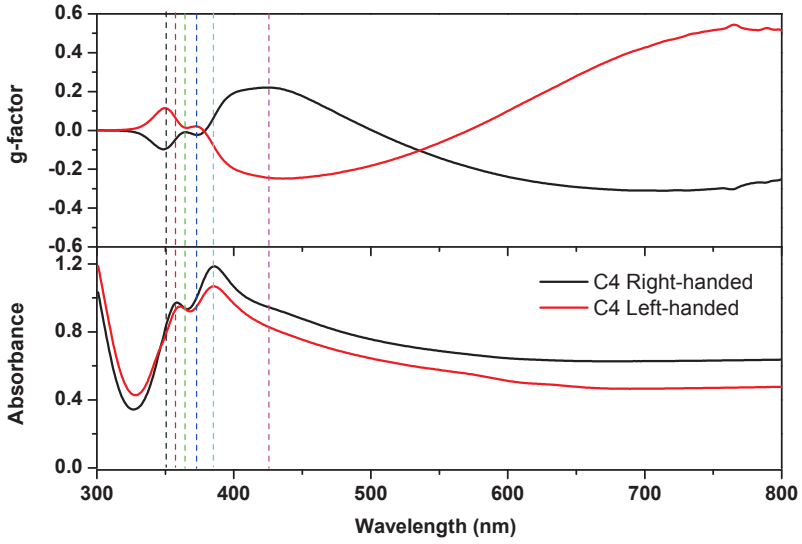

Figure 103. The anisotropy factors of RH- and LH- AgNW helices corresponding to the structures in **Figure 100**.

3.4.4 Chiral plasmonic nanostructure built with 4 layers of silver nanowires (AgNW suspension was diluted for 10 times) (HH 2-136 and HH 2-137)

Similarly, the C4 chiral plasmon were prepared with the diluted silver nanowire suspensions. Figure 104A and B show the polarized UV-Vis-NIR of the diluted samples of RH C4 and LH C4 chiral plasmon, the extinction spectrum of silver nanowires displays two peaks at 360 and 380 nm in the UV-Vis region. Similar to C3 diluted samples, the two peaks in the UV region merge together.

The spectra have also been recorded for polarization directions Φ varying from 0° to 360° with 20° steps. It can be seen that for C4 RH sample, the absorbance from the UV region to the NIR does not change too much for the whole turn (Figure 104A), but the C4 LH sample, when the polarizer turned to 120 degree, the absorbance in the NIR region is lower than the other angles, this may be because of the artifacts, the coverage of the fourth layer nanowire is lower than the previous three layers of silver

nanowires. When we measured CD and polarized UV, the sample is sticked with covers, the hole diameter of the cover for UV is 0.5 cm, which is bigger than the focus point of different layers of silver nanowires; the hole diameter of the cover for CD is less than 0.2 cm, which is smaller than the focus point of our sample. The CD can still be measured. The absorbance at 1500 nm is given in a polar plot as function of the polarization angle Φ in Figure 104 C.

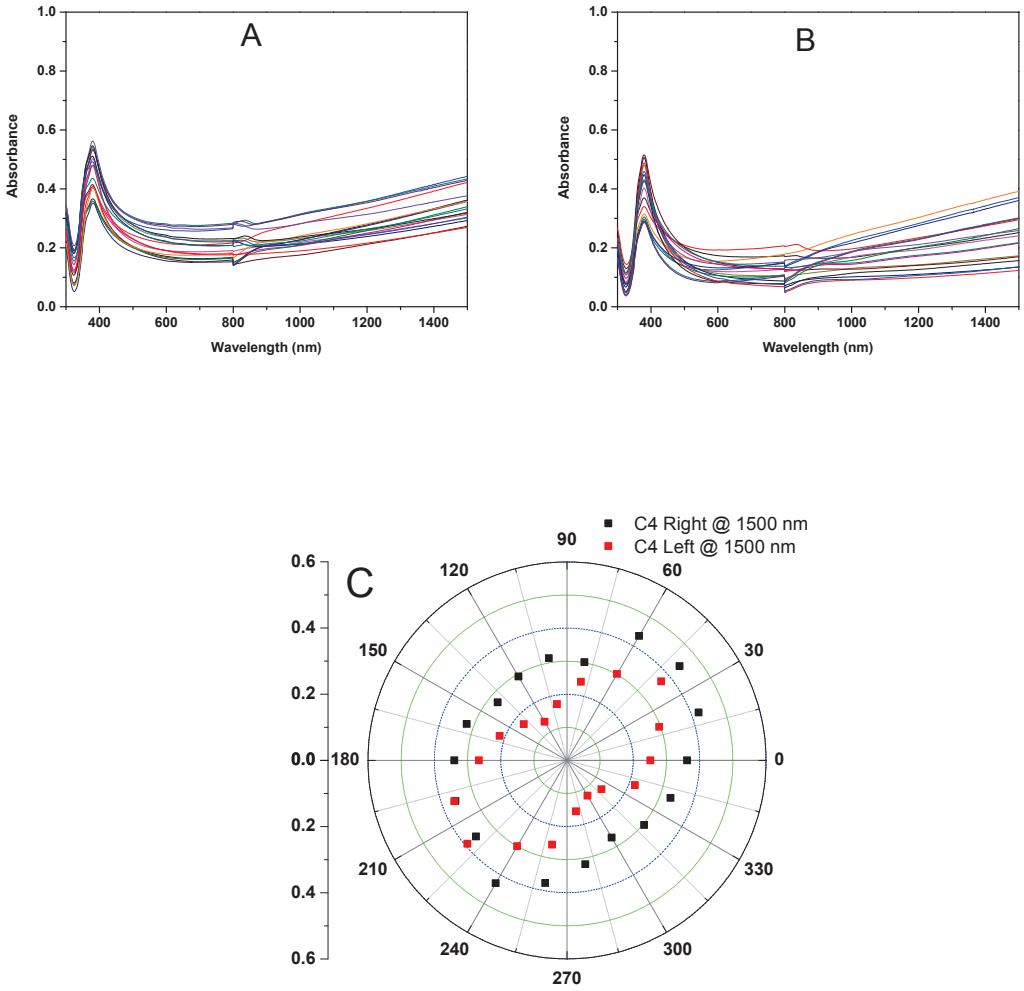

Figure 104. Polarized UV spectra of diluted C4 chiral plasmon. (A) right-handed (HH 2-136); (B) left-handed (HH 2-137); (C) Polar plot of absorbance at 1500 nm as function of rotation angles.

Figure 105 is the CD spectra of the diluted C4 samples, which shows a clear nice symmetry for LH and RH samples. The CD signal decreased obviously compare to

the non-diluted C4 samples, because of lower nanoparticle density. However, the CD intensity of the diluted C4 sample is a little bit higher than diluted C3 sample, because one more layer of silver nanowire is incorporated in the chiral systems.

In the CD spectra region of 370-500 nm of the CD spectra, a broad monosignated peak with a maximum at around 400 nm can be seen that correlates with the absorption maximum at 380 nm, which blue-shifted about 20 nm compare to the non diluted C4 samples (HH 3-33 and HH 3-88). In the CD region of 320-370 nm, a bisignate dip-peak shape was observed, with the peak centered around the absorbance frequency, this is different from the CD shape of non diluted C4 samples. For diluted C4 RH and LH, the peak maxima of the first cotton effects located at around 364 nm are less obvious like diluted C3 samples. We measured the CD of diluted C4 from different sides and different directions, the CD spectras are almost the same (Figure 106), which means that we get the true CD.

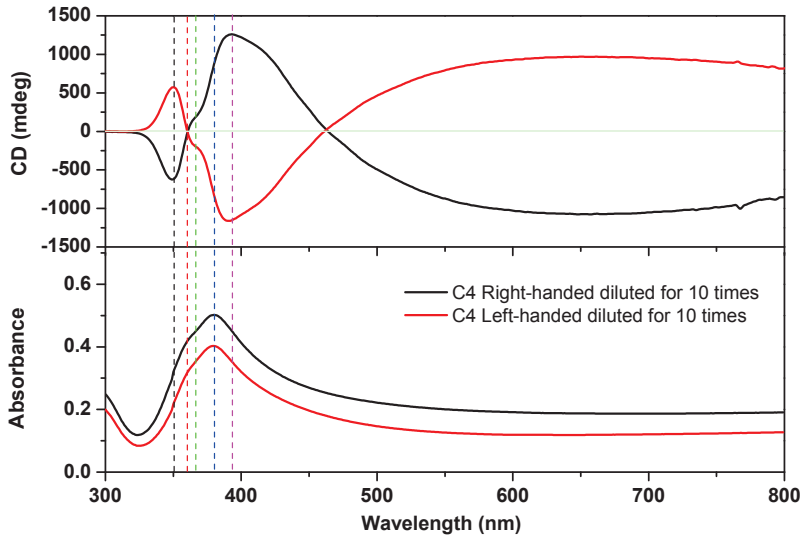

Figure 105. CD spectra and UV spectra of the RH (HH 2-136) and LH (HH 2-137) diluted C4 helical sample.

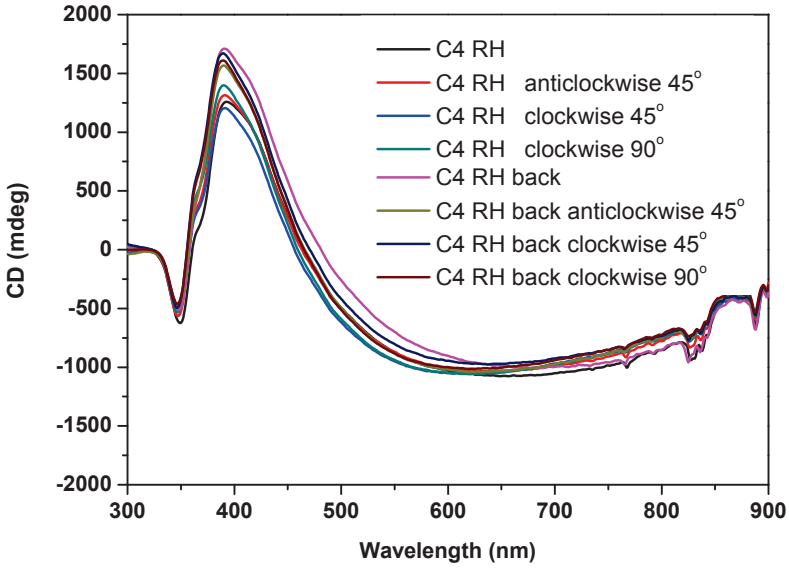

Figure 106. CD spectra of diluted RH C4 chiral plasmon sample measured from different sides and different directions.

Figure 107 shows the anisotropy factor of diluted RH and LH C4 helices. The g-factor curves show similar shapes to the CD spectra, the monobisignated peak around 390 nm red-shifts 20 nm to 410 nm. For the diluted C4 samples, the RH helice has the maximum g-factor of ~ 0.10 around the peak at around 410 nm, and the LH helice has the maximum g-facotr of ~ -0.10 around the peak at around 410 nm, which is comparable to the diluted C3 samples (± 0.06), this is because in diluted C3 and C4 samples, the density of silver nanowire in every layer is almost the same, which leads to the same coupling among nanowires.

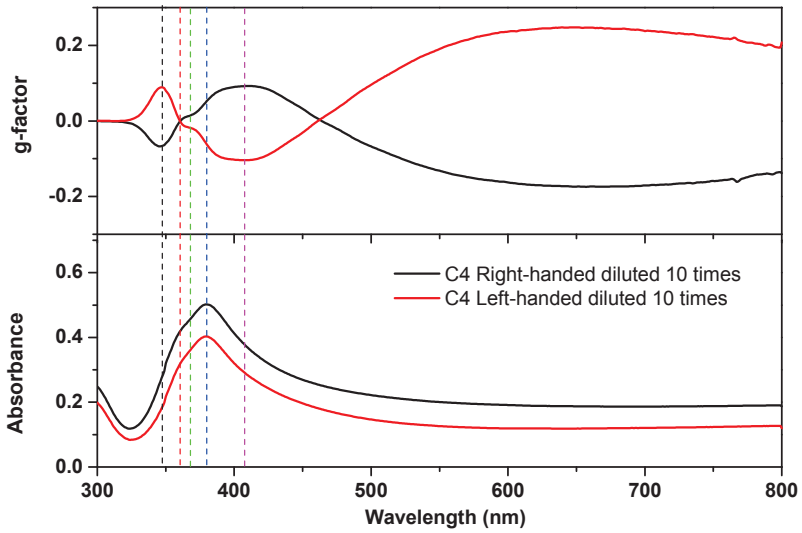

Figure 107. The anisotropy factors of RH- and LH- AgNW helices corresponding to the structures in **Figure 105**.

3.4.5 Influence of spacing on the chiroptical properties of chiral plasmonic nanostructure (HH 3-84 and HH 3-86, HH 3-73 and HH 3-71)

In order to study the influence of spacing between every adjacent AgNW layers on the chiroptical properties, we prepared the C4 chiral plasmonic samples with different spacing by simply changing the layer pairs of PSS/PAH (other parameters such as spraying time or twisted angle are kept constant). We prepared two other kind of C4 samples: PEI/AgNW/[PEI(PSS/PAH)$_n$PSS/PEI/AgNW]$_3$ (n = 10, 20), these two C4 samples different spacing will be compared with the previous C4 sample PEI/AgNW/[PEI(PSS/PAH)$_5$PSS/PEI/AgNW]$_3$. Figure 108A and B show the top-view SEM images of RH and LH chiral plasmonic samples of PEI/AgNW/[PEI(PSS/PAH)$_{10}$PSS/PEI/AgNW]$_3$. Comparing to former C4 samples PEI/AgNW/[PEI(PSS/PAH)$_5$PSS/PEI/AgNW]$_3$, we can get the silver nanowire density keeps almost the same. From the top-view of SEM, only the top two layers can be seen very clearly since as the layer pairs of PSS/PAH increased to 10, the spacing between adjacent silver nanowire layers is about 30 nm.

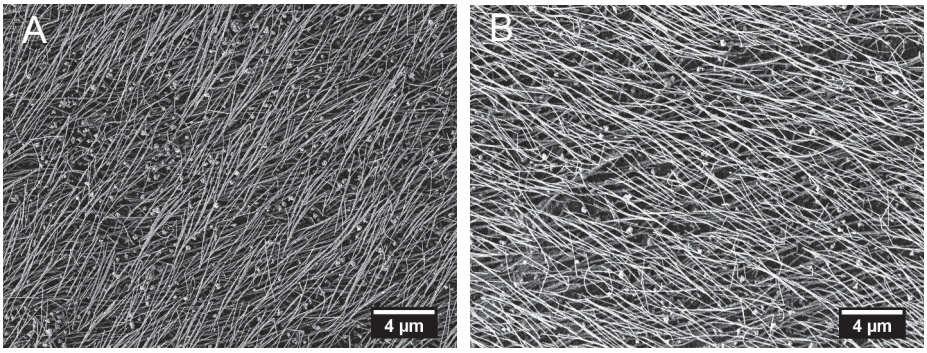

Figure 108. Top-view SEM image of HH 3-84(A) and HH 3-86 (B)

The polarized UV-Vis-NIR spectra of RH and LH C4 samples (PEI/AgNW/[PEI(PSS/PAH)$_{10}$PSS/PEI/AgNW]$_3$) are given in Figure 109 A and B. The spectra was recorded every 20 degrees. It can be seen that the absorbances are almost the same as PEI/AgNW/[PEI(PSS/PAH)$_5$PSS/PEI/AgNW]$_3$ samples, because they have almost the same nanowires densities. In principal, the absorbance from the UV region to the NIR region should not change too much for the whole turn, the results came as anticipited. The absorbance of 1500 nm is given in a polar plot as function of the rotation angles of the polarizer (Figure 109 C), again it is a circular shape for the whole turn.

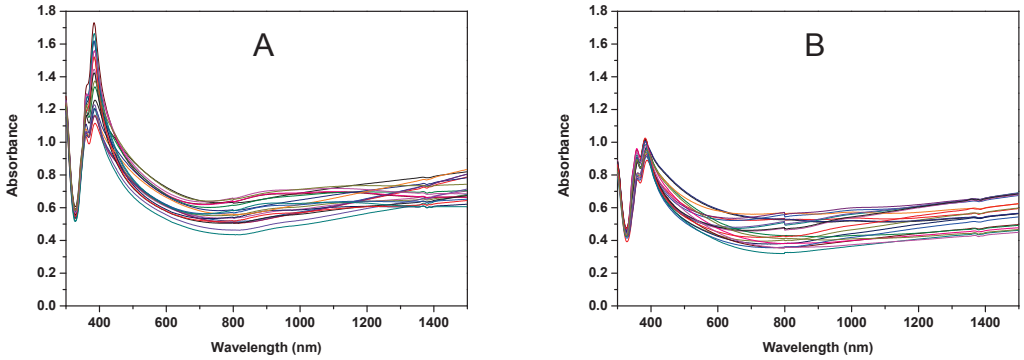

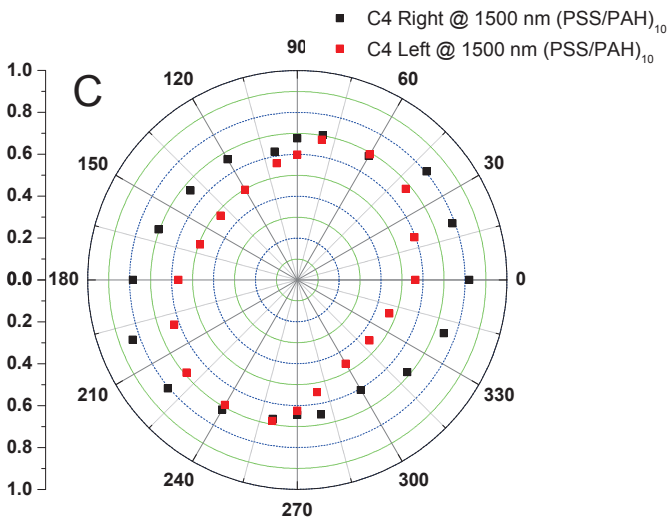

Figure 109. Polarized UV spectra of C4 chiral plasmon thin film as function of rotation angles. (A) right-handed (HH 3-84); (B) left-handed (HH 3-86); (C) Polar plot of absorbance at 1500 nm as function of rotation angles.

The CD spectra and the non-polarized UV spectra of assembled C4 RH- and LH-AgNW helices (PEI/AgNW/[PEI(PSS/PAH)$_{10}$PSS/PEI/AgNW]$_3$) are shown in Figure 110A. Figure 110B shows the CD spectra also dealt with the averaged method in order to force them fully symmetric. We can see that the non-polarized UV doesn't change too much comparing to the (PEI/AgNW/[PEI(PSS/PAH)$_5$PSS/PEI/AgNW]$_3$) samples. The CD spectra of the RH and LH (PEI/AgNW/[PEI(PSS/PAH)$_{10}$PSS/PEI/AgNW]$_3$) C4 samples also show a mirror image relation. As the intelayer spacing increased, the CD intensities don't change too much, for example, at the wavelength of ~420 nm, the CD intensities are still ~ 7000 mdeg and ~ -7000 mdeg for RH C4 and LH C4 respectively, this maybe due to the fact that the silver nanowires are sprayed usually for 200 seconds for all the samples, so the density of the nanoparticles in the chiral plasmon should be constant, which leads to the same CD intensity.

Interestingly, the CD spectra shape changes a lot comparing to C4 samples PEI/AgNW/[PEI(PSS/PAH)$_5$PSS/PEI/AgNW]$_3$. In the CD spectra region of 370-500 nm, the broad monosignated peak has red-shift of 10 nm to 425 nm, this peak

correlates with the absorption peak at 384 nm. This means as the spacing increased, this broad peak around 415 nm has red-shift in CD spectra but no shift in UV spectra. And this peak becomes broader than PEI/AgNW/[PEI(PSS/PAH)$_5$PSS/PEI/AgNW]$_3$ samples, for example, the CD spectra of LH and RH PEI/AgNW/[PEI(PSS/PAH)$_5$PSS/PEI/AgNW]$_3$ samples cross at ~533 nm, but cross position is ~610 nm for PEI/AgNW/[PEI(PSS/PAH)$_{10}$PSS/PEI/AgNW]$_3$ samples.

In the CD region of 320-370 nm, the peak shape changes obviously. At 368 nm, the CD value of RH sample is lower than 0 mdeg, and CD value of LH sample is higher than 0 mdeg, these two CD curves can not cross with each other around the peak at 358 nm. As the spacing increased, the peaks at ~374 nm are even more obvious, for example, the CD intensity at 350 nm is much bigger than CD at 373 nm for PEI/AgNW/[PEI(PSS/PAH)$_5$PSS/PEI/AgNW]$_3$ sample, but the CD intensity at 350 nm is almost equal to CD at 374 nm for PEI/AgNW/[PEI(PSS/PAH)$_{10}$PSS/PEI /AgNW]$_3$ sample. Figure 111A shows the CD spectra measured from front side and back side of PEI/AgNW/[PEI(PSS/PAH)$_{10}$PSS/PEI/AgNW]$_3$ samples, the CD spectra from front side and back side is also almost the same, Figure 111B shows the comparison of CD results measured from Jasco and Mueller Matrix, again the CD from MMP is higher than CD from Jasco, also the CD from MMP of these samples are in the same range with the MMP results of PEI/AgNW/[PEI(PSS/PAH)$_5$PSS/PEI/AgNW]$_3$ samples, the CD intensity is ~ 14000 mdeg.

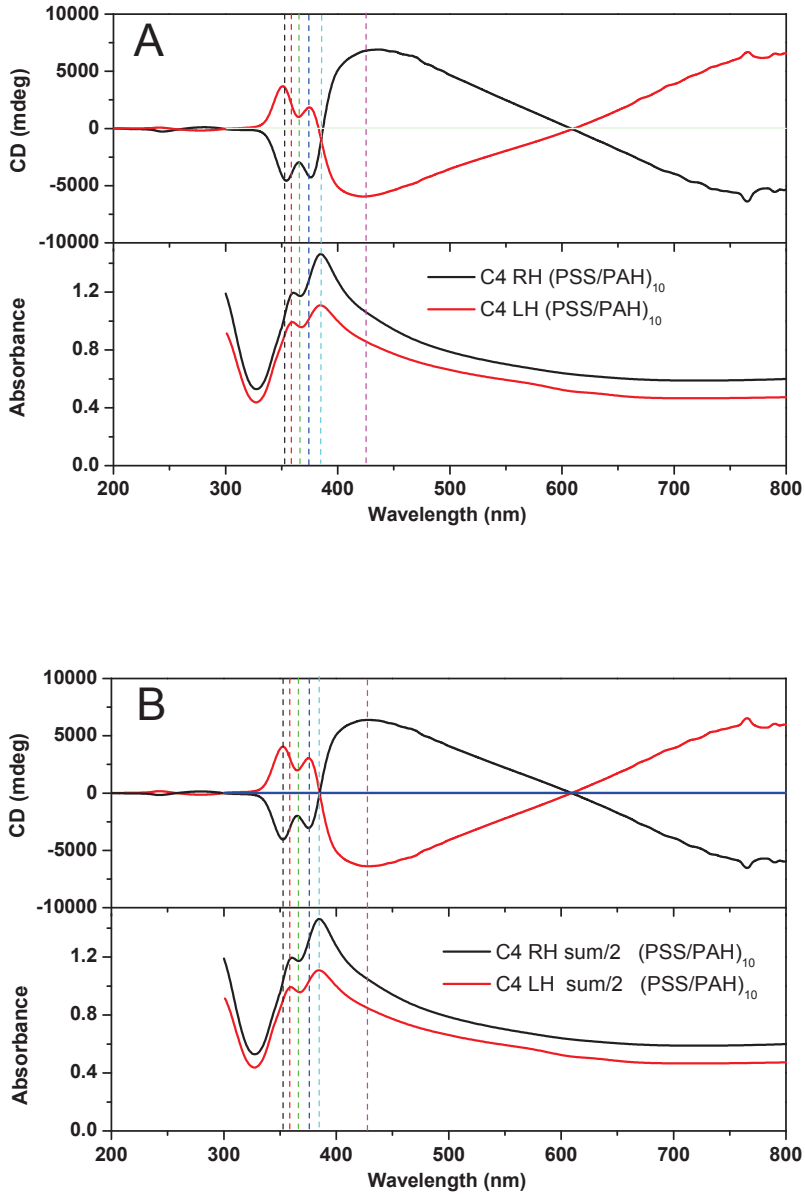

Figure 110. (A) CD spectra and UV spectra of the RH (HH 3-84) and LH (HH 3-86) sample. CD spectra (averaged) and UV spectra of RH and LH sample.

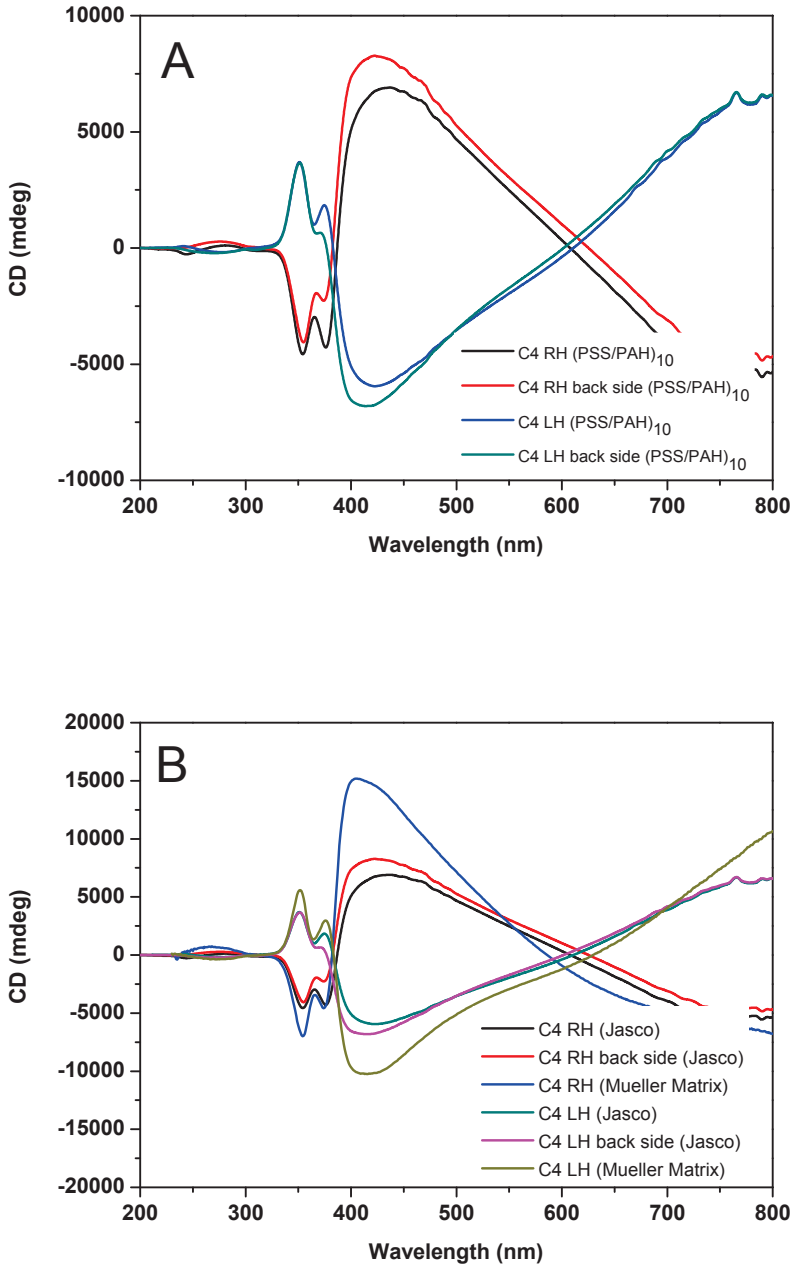

Figure 111. (A) CD spectra measured from front side and back side of RH (HH 3-84) and LH (HH 3-86) C4 samples; (B) Comparison of the CD data of C4 samples (HH 3-84 and HH 3-86) measured from Mueller Matrix Polarimetry and Jasco (on MMP, CD were measured without pinehole).

The g-factor of PEI/AgNW/[PEI(PSS/PAH)$_{10}$PSS/PEI/AgNW]$_3$ helices is also

calculated (Figure 112). The g-factor curve has similar shape as the CD curve. At 375 nm, the g-factor of RH C4 is lower than 0, and the g-factor of LH C4 is higher than 0, and two g-factor curve can not cross with each other around the peak at 358 nm. At 350 nm, the g-factor of PEI/AgNW/[PEI(PSS/PAH)$_{10}$PSS/PEI/AgNW]$_3$ is equal to the g-factor of PEI/AgNW/[PEI(PSS/PAH)$_5$PSS/PEI/AgNW]$_3$ sample, but at 375 nm, the g-factor increases dramatically as the spacing increases. The same as the CD spectra, the g-factor curves become broader and crosses at 384 nm and 610 nm.

And we can see that the maximum g-factor of RH C4 around the peak 420 nm is ~ 0.2, and the maximum g-factor of LH C4 at this wavelength is ~ -0.2, these values are comparable to PEI/AgNW/[PEI(PSS/PAH)$_5$PSS/PEI/AgNW]$_3$ samples, which means the maximum g-factor values are indenpendent on the spacing between every neighbored silver nanowires.

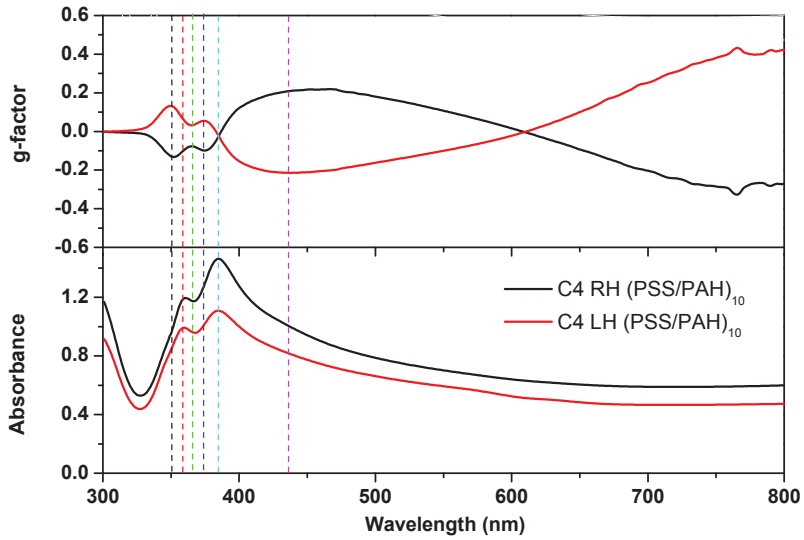

Figure 112. The anisotropy factors of RH- (HH 3-84) and LH- (HH 3-86) helices.

Figure 113A and B are the top-view SEM images of RH and LH chiral plasmonic samples of PEI/AgNW/[PEI(PSS/PAH)$_{20}$PSS/PEI/AgNW]$_3$. The SEM images show the mirrored helices clearly. The thickness of (PSS/PAH)$_{20}$ is about 60 nm, which is

about 2 times of the silver nanowire diameter. However, the silver nanowire density is still not influenced by inserting so big spacing between adjacent nanowire layers.

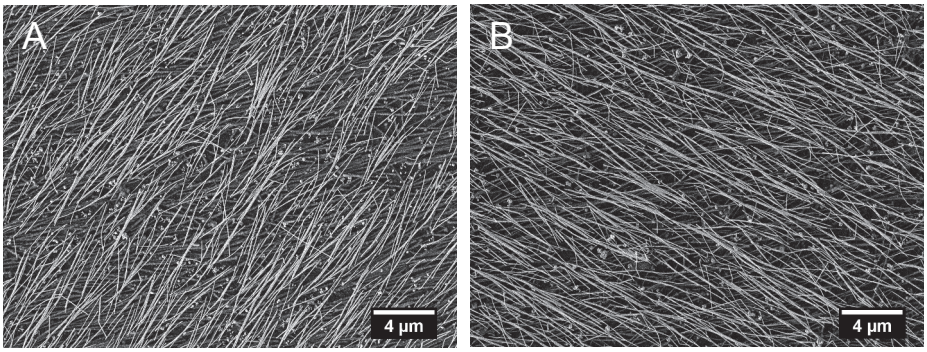

Figure 113. Top-view SEM image of HH 3-73 (A) and HH 3-71 (B)

Figure 114A and B present the polarized UV-Vis-NIR spectra of RH and LH C4 samples (PEI/AgNW/[PEI(PSS/PAH)$_{20}$PSS/PEI/AgNW]$_3$). The spectra was also recorded by rotating the polarizer every 20 degrees. It can be got that the intensities of UV are almost the same as PEI/AgNW/[PEI(PSS/PAH)$_n$PSS/PEI/AgNW]$_3$ (n =5, 10) samples, because they have similar nanowires densities. As the previous C4 samples, the absorbance from the UV region to the NIR region should not change too much for the whole turn because of their symmetric properties, it turns out as anticipited. The absorbance of 1500 nm is given in a polar plot as function of the rotation angles of the polarizer (Figure 114 C), it is also a circular shape for the whole round.

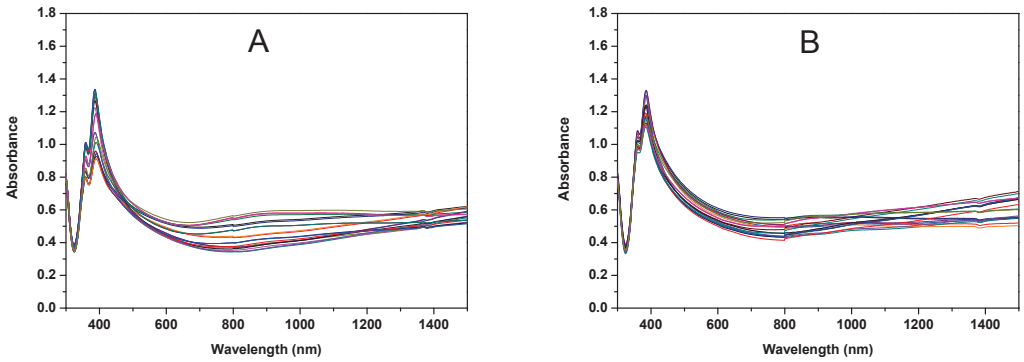

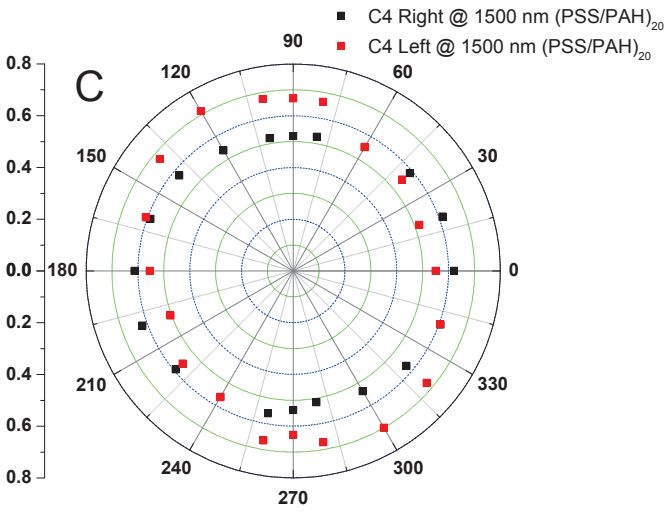

Figure 114. Polarized UV spectra of C4 chiral plasmon thin film as function of rotation angles. (A) right-handed (HH 3-73); (B) left-handed (HH 3-71); (C) Polar plot of absorbance at 1500 nm as function of rotation angles.

The CD spectra and the non-polarized UV spectra of assembled C4 RH- and LH-AgNW helices (PEI/AgNW/[PEI(PSS/PAH)$_{20}$PSS/PEI/AgNW]$_3$) are shown in Figure 115A. Figure 115B shows the CD spectra dealt with the averaged method. The CD spectra of the RH and LH (PEI/AgNW/[PEI(PSS/PAH)$_{20}$PSS/PEI/AgNW]$_3$) C4 samples also show a mirror relation. As the intelayer spacing increased, the CD intensities are in the same range as the previous C4 samples. At the wavelength of ~420 nm, the CD intensities are still ~ 7000 mdeg and ~ -7000 mdeg for RH C4 and LH C4 respectively.

The shape of the CD spectra is similar to CD spectra of PEI/AgNW/[PEI(PSS/PAH)$_{10}$PSS/PEI/AgNW]$_3$. In the CD spectra region of 370-500 nm, the broad monosignated peak locates at 425 nm, this peak correlates with the absorption peak at 384 nm. And this peak is broader than PEI/AgNW/[PEI(PSS/PAH)$_5$PSS/PEI/AgNW]$_3$ samples, the cross position is ~600 nm.

At 368 nm, the CD value of RH samples is still lower than 0 mdeg, and CD value of

LH C4 is higher than 0 mdeg, these two CD curves can not cross with each other around the peak at 358 nm. As the spacing increased from $(PSS/PAH)_{10}$ to $(PSS/PAH)_{20}$, the peaks at ~374 nm shift to ~377 nm. Also the CD intensity at 350 nm is almost equal to CD at 377 nm for PEI/AgNW/$[PEI(PSS/PAH)_{20}PSS/PEI/AgNW]_3$ sample. Figure 116A shows the CD spectra measured from front side and back side of PEI/AgNW/$[PEI(PSS/PAH)_{20}PSS/PEI/AgNW]_3$ samples, the CD spectra from front side and back side is also almost the same. Figure 116B shows the comparison of the CD result from MMP and Jasco, we can see that the CD results are almost the same, which indicates that these samples are more homogeneous than the previous samples (HH 3-33, 88, 84, 86), it shows almost the same CD results when we measured from different area.

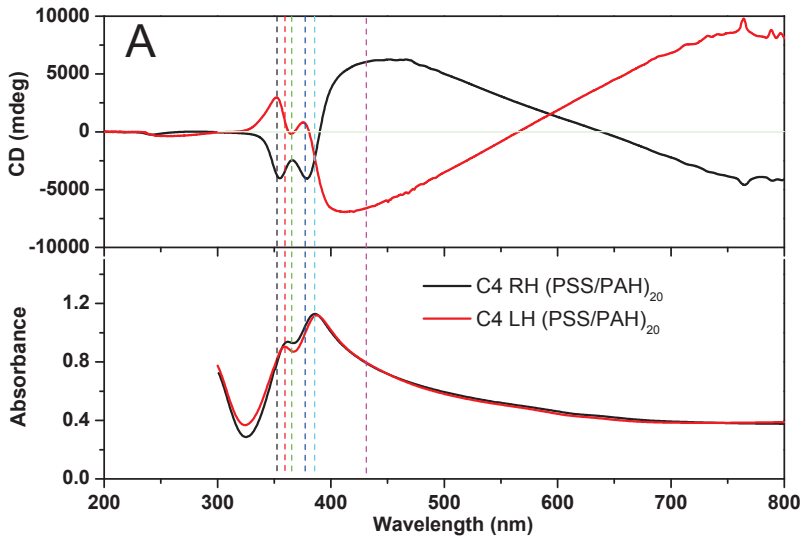

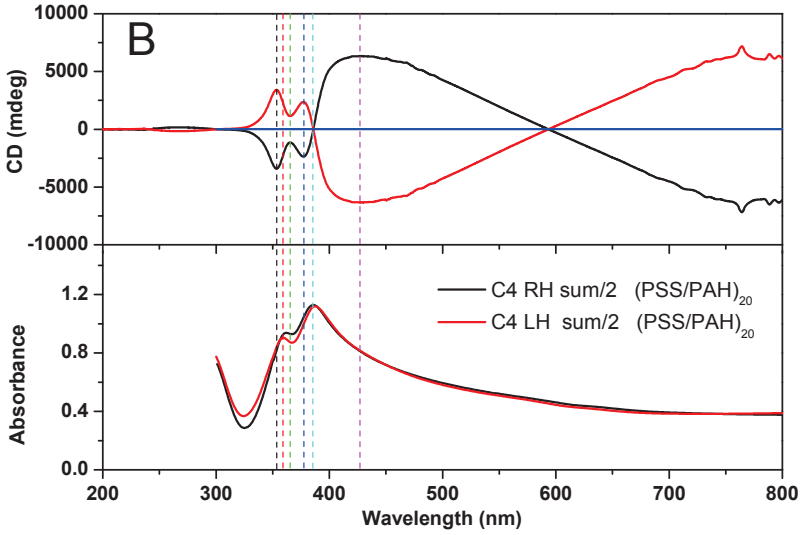

Figure 115. (A) CD spectra and UV spectra of the Right-handed (HH 3-73) and Left-handed (HH 3-71) sample. (B) CD spectra (averaged) and UV spectra of RH and LH sample.

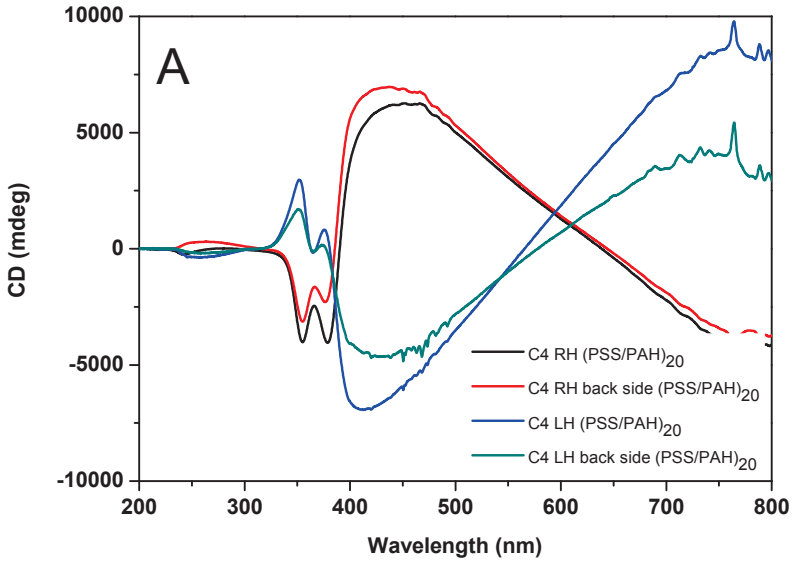

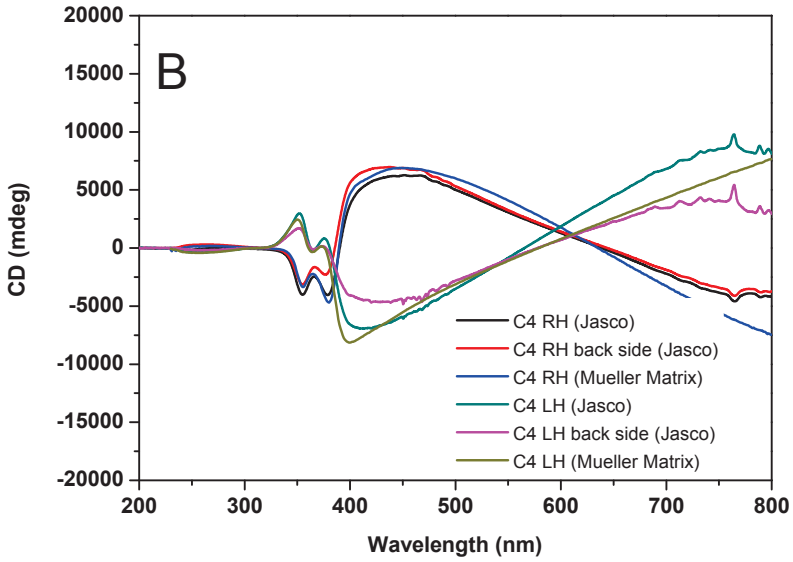

Figure 116. (A) CD spectra measured from front side and back side of RH (HH 3-73) and LH (HH 3-71) C4 samples; (B) Comparison of the CD data of C4 samples (HH 3-73 and HH 3-71) measured from Mueller Matrix Polarimetry and Jasco (on MMP, CD were measured without pinehole).

Figure 117 presents the g-factor of PEI/AgNW/[PEI(PSS/PAH)$_{20}$PSS/PEI/AgNW]$_3$ helices. The g-factor curve is similar to the shape of CD curve. At 377 nm, the g-factor of RH C4 is lower than 0, and the g-factor of LH C4 is higher than 0, and two g-factor curve can not cross with each other around the peak at 358 nm. At ~350 nm and ~377 nm, the g-factors of PEI/AgNW/[PEI(PSS/PAH)$_{20}$PSS/PEI/AgNW]$_3$ are in the same range as the g-factor of PEI/AgNW/[PEI(PSS/PAH)$_{10}$PSS/PEI/AgNW]$_3$ samples. The same as the CD spectra, the g-factor curves become broader and cross at 385 nm and ~ 600 nm.

And we can see that the maximum g-factor of RH C4 around the peak 420 nm is ~ 0.2, and the maximum g-factor of LH C4 at this wavelength is ~ -0.2, these values are almost the same as PEI/AgNW/[PEI(PSS/PAH)$_n$PSS/PEI/AgNW]$_3$ (n = 5, 10) samples. By comparing the CD spectra and g-factors of these three C4 chiral helices with different spacing, we can conclude: the shapes of the CD spectra and g-factor

curves are dependent on the spacing, nevertheless g-factor value is mainly dependent on the silver nanowire density in our chiral systems.

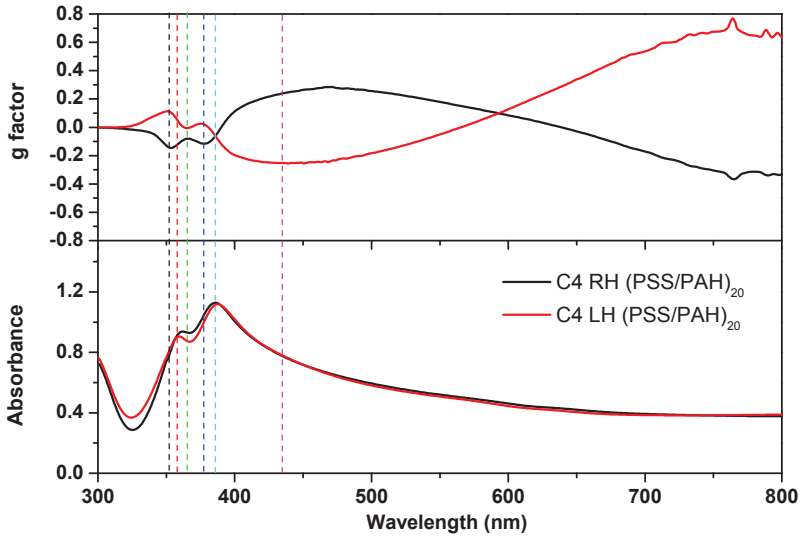

Figure 117. The anisotropy factors of RH- (HH 3-73) and LH- (HH 3-71) helices.

Bibliography

1. Wiley, B.; Sun, Y.; Xia, Y. *Acc. Chem. Res.* 2007, 40, 1067-1676.
2. Chen, M.; Phang, I. Y.; Lee, M. R.; Yang, J. K. W.; Ling, X. Y. *Langmuir* 2013, 29. 7061-7069.
3. Paula, M.M.D.; da Costa, C. S.; Baldin, M. C.; Scaini, G.; Rezin, G. T.; Segala, K.; De Andrade, V. M.; Franco, C. V.; Streck, E. L. *J. Braz. Chem. Soc.*, 2009, 20, 1556
4. Decher, G.; Blell, R.; Hu, H.; Pauly, M.; Felix, O.; Martel, D.; Lin, X.; Sekar, S.; Diabang, S.; Bayer, J. European Patent, Patent No.: 14305725.5-1504.
5. Sheikholeslami, S.; Jun, Y. W.; Jain, P. K.; Alivisatos, A. P. *Nano Lett.* 2010, 10, 2655-2660.
6. Nie, Z. H.; Petukhova, A.; Kumacheva, E. *Nat. Nanotechnol.* 2010, 5, 15-25.
7. Chen, W.; Bian, A.; Agarwal, A.; Liu, L. Q.; Shen, H. B.; Wang, L. B.; Xu, C. L.; Kotov, N. A.; *Nano Lett.* 2009, 9, 2153-2159.
8. Gubler, U.; Bosshard, C.; *Nat. Mater.* 2002, 1, 209-210.
9. Tang, Y. Q.; Cohen, A. E. *Science* 2011, 332, 333-336.
10. Zhao, R.; Zhou, J.; Koschny, T.; Economou, E. N.; Soukoulis, C. M. *Phys. Rev. Lett.* 2009, 103, 103602.
11. Hendry, E.; Carpy, T.; Johnston, J.; Popland, M.; Mikhaylovskiy, R. V.; Lapthom, A. J.; Kelly, S. M.; Barron, L. D.; Gadegaard, N.; Kadodwala, M. *Nat. Nanotechnol.* 2010, 5, 783-787.
12. Kildishev, A. V.; Boltasseva, A.; Shalaev, V. M. *Science* 2013, 339, 1232009.
13. Papakostas, A.; Potts, A.; Bagnall, D. M.; Prosvirnin, S. L.; Coles, H. J.; Zheludev, N. I. *Phys. Rev. Lett.* 2003, 90, 107404.
14. Agranat, I.; Caner, H.; Caldwell, A. *Nat. Rev. Drug Discov.* 2002, 1, 753-768.
15. Lan, X.; Lu, X. X.; Shen, C. Q.; Ke, Y. G.; Ni, W. H.; Wang, Q. B. *J. Am. Chem. Soc.* 2015, 137, 457-462.
16. Chu, G.; Wang, X. S.; Chen, T. R.; Gao, J. X.; Gai, F. Y.; Wang, Y.; Xu, Y. *ACS Appl. Mater. Interfaces* 2015, 7, 11863-11870.

Conclusion and Perspective

The goal of this research was to align the one-dimenional nanostructures by grazing-incidence spraying and build interesting structures by combing grazing-incidence spraying (GIS) and Layer-by-Layer technique. Silver nanowires were taken as model object for one-demensional structures. Silver nanowire have a aspect ratio about 100, can be aligned on various substrates (Silicon, glass, quartz etc) along the spraying direction because of the shear force. The best parameters for alignment are 1 cm of downstream distance and 30 L/min of air flow. The nanowire density can be tuned very easily by changing the sparying time. Different from the disordered thin film, the optical properties of aligned silver nanowire thin films depend on the polarization of the incident light, the absorbance in the NIR range is high when the longitudinal SPR band is excited, and the absorbance in the near-UV range is high when the transverse SPR bands are excited.

The silver nanowire can be incorporated into Layer-by-Layer films because its negative zeta-potential (-33.4 mV), by combining GIS and LbL technique, novel three dimensional architechture can be fabricated. In order to keep the orientation of the former layers, some polyelectrolyte [PEI/$(PSS/PAH)_n$PSS/PEI] was inserted between every adjacent layers of silver nanowires, UV and Side-view SEM can both monitor the Layer-by-Layer build up, for 5 layer pairs of PSS/PAH, the thickness of one layer of silver nanowire plus the polymers is ~ 50 nm. The same or different direction multilayers of silver nanowires can be built by tuning the sparying direction.

The multilayers of silver nanowire nanostructures aligned in the same direction show also obvious anisotropic properties, they can be served as excellent wavelength dependent polarizers, the polarization efficiency (PE) increases as increasing the layers of silver nanowires, the PE can get close to the maximum value of 100% for 4 layers of silver nanowires. The macrosopic electrical transport also depend on the

orientation of silver nanowires, the conductivity along the orientation direction is about 10 times higher than the vertical direction for 6 layers of AgNW samples.

The multilayers of AgNW thin films in the same direction show also very interesting optical properties in the UV range. At the polarization angle of 90 degree (transverse mode): (1) for different layers of AgNW with same spacing, the positions of the two peaks ~360 nm and ~ 380 nm don't change too much, however as the layers of AgNW increase, the differences of the absorbance between these two peaks become more obviously, peak at ~360 nm decreases but the peak ~380 increases; (2) for 2 layers of AgNW with different spacing, as the spacing increases, the peak at ~360 nm decreases and the peaks at ~380 nm increases, the distance between these two peaks becomes bigger.

Chiral plasmonic nanostructures can be fabricated when the spraying direction is rotated for a few degrees from one AgNWs layer to the next. To keep the system symmetric, the twisted angle is 60 degree and 45 degree for C3 and C4 chiral samples, respectively. The polarized-UV of chiral plasmonic thin films display both longitudinal and transverse modes of the plasmon resonance independently of the polarization of the incident light, because the samples are symmetric and every layer of silver nanowire has the almost same silver nanowire density.

These chiral structures gave rise to giant circular dichroism (CD), in sample with a single helical pitch comprised of 3 or 4 layers of AgNWs reaches 5000 to 7000 mdeg with g-factors ~ 0.2, which is much bigger than the results showed in the literature before. As the layers of silver nanowires increases, the CD signal increases but the g-factors keep constant.

When diluted the AgNW suspension for 10 times, both the CD value and g-factors decreased dramatically for C3 and C4 samples, which means the in-plane coupling among nanowires plays an important role in these systems, because g-factor usually only depends on the materials.

For bigger distance C4 samples with different spacing, the CD intensity keeps almost constant as the spacing increased. However, as the spacing increased, the CD curves

changed obviously, the peak ~ 410 nm becomes broader and the peak ~ 377 nm becomes more obvious.

Hebing HU

Spray-assisted alignment of Layer-by-Layer assembled silver nanowires for linear and chiral nanoplasmonics

Résumé

Ce travail de thèse décrit l'alignement par pulvérisation de nanofils d'argent (AgNWs) aux interfaces solides sous la forme de films mono- et multicouches. Cette technique permet de contrôler la densité de nanofils dans le plan sur des zones macroscopiques avec des paramètres d'ordre nématique atteignant des valeurs > 0,90 dans les films monocouches. La répétition des cycles de dépôt en utilisant l'assemblage couche-par-couche produit des films multicouches dans lesquels par exemple des superstructures uniaxiales ou hélicoïdales peuvent être préparées en choisissant les directions de pulvérisation appropriées pour chaque monocouche individuelle. Les systèmes uniaxiaux sont des polariseurs fortement dépendant de la longueur d'onde (en raison de l'orthogonalité des plasmons transversaux et longitudinaux des AgNWs) et montrent une conductivité anisotrope dans le plan. Les systèmes hélicoïdaux montrent un dichroïsme circulaire très élevé qui peut être ajusté par exemple par le biais de la densité des AgNWs dans le plan ou de la distance entre les monocouches individuelles. Les mesures de la matrice Müller confirment que le dichroïsme circulaire observé découle de la superstructure hélicoïdale des multicouches à base d'AgNWs.

Mots clés: Alignement, pulvérisation à incidence rasante, nanofils d'argent, assemblage couche-par-couche, nanomatériaux orientés.

Abstract

This thesis work describes the spray-alignment of silver nanowires (AgNWs) at solid interfaces in the form of mono- and multilayer films. The technique allows to control the in-plane density of nanowires over macroscopic areas with the best nematic order parameters reaching > 0.90 in monolayer films. Repeated deposition cycles using layer-by-layer assembly yield multilayer films in which for example uniaxial or helically twisted superstructures can be prepared by choosing appropriate spraying directions for each individual monolayer. Uniaxial systems are strong wavelength dependent polarizers (due to the orthogonality of the transversal and longitudinal plasmons of the AgNWs) and they show anisotropic in-plane conductivitiy. Helically twisted systems show very high circular dichroism which can be tuned for example through the in-plane density of AgNWs or through the distance between individual monolayers. Müller Matrix measurements confirm that the observed circular dichroism arises from the helically twisted superstructure of the AgNW multilayers.

Key words: Alignment, grazing-incidence spraying, silver nanowires, Layer-by-Layer assembly, oriented nanomaterials.